Nonlinear Momentum Compaction and Coherent Synchrotron Radiation at the Metrology Light Source

Low-α Commissioning and Development

D I S S E R T A T I O N

zur Erlangung des akademischen Grades

doctor rerum naturalium
(Dr. rer. nat.)
im Fach Physik

eingereicht an der
Mathematisch-Naturwissenschaftlichen Fakultät I
Humboldt-Universität zu Berlin

von
Dipl.-Phys. Markus Ries

Präsident der Humboldt-Universität zu Berlin:
Prof. Dr. Jan-Hendrik Olbertz

Dekan der Mathematisch-Naturwissenschaftlichen Fakultät I:
Prof. Stefan Hecht PhD

Gutachter:
1. Prof. Dr. Andreas Jankowiak
2. Prof. Dr. Norbert Holtkamp
3. Prof. Dr. Jens Knobloch

eingereicht am: 29. Oktober 2013
Tag der mündlichen Prüfung: 12. Mai 2014

Abstract

Short pulses of synchrotron radiation are becoming an increasingly demanded tool in various fields of science. The generation of short synchrotron radiation pulses can be accomplished by different accelerator-based approaches such as free electron lasers, energy recovery linacs or electron storage rings. Linear accelerator driven free electron lasers are capable of generating intense pulses in the femtosecond regime at moderate repetition rates. In comparison, electron storage rings generate pulses of lower intensity with the advantage of large repetition rates. However, electron storage rings rely on radiation emitted by the same bunch(es) every turn, which are present in an equilibrium state. Thus making the electron storage ring a yet unchallenged source of short synchrotron radiation pulses in terms of stability and reproducibility. In addition, storage rings are capable to serve a large number of users simultaneously.

In general, it is possible to distinguish the user community of short pulses at electron storage rings. The first user group is interested in time-resolution applying incoherent synchrotron radiation up to the X-ray regime. The second user group makes use of coherent synchrotron radiation emitted by short bunches at wavelengths large compared to the bunch dimensions, which commonly applies up to the THz-regime. Both user groups are interested in the high average power and stability available at electron storage rings. However, there is a current limitation for stable short bunch operation of electron storage rings, which is due to an instability driven by the emission of coherent synchrotron radiation.

The subject of this thesis is the operation of an electron storage ring at a low momentum compaction to generate short electron bunches as a source for coherent synchrotron radiation. For this purpose the Metrology Light Source is ideally suited, as it is the first light source designed with the ability to adjust the three leading orders of the momentum compaction factor by quadrupole, sextupole and octupole magnets. Therefore, new opportunities to shape the longitudinal phase space arise. Focus will be put on beam dynamics dominated by nonlinear momentum compaction, in particular the generation of a new bucket type – "α-buckets" – and possible applications. Relation of analytical theory, numerical simulations and experimental data will be presented and discussed. In addition, the current limitation due to the bursting instability at the Metrology Light Source bunches will be investigated. The majority of measurements were conducted at the Metrology Light Source complemented by measurements at the BESSY II storage ring.

Keywords: isochronous operation of electron storage rings, low-alpha, nonlinear momentum compaction, alpha-buckets,coherent synchrotron radiation, bursting

Zusammenfassung

Kurze Synchrotronstrahlungspulse sind ein immer wichtiger werdendes Werkzeug in vielen Forschungsfeldern. Dabei erstreckt sich der Anwendungsbereich breit über Fachgebiete wie der Physik, Chemie, Biologie oder Materialwissenschaft. Die Erzeugung kurzer Strahlungspulse kann mit Hilfe verschiedener Beschleuniger-basierter Technologien erfolgen wie zum Beispiel einem Freien-Elektronen-Laser (FEL), einem Linearbeschleuniger mit Energierückgewinnung (ERL) oder einem Elektronenspeicherring. Synchrotronstrahlungsquellen, basierend auf Linearbeschleunigern, sind in der Lage hochintensive Strahlungspulse mit einer Pulsdauer im Femtosekundenbereich bei moderaten Wiederholraten zu erzeugen. Im Vergleich dazu erzeugen Elektronenspeicherringe Strahlungspulse von geringerer Intensität, welche jedoch mit einer deutlich höheren Wiederholrate zur Verfügung stehen. Ein prinzipieller Unterschied ist jedoch die langfristige Speicherung der Elektronenpakete und die damit verbundene Wiederverwendbarkeit. Im Elektronenspeicherring werden die Strahlparameter somit durch Gleichgewichtsprozesse bestimmt, wohingegen sie in Linearbeschleunigern durch die Elektronenquelle gegeben sind. Der Elektronenspeicherring ist daher in der Lage, Pulse von hoher Stabilität und Reproduzierbarkeit zur Verfügung zu stellen. Ein weiterer Vorteil der Elektronenspeicherringe ist die gleichzeitige Versorgung einer großen Zahl von Nutzerplätzen.

Im Allgemeinen ist es möglich die Nutzergemeinschaft von Kurz-Puls-Synchrotronstrahlung in zwei Gruppen zu unterteilen. Ein Teil der Nutzer ist interessiert an zeitaufgelöster, beugungsbegrenzter Spektroskopie mit inkohärenter Synchrotronstrahlung bis in den Röntgenstrahlungsbereich. Die zweite Gruppe verwendet kohärente Synchrotronstrahlung, welche bei Wellenlängen größer als die Ausdehnung der Elektronenpakete entsteht. Beide Nutzergruppen profitieren hierbei von der hohen mittleren Leistung und Stabilität an Elektronenspeicherringen. Jedoch ist die Erzeugung kurzer Pulse mit Hilfe von Speicherringen limitiert durch eine Elektronenstromgetriebene Instabilität, welche ihre Ursache in der Emission kohärenter Synchrotronstrahlung besitzt.

Das Thema der vorgelegten Dissertation ist der quasi-isochrone Betrieb der Metrology Light Source zur Erzeugung kurzer Elektronenpakete mit der damit verbundenen Emission von kohärenter Sychrotronstrahlung. Die Metrology Light Source wurde schon in der Planungsphase auf den quasi-isochronen Betrieb ausgelegt. Es stehen Quadrupol-, Sextupol- und Oktupolmagnete zur Verfügung, um die drei führenden Ordnungen des sogenannten momentum compaction factors zu kontrollieren. Der Schwerpunkte der Arbeit ist nichtlineare, longitudinale Strahldynamik, insbesondere die sogenannten "α-buckets". Der Vergleich zwischen analytischen Ansätzen, numerischen Simulation und experimentellen Daten wird vorgestellt und diskutiert. Desweiteren wurde die Stromlimitierung durch die Bursting-Instabilität an der Metrology Light Source untersucht. Der Großteil der Messungen ist dabei an der Metrology Light Source durchgeführt worden mit komplementären Messungen am Elektronenspeicherring BESSY II.

Contents

1 Introduction

1.1 Synchrotron Radiation

Synchrotron radiation (SR) is electromagnetic dipole radiation emitted by ultra-relativistic charged particles when undergoing acceleration, usually in magnetic fields. The spectrum of this radiation is shifted to high photon energies up to the range of a few hundred keV depending on the particle momentum. Originally being an offspring of high energy particle physics, synchrotron radiation generated by accelerators has evolved into an extensively used tool in various fields of science such as materials science, physical chemistry and life science. Synchrotron radiation incorporates several crucial properties into a single radiation source, thus making it attractive for many different applications. It is a highly brilliant source, which is capable of delivering high photon flux in a broad spectral range featuring tunable polarization.

The "*first generation*" of synchrotron radiation based light sources actually was designed for the purpose of high energy particle physics. However, the byproduct of emitted radiation led to a parasitic use of these machines. "*Second generation*" light sources were formed by storage rings explicitly designed to generate synchrotron radiation, whereas Tantalus I operating in 1968 was the first of this kind [1]. Magnet lattice and therefore electron beam parameters could now be optimized for user demands. The development then focused on designing light sources able to supply higher brightness and brilliance by increasing storable current and decreasing transverse emittance as well as pushing the spectrum towards the hard X-ray regime. The "*third generation*" of synchrotron light sources such as BESSY II, including most of the storage rings operational today, is characterized by the design goal to be optimized for insertion devices further improving the spectral brightness [2].

In parallel to the improvement of storage rings other concepts emerged to satisfy user demands. The Free-Electron Laser (FEL) [3] is able to supply orders of magnitude higher peak-brightness than storage rings at the cost of a lower repetition rate i.e. average brightness and a temporal and spectral pulse-to-pulse fluctuation. This is achieved by making use of self-induced, seeded or self-seeded emission of coherent synchrotron radiation (CSR). Another emerging light source concept is the Energy Recovery Linac (ERL) [4, 5]. An ERL relies on single cycle usage of high energy electron bunches with a following deceleration, i.e. beam power is recirculated instead of beam current. Given a low emittance, high current electron source an ERL can provide lower emittance than electron storage rings operational today, due to the effect of adiabatic damping. It gets rid of the equilibrium emittance generated by stochastic quantum emission of photons, which dominates the beam parameters in storage rings. In addition, there is an upcoming advanced third generation of storage rings such as MAX IV [6] delivering drastically improved beam parameters.

Recently there is a growing interest to push beam parameters in the longitudinal plane, i.e. to shorten bunches to ps lengths [7–9]. Users are more and more interested to make use of the pulsed time structure of synchrotron radiation. On the one hand, there is an interest of the user community in the availability of short X-ray pulses. The length of the radiation pulses affects measurement quantities such as spectral resolution of time-of-flight (TOF) experiments or temporal resolution when exploring dynamic processes in samples. In addition, synchrotron radiation can be used for "pumping" as well as for "probing" samples, where short pulses are favourable. On the other hand, there is another user community interested in the generation of synchrotron radiation in the THz range. For wavelengths larger than the bunch length electrons emit radiation coherently. Therefore, the radiated power does not scale linearly with the number of electrons but is proportional to its square for a fixed bunch shape. This leads to a huge gain in the Far-Infrared (FIR) regime, as the number of electrons stored in a bunch goes up to the order of 10^{11}. Typical electron bunch lengths in storage rings are currently in the order of a few tens of picoseconds. For these bunch lengths the emission of coherent synchrotron radiation is suppressed due to the vacuum chamber dimensions.

FELs and ERLs have an intrinsic advantage when it comes to short pulses as their beam parameters are mainly defined by electron source parameters. However, multiple storage rings offer a special operation mode, where the magnet lattice is tuned to compress the electron bunch to picosecond lengths [10]. A key parameter for shortening the bunch length is the "momentum compaction factor" α. Alpha is a parameter of the storage ring optics, which can be adjusted over several orders of magnitude. The zero-current bunch length scales with $\sqrt{\alpha}$ enabling the option to reduce the bunch length to small values for $\alpha \to 0$. The advantage of using storage rings to generate short bunches is the ability to serve a large number of beamlines in a broad spectral range at high repetition rates using a well established technology. In addition, operating storage rings in low-α is usually possible with moderate hardware requirements. Storage rings also have an intrinsic advantage in stability respectively reproducibility as radiation from the same bunches is observed by the user many turns. Therefore, there are advanced concepts for storage rings to generate bunches or microbunches in the pico- to femtosecond regime such as Laser-slicing, crab-cavities or radio frequency (RF) beat schemes [11–14].

In addition, synchrotron radiation is used by national metrology organizations like the Physikalisch-Technische Bundesanstalt (PTB) or the National Institute of Standards and Technology (NIST) as a source of stable and reproducible radiation [15]. Incoherent synchrotron radiation is one of the most linear sources that exist in terms of brightness, being able to cover more than ten orders of magnitude. The absolute value of the emitted spectral radiation power can be calculated based on fundamental principles [16]. Therefore, synchrotron radiation can be used as primary radiation standard, which is unique for wavelengths shorter than Ultraviolet (UV). The PTB is using synchrotron radiation for metrology purposes for over 25 years and utilizes a dedicated storage ring – the Metrology Light Source – for this purpose [17].

1.2 Metrology Light Source

The Metrology Light Source (MLS) is an electron storage ring based synchrotron light source in Berlin (Germany) owned by the PTB. It was designed, built and is now operated by the Helmholtz-Zentrum Berlin (HZB) [18]. The main purpose of the MLS is to serve as a reference source in the Extreme Ultraviolet (EUV) regime for metrology applications [17, 19]. The MLS is used in a spectral range covering FIR, Mid-Infrared (MIR), Near-Infrared (NIR), Vacuum Ultraviolet (VUV) to EUV. The black line in Fig. 1.1(a) shows a calculation of the spectrally

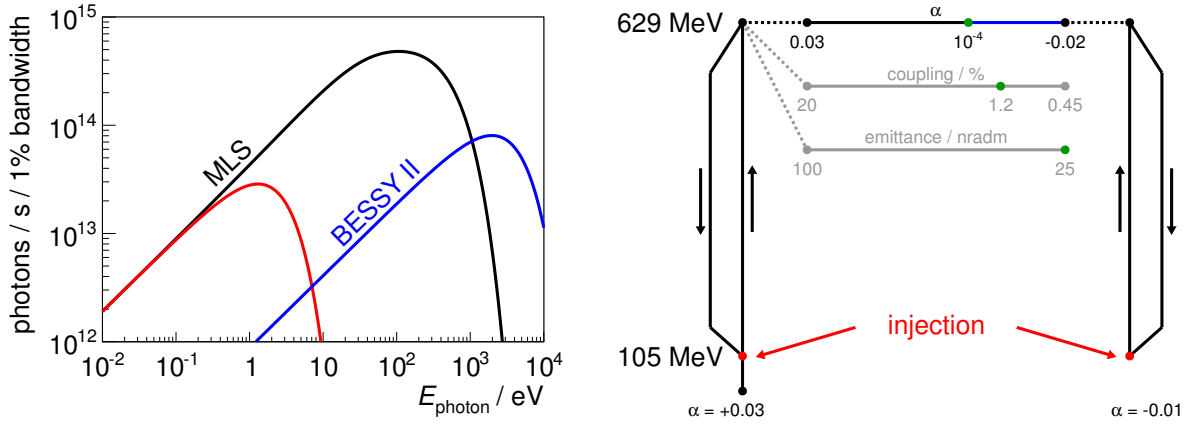

(a) MLS: spectral range

(b) MLS: operation principle

Figure 1.1: Spectrally resolved photon flux for the EUV-beamline at the MLS (a). The black line corresponds to operation at 629 MeV, whereas the spectrum at the injection energy 105 MeV is shown in red. For comparison, the spectrally resolved photon flux of the EUV beamline of the PTB at BESSY II is shown (blue). Operation scheme of the MLS - a ramped synchrotron (b).

resolved photon flux at the EUV beamline of the MLS for a stored beam current of 200 mA. The critical photon energy of the spectrum is about 360 eV. The blue line corresponds to the EUV beamline of the PTB currently in operation at BESSY II. The EUV beamline at the MLS will supplies more than one order of magnitude higher flux mainly due to optimized geometric beam line parameters.

The MLS is a ramped synchrotron operated in storage ring mode during user shifts. A racetrack microtron is used to accelerate electrons to the injection energy of 105 MeV [20]. Electrons are accumulated from the microtron to the storage ring up to 200 mA, which is the upper limit imposed by radiation protection policies. Subsequently, there is an energy ramp to 629 MeV, which takes about three minutes. As the MLS is a "low" electron energy machine as well as very flexible in operation, it is designed to be automatized to a high degree. For this purpose the concept of a state machine was applied. An automated master control program was implemented, that knows all available machine states as well as all transitions between states. Figure 1.1(b) shows a sketch of the operational concept [21]. Energy ramps exist for positive

and negative momentum compaction (see chapter 3) indicated by the vertical plane. Beam parameters are relaxed during the energy ramp to maximize reliability as well as beam current conservation. Upon reaching the target electron energy the dipole magnet excitation is kept constant – storage ring mode. Afterwards, beam parameters like momentum compaction factor, beam size or beam emittance are adjusted by "optic ramps" to fit user demands using elements such as quadrupole and sextupole magnets.

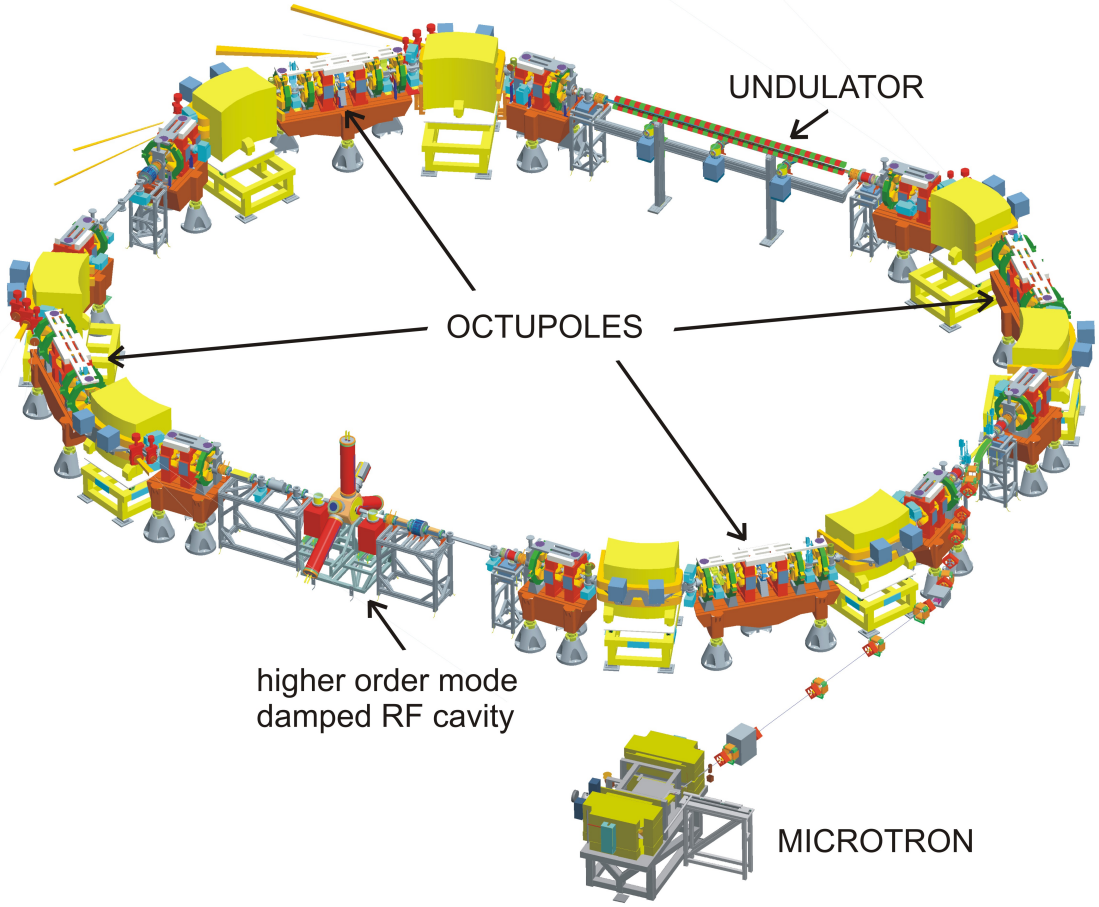

Figure 1.2: Scheme of the MLS.

A sketch of the MLS hardware is shown in Fig. 1.2. There are four double bend achromat cells with a slight break in symmetry in the connecting short (2.5 m) and long (6 m) straight sections. The lattice is characterized by a small bending radius $\rho = 1.528$ m inside the dipole magnets in combination with a large bending angle per dipole of $\pi/4$. The large bending angle per dipole leads to a high value of the dispersion function in the center of the achromat. There are 24 quadrupoles powered by individual power supplies providing a high degree of freedom in the scope of linear beam optics [22]. In addition, the MLS holds three families of sextupole

magnets to be able to control the chromaticity in all three planes. Finally, there is one octupole magnet per cell placed in the center of the achromat, where the dispersion is at its maximum. Therefore the octupole has maximized impact for longitudinal beam dynamics. The purpose of the third sextupole magnet family and the octupole magnet is to control higher orders of the momentum compaction factor. This plays an important role when operating the MLS in the short bunch mode – "low-α". In this way, the MLS is the first electron storage ring optimized by design for higher order momentum compaction control as well as the generation of coherent synchrotron radiation [18, 23].

A single, normal conducting, higher order mode damped RF cavity is used to accelerate the electrons and to resupply the energy lost due to synchrotron radiation [24]. It is able to supply 500 kV of effective acceleration voltage with a prospective upgrade to 700 kV. Table 1.1 gives a review of MLS machine parameters that will be relevant throughout this work.

The "standard user mode" is characterized by a horizontal emittance of about 120 nm rad. Transverse β-functions as well as the dispersion function D for this mode are shown in Fig. 1.3. The data was obtained by fitting the orbit response of the corrector magnets to a model of the storage ring (see section 4.1). Beam optics of standard user operation at the MLS are deviating from the classical achromat setup. The value of the dispersion function at the septum magnet (at $s = 0$ m) was set to zero to increase the momentum acceptance and hence the beam lifetime [25].

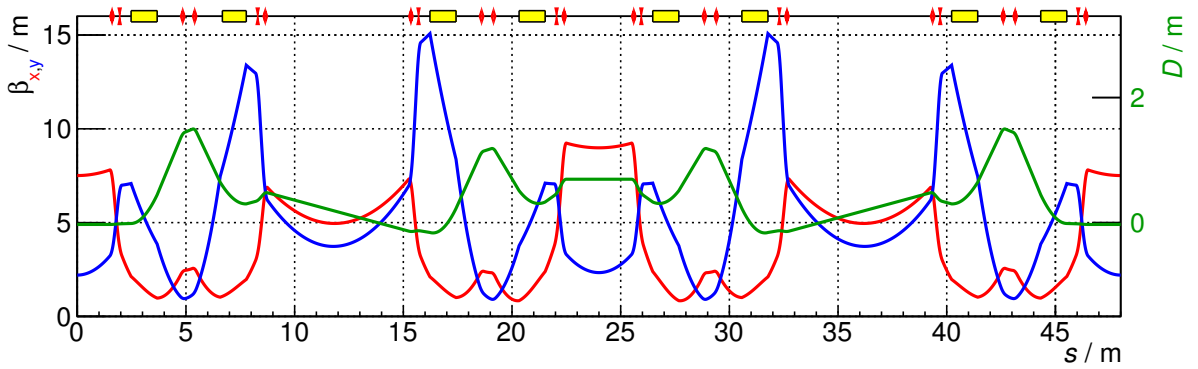

Figure 1.3: MLS magnet optics for standard user operation: Horizontal (red) and vertical (blue) β-functions $\beta_{x,y}$ as well as horizontal dispersion D (green) were measured by fitting a model to the orbit response matrix (LOCO [26]). The top axis indicates the position of dipole (yellow) and quadrupole (red) magnets.

Due to the compact design of the MLS, the circumference is too short to allow operation with a significant gap in the filling pattern. Clearing gaps are commonly used at storage rings with a length in the order of 100 ns to fight trapping of ions by the attractive potential generated by the electron beam. Alternative countermeasures are in action such as clearing electrodes, a NEG-coated vacuum chamber section as well as electron beam shaking. The impact of ions on the dynamics of stored electrons is enhanced by a comparatively low electron energy. This is particularly inconvenient at injection energy, where the injection is severely hampered imposing

current limitations.

Of special interest for the presented work is the momentum compaction factor. At the MLS the momentum compaction factor can be varied over a wide range covering about three orders of magnitude as well as operation with positive or negative values. This flexibility is intended by design to enable short bunch operation, which will be discussed in detail in section 3.

parameter	**standard user**	**low alpha**	**tuning range**
electron energy	629 MeV		50 MeV ... 629 MeV
γ	1231		98 ... 1231
current	200 mA	200 mA (bursting) 0.3 mA (stable)	1 pA ... 200 mA
bunch current	2.5 mA	2.5 mA (bursting) 4 µA (stable)	1 pA ... 10 mA
bunch charge	400 pC	400 pC (bursting) 0.6 pC (stable)	e ... 1.6 nC
typical lifetime (at 629 MeV, 195 mA)	4.5 h	10 h	$<$ 30 h
RF cavity voltage	500 kV	500 kV	$<$ 500 kV
mom. comp. factor			
α_0	0.03	1.3×10^{-4}	$-0.03 \ldots 0.07$
α_1	-0.4	< 0.01	
α_2	≈ 1	≈ 3	$-200 \ldots 200$
tunes			
horizontal tune	3.178		
vertical tune	2.232		
longitudinal tune	0.017	0.0011	< 0.07
natural chromaticity	$\xi_x = -3.4$ $\xi_y = -5.6$	$\xi_x = -4.2$ $\xi_y = -6.0$	
damping partition numbers *	$J_x = 1.05$, $J_y = 1.0$, $J_s = 1.95$		
damping times *			
τ_x	21.1 ms		21.1 ms... 42 s
τ_y	22.2 ms		22.2 ms... 44 s
τ_s	11.4 ms		11.4 ms... 23 s
zero current bunch length (rms) *	19 ps	1.3 ps	sub-ps ... 100 ps
horizontal emittance	120 nm rad	200 nm rad	$>$ 25 nm rad
emittance coupling $\varepsilon_y/\varepsilon_x$	0.5%	20%	
circumference	48 m		
RF frequency	499.654 MHz		
revolution frequency	6.2457 MHz		
harmonic number	80		
max. dispersion	1.5 m	1.9 m	$>$ 0.9 m
dipole bending radius	1.515 m		
magnetic induction (bend)	1.384 T		$\leq$ 1.384 T
energy loss per turn *	9140 eV		0.4 eV ... 9140 eV
crit. photon energy *	360 eV		0.2 eV ... 360 eV
fill pattern	homogeneous		arbitrary
full chamber height	42 mm		
full chamber width	70 mm		
smallest hor. aperture	20 mm (septum magnet)		

Table 1.1: Selected beam and machine parameters of the MLS. Values marked with * are calculated.

2 Longitudinal Beam Dynamics towards Quasi-Isochronous Operation of Storage Rings

This chapter is dedicated to the basics of longitudinal beam dynamics for a single particle. Possibilities to manipulate the equilibrium bunch length in a storage ring will be shown. Impedance, multi particle effects, coherent synchrotron radiation as well as deviations from highly relativistic dynamics will be neglected. Transverse particle dynamics [27, 28] are of limited relevance for the discussed phenomena and will be treated when necessary.

2.1 Reference Frame

To describe the particle motion a combination of global and local coordinates will be used as shown in Fig. 2.1. The reference system is defined by the trajectory of a reference particle with design momentum traveling along the design orbit. By definition the horizontal displacement

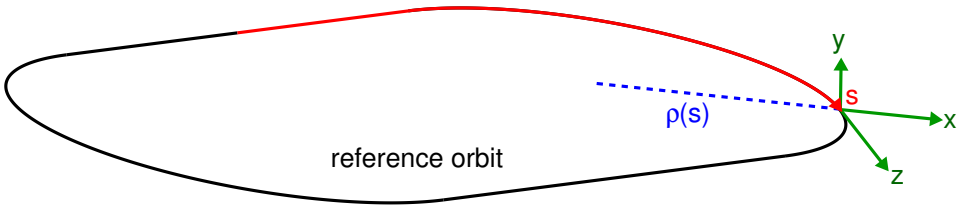

Figure 2.1: Definition of the coordinate system used to describe the beam dynamics.

x, vertical displacement y and longitudinal displacement z are measured with respect to the reference particle. These quantities as well as the bending radius of the reference orbit $\rho(s)$ are local quantities in dependence of the longitudinal coordinate s. The coordinate s corresponds to the longitudinal position of the reference particle on the design orbit around the machine. For a machine with a design orbit in the horizontal plane, this kind of coordinate system corresponds to a Frenet–Serret type.

A convenient quantity to describe particles with momenta p, differing from the momentum of the reference particle, is the relative momentum deviation δ defined by:

$$\delta = \frac{\Delta p}{p_0} = \frac{p - p_0}{p_0} = \frac{1}{{\beta_0}^2}\frac{\Delta E}{E_0} \approx \frac{\Delta E}{E_0}, \tag{2.1}$$

where E corresponds to particle energy and $\Delta E = E - E_0$ to energy deviation with respect to the reference particle. Throughout this work, if not stated otherwise, the index "0" will be used to denote properties of the reference particle. As for light sources only highly relativistic particles are relevant, relative momentum deviation and relative energy deviation can be used synonymously.

2.2 Dispersion Function

Electrons with different momenta will experience different impact from the magnetic fields used to guide the beam. Therefore, these electrons will travel on different paths through the storage ring. In the scope of linear beam optics the equation of motion in the horizontal plane is given in the form of an inhomogeneous Hill's equation [29]:

$$\frac{\mathrm{d}^2 x\left(s\right)}{\mathrm{d}s^2} + \left(\frac{1}{\rho\left(s\right)^2} - k\left(s\right)\right) x\left(s\right) = \frac{1}{\rho\left(s\right)}\delta, \tag{2.2}$$

whereas $\rho(s)$ describes the bending radius of the on-momentum reference particle and the normalized field gradient $k\left(s\right) = \frac{1}{B_y \rho}\partial B_y / \partial x$. The dispersion function $D(s)$ is defined as the trajectory of a particle with a momentum deviation of $\delta = 1$. The solution of Eq. 2.2 for $\delta = 1$ in a sector bending magnet ($\rho = \text{const.}, k\left(s\right) = 0$) has the form [28]:

$$D\left(s\right) = D_{\text{initial}}\ \cos\left(\frac{s - s_{\text{initial}}}{\rho}\right) + D'_{\text{initial}}\ \rho \sin\left(\frac{s - s_{\text{initial}}}{\rho}\right) + \rho\left(1 - \cos\left(\frac{s - s_{\text{initial}}}{\rho}\right)\right), \tag{2.3}$$

$$D'\left(s\right) = -\frac{D_{\text{initial}}}{\rho}\sin\left(\frac{s - s_{\text{initial}}}{\rho}\right) + D'_{\text{initial}}\ \cos\left(\frac{s - s_{\text{initial}}}{\rho}\right) + \sin\left(\frac{s - s_{\text{initial}}}{\rho}\right), \tag{2.4}$$

whereas prime indicates differentiation with respect to s. D_{initial} and D'_{initial} are the values of the dispersion respectively its derivative at the entrance of the magnet. The dispersive horizontal displacement $x_D(s)$ can be calculated by:

$$x_D(s) = D(s)\delta, \tag{2.5}$$

as well as the angle:

$$x_D{}'(s) = D'(s)\delta. \tag{2.6}$$

Example trajectories of particles with different momenta in a sector bending magnet are shown in Fig. 2.2(a). Particles are entering the bending magnet with a dispersive displacement corresponding to Eq. 2.5 and are propagated on trajectories given by Eqs. 2.3 and 2.4. Particle

positions are highlighted by dots for the time when the reference particle (black) passes entrance, center and exit of the bending magnet. In drift sections the bending radius $\rho(s)$ is assumed to be infinity yielding a constant D'.

A measurement of two dispersive closed orbits for a double bend achromat (DBA) lattice setup of the MLS is shown in Fig. 2.2(b). Data acquired by beam position monitors (BPMs) for two successively conducted measurements is shown for a momentum deviation of $\delta \approx +10^{-3}$ (red) and $\delta \approx -10^{-3}$ (blue.) A DBA segment consists of two bending magnets with a quadrupole

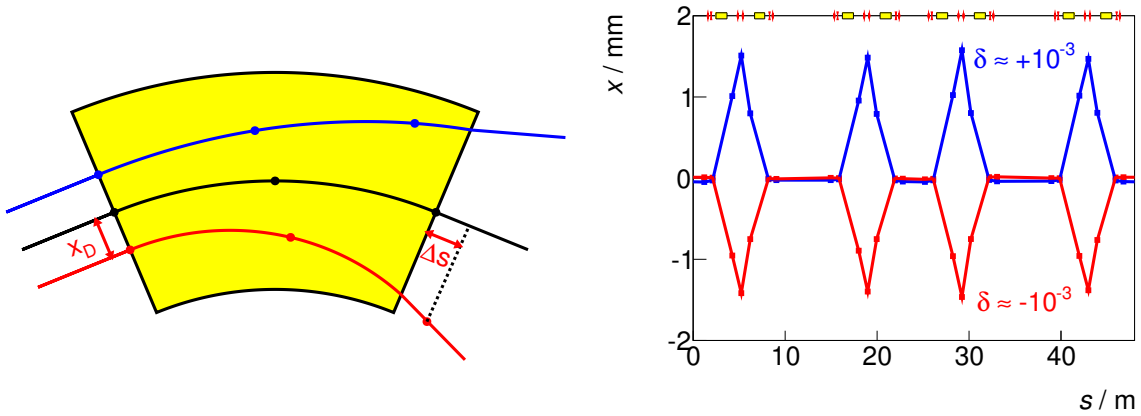

(a) path lengths inside bending magnet

(b) measured dispersive closed orbits

Figure 2.2: Simplified visualization of the momentum dependent orbit length inside a sector bending magnet (a). The reference trajectory (black) as well as trajectories featuring $\delta > 0$ (blue) and $\delta < 0$ (red) are shown (see text). Examples of two dispersive closed orbits for a DBA lattice setup measured at the MLS (b).

magnet in between. The quadrupole strength is adjusted to achieve zero dispersion at the segments ends.

Linear beam optics do not consider magnets of orders higher than quadrupoles. At light source storage rings the use of sextupole magnets is mandatory, whereas the MLS even uses octupole magnets.

In general, the dispersion function features higher order terms in δ, as ρ and k are not only functions of s but as well of δ [30]:

$$D(s,\delta) = D_0(s) + D_1(s)\delta + D_2(s)\delta^2 \ldots = \sum_{i=0}^{\infty} D_i \delta^i. \tag{2.7}$$

Higher order dispersion is a relevant parameter for beam dynamics at storage rings operated with short bunches using low momentum compaction, which will be addressed in the following sections. For reasons of simplicity the term $D(s)$ will be used to denote $D_0(s)$, whenever relevant the term $D(s,\delta)$ will be explicitly stated.

2.3 Momentum Compaction Factor

Particles stored in electron storage rings show a spread in their momentum distribution. One source for this momentum spread is the stochastic nature of synchrotron radiation emission known as "quantum excitation" [31]. Due to different momenta, electrons travel along different trajectories defined by the dispersion function yielding momentum dependent orbit lengths. Additionally, transverse oscillation amplitudes can introduce a spread in orbit length. However, this effect can be compensated by adjusting transverse chromaticities as will be shown in section 2.4. Therefore, the effect of transverse amplitudes on the orbit length will be neglected. The length of the closed orbit C with respect to the momentum deviation δ of the particle can be written as:

$$C = C_0 \left(1 + \alpha\delta\right), \tag{2.8}$$

or in a more commonly used notation:

$$\frac{C}{C_0} - 1 = \frac{\Delta C}{C_0} = \alpha\delta, \tag{2.9}$$

whereas C_0 is the orbit length of the reference particle, $C = C_0 + \Delta C$ and α the momentum compaction factor. The momentum compaction factor α is momentum dependent and can be described by an expanded power series:

$$\alpha = \alpha\left(\delta\right) \equiv \sum_{i=0}^{\infty} \alpha_i \delta^i, \tag{2.10}$$

yielding the commonly applied first order approximation ($\alpha \approx \alpha_0$):

$$\frac{\Delta C}{C_0} = \alpha_0\delta + \mathcal{O}\left(\delta^2\right), \tag{2.11}$$

There are several different definitions for Eq. 2.8 relating the momentum deviation and orbit length [32]. The definition used in this work was chosen to fit practical demands and is in correspondence to the traditional notation.

To first order in δ, the momentum dependence of the orbit length for a light source lattice is dominated by the contribution of different paths in curved sections. Therefore, α_0 can be calculated by evaluating the dispersion function inside the bending magnets [33] as depicted in Fig. 2.2(a):

$$\alpha_0 = \frac{1}{C_0} \oint \frac{D_0\left(s\right)}{\rho\left(s\right)} \mathrm{d}s. \tag{2.12}$$

Higher orders of the momentum compaction factor are introduced by a non-vanishing D_0' in straight sections as well as higher orders of the dispersion function. The next higher order of α

can be calculated by [30]:

$$\alpha_1 = \frac{1}{C_0} \oint \left(\frac{D_0'(s)^2}{2} + \frac{D_1(s)}{\rho(s)} \right) \mathrm{d}s. \tag{2.13}$$

In addition, electrons with different momenta travel at different velocities βc. Therefore the relative change of the revolution time $T_{\mathrm{rev}} = C/\beta c$ with respect to momentum is given by [29]:

$$\frac{\Delta T_{\mathrm{rev}}}{T_{\mathrm{rev0}}} = \frac{\Delta \frac{C}{\beta}}{\frac{C_0}{\beta_0}} = \frac{\Delta C}{C_0} - \frac{\Delta \beta}{\beta_0} = \underbrace{\left(\alpha - \frac{1}{\gamma^2} \right)}_{\eta} \delta \approx \alpha \delta, \tag{2.14}$$

with η being the slip factor. Hence, there are two momentum dependent effects contributing to the revolution time. The change of orbit length introduced by the different interaction of the particles with the magnet lattice $\Delta C/C_0$ as well as the velocity change with momentum $\Delta v/v_0 = \Delta\beta/\beta_0$. A scheme to calculate higher orders of the slip factor is given in [34]. For the MLS, being a low electron energy machine, the term γ^2 is still negligible compared to α, e.g. at 629 MeV the ratio of both terms is $|\alpha| / \frac{1}{\gamma^2} > 100$ for operation with small α. As $|\alpha| \gg \gamma^{-2}$ is usually valid for a synchrotron light source, the approximation $\eta \approx \alpha$ will be used throughout this work.

Equation 2.14 can be expressed in terms of revolution frequency f_{rev}, yielding the result of:

$$\frac{\Delta T_{\mathrm{rev}}}{T_{\mathrm{rev0}}} = -\frac{\Delta f_{\mathrm{rev}}}{f_{\mathrm{rev}}} = -\frac{\Delta f_{\mathrm{rev}}}{f_{\mathrm{rev0}} + \Delta f_{\mathrm{rev}}}. \tag{2.15}$$

2.4 Amplitude Dependent Orbit Length

Particles oscillating in the horizontal or vertical plane will perform betatron oscillations around the closed orbit. Therefore these particles will have to travel a longer path to complete one revolution compared to the reference particle. The orbit length as defined in Eq. 2.8 does not include this amplitude dependency. The effect of an amplitude dependent path length can lead to a smearing of the bunch length [27, 35]:

However, path lengthening due to betatron oscillation can be suppressed by reducing transverse chromaticity towards zero as given in [36]:

$$\Delta C = -2\pi \left(J_x \xi_x + J_y \xi_y \right), \tag{2.16}$$

where $J_{x,y}$ correspond to the horizontal and vertical action-invariants and $\xi_{x,y}$ to the horizontal and vertical chromaticities, which are discussed in more detail in section 3.10.

Calculations performed to evaluate the impact for MLS low-α optics (see chapter 3) following

the estimates $J_x \approx \varepsilon_x/2$ and $J_y \approx 0$ yield:

$$\text{natural chromaticity:} \qquad \left.\frac{\Delta C}{C_0}\right|_{\xi_x=-6.8} \leq 9 \times 10^{-8} \approx \alpha_0\delta_0, \tag{2.17}$$

$$\text{corrected chromaticity:} \qquad \left.\frac{\Delta C}{C_0}\right|_{\xi_x=0.2} \leq -2.6 \times 10^{-9} \ll \alpha_0\delta_0, \tag{2.18}$$

with $\varepsilon_x = 200\,\text{nm rad}$, $\alpha_0 = 1.27 \times 10^{-4}$, $\delta_0 = 4.4 \times 10^{-4}$ and $\alpha_0\delta_0 = 5.6 \times 10^{-8}$. In the case of operation at natural transverse chromaticities the path lengthening due to transverse oscillation amplitudes is larger than the lengthening contributed by the term $\alpha_0\delta_0$. Therefore, following [36], for low-α user operation at the MLS transverse chromaticities were set to small positive values $\xi_{x,y} \approx 0.2$ to avoid a smearing of the bunch length as well as coupling between horizontal and longitudinal plane.

2.5 Acceleration

The energy loss per turn due to synchrotron radiation of a single electron in the bending magnets can be calculated by [37]:

$$\frac{\Delta E}{\text{turn}} = W_{\text{bend}}(E) = \frac{e^2}{3\epsilon_0(m_0c^2)^4}\frac{E^4}{\rho} \overset{e^-}{=} 88.463\frac{(E[GeV])^4}{\rho[m]}\ \text{keV}. \tag{2.19}$$

Energy loss per turn due to insertion devices can be calculated by similar expressions [31]. However, at the MLS standard operation energy of 629 MeV the energy loss is dominated by synchrotron radiation emitted in bending magnets accounting to more than 95% of the radiation power. For stable storage, the energy loss has to be resupplied to the electrons. This is done through acceleration by RF cavities usually operating in a frequency range from 100 MHz to 3 GHz. The RF cavity of the MLS operates at 500 MHz. The integral of the longitudinal electric field component $\mathcal{E}$ seen by an electron passing through a cavity of the length L can be translated into an effective acceleration voltage:

$$\frac{\Delta E}{\text{RF cavity pass}} = e\int_{-L/(2\beta c)}^{L/(2\beta c)} \mathcal{E}(t'+t)\beta c\ \mathrm{d}t' = eU(t) = eU\left(\varphi\left(t\right)\right), \tag{2.20}$$

where $U(\varphi)$ is an effective accelerating voltage at the phase $\varphi(t) = 2\pi f_{\text{rf}}t$. In a multi-cavity setup containing RF cavities at different frequencies or phases, $U(\varphi)$ may be more complicated. In the case of a single RF-cavity, as it is the case at the MLS, $U(\varphi)$ can be expressed by:

$$U\left(\varphi\left(t\right)\right) \overset{\text{MLS}}{=} U_0 \sin\varphi(t), \tag{2.21}$$

where U_0 is the maximum integrated voltage applied. The value U_0 corresponds to the situation where the electric field is at its peak, when the particle is located in the center of the RF cavity. The ratio of peak voltage to effective voltage due to a finite particle velocity is given by the

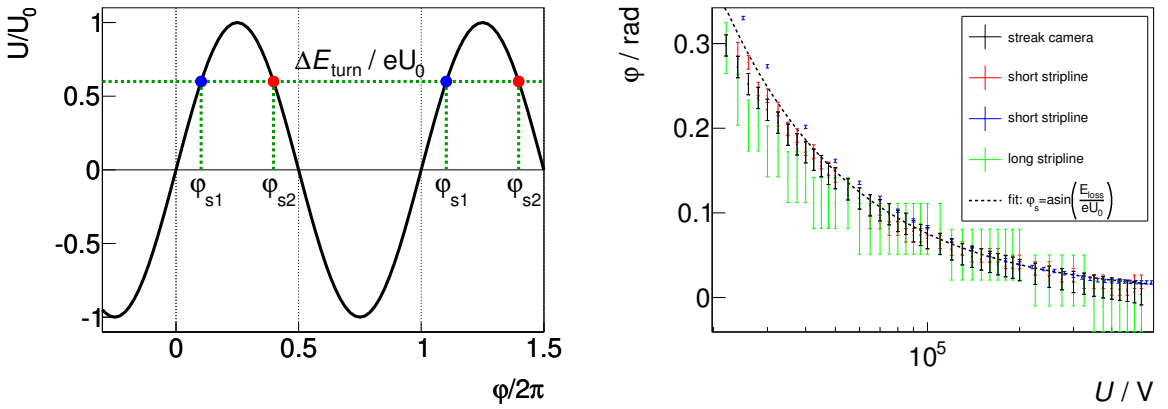

(a) points of synchronous phase

(b) measurement of φ_s

Figure 2.3: Left: Points of synchronous phase φ_s and sign of phase focusing voltage gradient (red / blue). Right: Measurement of the synchronous phase in the standard operation mode of the MLS.

transit time factor $\tilde{T}$, which is at the MLS well within the highly relativistic limit corresponding to $\tilde{T} \approx 2/\pi$.

To account for the energy balance the condition $eU_0 \geq W(E_0)$ applies. The phase φ_s with $eU_0 \sin(\varphi_s) = W(E_0)$ is called the synchronous phase. For one RF voltage cycle there are two points in phase, where the particles can gain the right amount of acceleration to exactly compensate for the synchrotron radiation losses as depicted in Fig. 2.3(a). The synchronous phase φ_s can be varied by changing the parameter U_0:

$$\sin \varphi_s = \frac{W(E)}{eU_0}. \tag{2.22}$$

An example measurement of φ_s as a function of U_0 applying different detection methods is shown in Fig. 2.3(b). A single bunch was stored in the standard operation mode of the MLS. The RF cavity voltage was varied over a range from 20 kV to 500 kV measuring the synchronous phase φ_s by evaluating arrival time at striplines (red, blue, green) as well as a streak camera (black).

Throughout this work, the phase φ will always be measured with respect to the RF phase, when not explicitly stated otherwise.

2.6 Bound Longitudinal Motion – Phase Focusing

Momentum dependence of the revolution time, as given in Eq. 2.14, leads to a phase slip per turn with respect to the RF voltage phase for momentum deviating particles, which can be

calculated by:

$$\frac{\Delta z}{\text{turn}} \approx -\alpha\delta C_0, \tag{2.23}$$

$$\frac{\mathrm{d}\varphi}{\mathrm{d}z} = -\frac{2\pi f_{\mathrm{rf}}}{\beta c}, \tag{2.24}$$

$$\frac{\Delta\varphi}{\text{turn}} = 2\pi h\alpha\delta, \tag{2.25}$$

The sign of $\Delta z/\text{turn}$ in Eq. 2.23 is a direct consequence of the applied coordinate system as depicted in Fig. 2.1.

Because the longitudinal motion is generally slow compared to the revolution time, the approximation of a continuous phase slip per revolution will be used:

$$\frac{\Delta\varphi}{\text{turn}} \approx \frac{\mathrm{d}\varphi}{\mathrm{d}n}, \tag{2.26}$$

$$\frac{\mathrm{d}s}{\mathrm{d}n} = T_{\mathrm{rev0}}\beta_0 c = \frac{h\beta_0 c}{f_{\mathrm{rf0}}}, \tag{2.27}$$

$$\frac{\mathrm{d}\varphi}{\mathrm{d}s} = \frac{2\pi f_{\mathrm{rf}}\alpha}{\beta_0 c}\delta, \tag{2.28}$$

where n denotes the number of turns [34]. However, for extremely short bunches the approximation given in Eq. 2.26 may fail due to the limited number of photon emission events per turn. This effect is called synchrotron radiation excitation [38] and will be discussed in section 3.7.

The energy loss per turn due to synchrotron radiation is in principle of stochastic nature. However, the number of photons emitted per turn will be approximated to be constant. The number of photons emitted per unit length is approximately given by $N_{\mathrm{photons}}/2\pi\rho \approx 1.9\ \mathrm{T}^{-1}\ \mathrm{m}^{-1}B$, whereas B corresponds to the magnetic field responsible for the radiation. For the MLS this value estimates to $N_{\mathrm{photons}}/2\pi\rho \approx 2.6\ \mathrm{m}^{-1}$ inside the bending magnets [37].

For simplicity a single RF cavity will be considered (MLS case). The energy change per turn is then given by:

$$\frac{\Delta E}{\text{turn}} = eU_0 \sin(\varphi) - W_{\mathrm{loss}}, \tag{2.29}$$

where the energy loss per turn W_{loss} includes synchrotron radiation in bending magnets and insertion devices as well as other sources of energy loss, i.e. impedances. At 629 MeV the energy loss at the MLS will be approximated by $W_{\mathrm{loss}} \approx W_{\mathrm{bend}}(E_0)$. The energy loss in bending magnets $W_{\mathrm{bend}}(E)$ is strongly dependent on the electron energy as shown in Fig. 2.4(a):

$$\frac{W_{\mathrm{bend}}(E)}{W_{\mathrm{bend}}(E_0)} = (1+\delta)^4. \tag{2.30}$$

Nevertheless for reasons of simplicity the approximation $W_{\mathrm{bend}}(E) \approx W_{\mathrm{bend}}(E_0)$ will be used, as mainly halo particles are affected in higher order terms. However, the longitudinal phase space

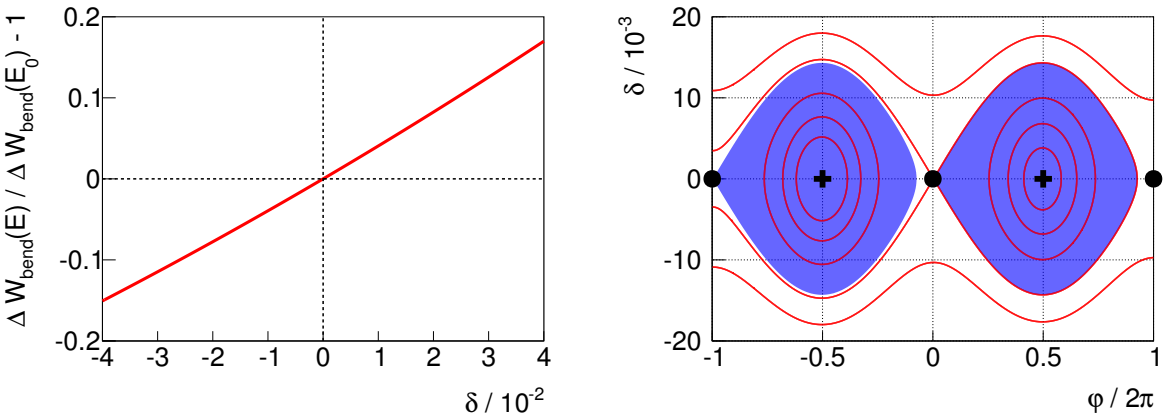

(a) energy dependent synchrotron radiation loss

(b) standard user: longitudinal phase space

Figure 2.4: Calculated, δ-dependent energy loss per turn in dipole magnets for the MLS operated at 629 MeV (a). Longitudinal phase space of the MLS standard user mode (b). Stable fixed points are indicated by black crosses, whereas unstable fixed points are marked by black circles. Areas of stable oscillations around the stable fixed points are marked blue.

can be distorted significantly by this effect. Equation 2.29 can be rewritten in the form of:

$$\frac{\Delta E}{\text{turn}} = eU_0 \left(\sin\left(\varphi\right) - \sin\left(\varphi_s\right)\right), \tag{2.31}$$

yielding in units of relative momentum deviation δ while using the approximation of continuous energy loss:

$$\frac{\mathrm{d}\delta}{\mathrm{d}s} = \frac{f_{\mathrm{rf}}}{h\beta_0^3 c}\frac{eU_0}{E_0}\left(\sin\left(\varphi\right) - \sin\left(\varphi_s\right)\right). \tag{2.32}$$

Equations 2.28 and 2.32 form a system of two coupled first order differential equations. In the approximation of small amplitude oscillations around the synchronous phase as well as $\alpha \approx \alpha_0$ the described dynamics correspond to the system of the harmonic oscillator: $\ddot{\delta} + \omega_s^2 \delta = 0$. Therefore particles perform sinusoidal oscillations – *synchrotron oscillations* – with the characteristic frequency:

$${f_s}^2 = \frac{{\omega_s}^2}{4\pi^2} = -\frac{f_{\mathrm{rf}}^2 \alpha_0 eU_0 \cos\left(\varphi_s\right)}{2\pi {\beta_0}^2 E_0 h}. \tag{2.33}$$

Additionally, it is common to express the frequency of the synchrotron oscillation f_s normalized to the revolution frequency f_{rev} defining the longitudinal tune $Q_s = f_s/f_{\mathrm{rev}}$. Therefore, Q_s can

be calculated by:

$$Q_s{}^2 = -\frac{\alpha_0 h e U_0 \cos(\varphi_s)}{2\pi {\beta_0}^2 E_0}. \tag{2.34}$$

The sign of the term $\alpha_0 U_0 \cos(\varphi_s)$ in Eqs. 2.33 and 2.34 indicates a boundary condition on the involved quantities for stable oscillations. This problem is related to "crossing γ-transition" at hadron machines [39].

2.7 Hamiltonian

By the use of Hamilton's equations:

$$\frac{\partial \mathcal{H}}{\partial p} = \frac{\mathrm{d}z}{\mathrm{d}t}, \qquad -\frac{\partial \mathcal{H}}{\partial z} = \frac{\mathrm{d}p}{\mathrm{d}t}, \tag{2.35}$$

applied to Eqs. 2.28 and 2.32 using $f_{\mathrm{rf0}} = \text{const.}, \mathrm{d}/\mathrm{d}t \approx \beta_0 c \, \mathrm{d}/\mathrm{d}s$ within the limits of an ultra-relativistic particle motion:

$$\frac{\partial \mathcal{H}}{\partial \delta}\frac{\partial \delta}{\partial p} = \frac{\mathrm{d}z}{\mathrm{d}\varphi}\frac{\mathrm{d}\varphi}{\mathrm{d}s}\frac{\mathrm{d}s}{\mathrm{d}t}, \qquad -\frac{\partial \mathcal{H}}{\partial \varphi}\frac{\partial \varphi}{\partial z} = \frac{\mathrm{d}p}{\mathrm{d}\delta}\frac{\mathrm{d}\delta}{\mathrm{d}s}\frac{\mathrm{d}s}{\mathrm{d}t}, \tag{2.36}$$

$$\frac{\partial \mathcal{H}}{\partial \delta} = -\beta_0^2 E_0 \alpha \delta, \qquad \frac{\partial \mathcal{H}}{\partial \varphi} = \frac{1}{2\pi h}\left[eU(\varphi) - W_{\mathrm{loss}}(\delta)\right], \tag{2.37}$$

the Hamiltonian can be constructed by integration [34]:

$$\mathcal{H}(\varphi, \delta) = -\beta_0^2 E_0 \int \alpha\delta \, \mathrm{d}\delta + \frac{1}{2\pi h}\int \left[eU(\varphi) - W_{\mathrm{loss}}(\delta)\right] \, \mathrm{d}\varphi + \mathcal{H}_0, \tag{2.38}$$

where $\mathcal{H}_0$ is a constant of integration, which will be set to zero further on. Assuming $U(\varphi) = U_0 \sin(\varphi)$ and $W_{\mathrm{loss}} = \text{const.} = eU_0 \sin(\varphi_s)$, Eq. 2.38 yields:

$$\mathcal{H}(\varphi, \delta) = -\beta_0^2 E_0 \int \alpha\delta \, \mathrm{d}\delta - \frac{eU}{2\pi h}\left[\cos(\varphi) + \varphi \sin(\varphi_s)\right]. \tag{2.39}$$

Figure 2.4(b) shows the Hamiltonian evaluated for parameters corresponding to the standard user mode at the MLS. Red lines mark equipotential trajectories. Areas of stable oscillations around the stable fixed points (black crosses) are marked in blue and enclosed by unstable fixed points (black dots) defining the RF-bucket. Fixed points at $(\varphi_{\mathrm{FP}}, \delta_{\mathrm{FP}})$ are defined by:

$$\left.\frac{\partial \mathcal{H}}{\partial \varphi}\right|_{\varphi_{\mathrm{FP}}} = 0, \tag{2.40}$$

$$\left.\frac{\partial \mathcal{H}}{\partial \delta}\right|_{\delta_{\mathrm{FP}}} = 0. \tag{2.41}$$

The Hamiltonian given in Eq. 2.38 can by simplified by using an applied RF-cavity voltage of $U(\varphi) = U_0 \sin(\varphi)$, a negligible variation of the emitted radiated power within the regarded momentum regime $W_{\text{loss}}(\delta) \approx eU_0 \sin(\varphi_s)$, an approximately constant momentum compaction factor $\alpha(\delta) \approx \alpha_0$ and small oscillation amplitudes with respect to the synchronous phase $\varphi - \varphi_s = \Delta\varphi << 1$:

$$\mathcal{H}_{\text{harm}}(\Delta\varphi, \delta) = -\frac{\beta_0^2 E_0 \alpha_0}{2}\delta^2 + \frac{eU_0 \cos(\varphi_s)}{4\pi h}\Delta\varphi^2. \tag{2.42}$$

This Hamiltonian describes a harmonic oscillator with a characteristic frequency given by equation 2.33.

For the MLS at 629 MeV the overvoltage factor, defined by the ratio of maximum RF cavity voltage and energy loss per turn, is $U_{0,\max}/W_{\text{loss}} \approx 50$. Therefore, the effect induced by the synchronous phase is negligible for large U_0, e.g. $\varphi_s(629\,\text{MeV}, 500\,\text{kV}) \approx 0.018\,\text{rad}$, i.e. $\cos(\varphi_s) \approx 1$.

2.8 Zero-Current Bunch Length

Electrons stored in the RF bucket of an electron storage rings are subject to quantum excitation and radiation damping. For arbitrary initial phase space populations the equilibrium state is reached within a few longitudinal damping times τ_s, which is usually in the order of tens of milliseconds. For standard operation the calculated longitudinal damping time at the MLS is $\tau_{s629\,\text{MeV}} \approx 11.1$ ms, whereas $\tau_{s105\,\text{MeV}} \approx 2.4$ s at injection energy [31]. The equilibrium state is characterized by a Gaussian distribution in momentum [37]. The rms energy spread δ_0 is to some extend independent on the transverse optics (see section 3.4) and corresponds for MLS operation at 629 MeV to $\delta_0 = 4.4 \times 10^{-4}$. Longitudinal dynamics, as described in the previous sections, propagate the energy spread to the phase plane. Commonly the extension of the bunch in the equilibrium state in phase and momentum is small compared to bucket dimensions. Therefore, the rms extension in phase can by calculated using Eq. 2.42:

$$(\Delta\varphi_\sigma)^2 = \frac{2\pi h {\beta_0}^2 E_0 \alpha_0 \delta_0^2}{eU_0 \cos(\varphi_s)}. \tag{2.43}$$

In more practical units the extension can by written as the rms bunch length:

$$\sigma_0 = \sqrt{\frac{hc^2 E_0 {\beta_0}^4 \alpha_0 \delta_0^2}{2\pi f_{\text{rf}}^2 eU_0 \cos(\varphi_s)}} = \sqrt{\frac{C_0^2 E_0 {\beta_0}^2 \alpha_0 \delta_0^2}{2\pi h eU_0 \cos(\varphi_s)}} = \frac{|\alpha_0|\, c\beta_0 \delta_0}{2\pi f_s}, \tag{2.44}$$

and will be called the "zero-current" bunch length, as it is a single particle effect. The term σ_0 corresponds to the traditional term of the "natural" bunch length [37]. It is common to express the bunch length in units of time indicating the duration of the photon pulse. The rms pulse duration in seconds can be calculated by $\sigma_{0_\text{t}} \approx \sigma_0/c$, which typically is in the order of a few tens of picoseconds. Thoughout this work the bunch length will be referenced as extension as well as duration, depending on the context.

The zero current bunch length derived in this section may be significantly distorted in the

regime of very short bunches by several effects, which will be discussed later.

2.9 Manipulation of the Bunch Length

The circumference of the storage ring as well as the electron energy or the energy spread are design parameters determined by quantities such as desired spectral range, horizontal emittance or number of beam ports. Therefore, manipulation of the equilibrium bunch length for a given machine has to be conducted according to Eq. 2.44 using the relation:

$$\sigma_0 \propto \sqrt{\frac{\alpha_0}{hU_0 \cos(\varphi_s)}}. \tag{2.45}$$

To generate shorter bunches it is possible to either decrease the absolute value of the momentum compaction factor or increase the voltage gradient ($\mathrm{d}U/\mathrm{d}t$). Increasing the voltage gradient is limited by technical boundary conditions of RF cavity design. Whereas h as well as the number of RF cavities are design choices, the voltage gradient can be manipulated during operation by changing U_0.

Manipulation of α_0 is done by exploiting Eq. 2.12, whereas the quadrupole magnet strengths are used to adjust D_{initial} and D'_{initial} at the bending magnets. To reach the limit of the isochronous ring ($\alpha \to 0$) there are two approaches. It is possible to compensate the momentum compaction for every dipole magnet by itself, which makes a zero-crossing of the dispersion function inside the dipole mandatory:

$$\int_0^{L_{\mathrm{dip}}} \frac{D(s)}{\rho(s)} \mathrm{d}s = 0 \quad \forall \quad \text{dipoles}, \tag{2.46}$$

where L_{dip} is the length of the bending magnet.

Another approach is to compensate the path lengthening contributions of different dipoles with each other. The second approach offers more freedom with respect to beam optics, e.g. to generate dispersion free straight sections.

$$\sum^{\mathrm{dipoles}} \int_0^{L_{\mathrm{dip}}} \frac{D(s)}{\rho(s)} \mathrm{d}s = 0. \tag{2.47}$$

Nevertheless, tighter demands on the temporal stability of the used dipole magnet power supplies are imposed. Fluctuations of the power supplies can destroy the delicate balance generated by large contributions with different signs adding up to zero and therefore smear out the resulting bunch length [40].

In a DBA machine, the achromat condition $D(\text{straights}) = D'(\text{straights}) = 0$ has to be given up to achieve isochronous operation, as there is no degree of freedom for the manipulation of α_0. For the MLS operated with zero dispersion in straights the momentum compaction factor is $\alpha_0(\text{DBA}) \approx 0.02$.

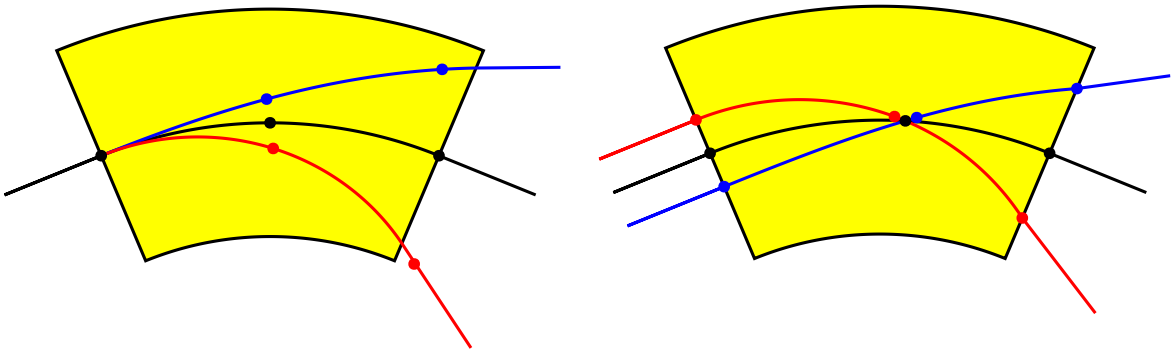

(a) DBA lattice path length

(b) isochronous lattice path length

Figure 2.5: Momentum dependent trajectories inside a sector bending magnet for a DBA setup (a) and isochronous operation (b). The reference trajectory is shown in black as well as trajectories for $\delta > 0$ (blue) and $\delta < 0$ (red). For marked particle positions see text.

Figure 2.5 shows a sketch of chromatic trajectories inside a sector bending magnet. The left part of the figure corresponds to the first dipole of a DBA setup, whereas dispersion generated by the first magnet will be reversed by a second one to generate dispersion-free straight sections. The right part shows the corresponding trajectories for isochronous operation using the approach given in Eq. 2.46. The reference trajectory is shown in black, whereas momentum deviating trajectories are shown for $\delta > 0$ (blue) and $\delta < 0$ (red). All trajectories inside the dipole magnet are of equal length as required for a $\alpha_0 = 0$ lattice. Particle positions are highlighted by markers for the time when the reference particle passes entrance and exit as well as an example position inside the bending magnet.

3 Low-α Operation of the MLS

Operation of synchrotron light sources at a near-zero momentum compaction – "low-α" or "quasi-isochronous" – has become an increasingly demanded mode of operation at many facilities such as ANKA, DIAMOND, MLS, NEW SUBARU, SOLEIL, and SPEAR3 [23, 41–46], strongly motivated by the BESSY II success to achieve stable coherent synchrotron radiation in the THz regime [10]. Various techniques have been developed driven by the motivation to generate short electron bunches in the order of a picosecond. The MLS is the first synchrotron light source, that was optimized for low-α operation already in the design phase [18, 23] regarding the possibility to control higher orders of the momentum compaction factor. An overview of the low-α operation principle applied at the MLS as well as its overall capabilities will be given.

3.1 Low-α User Optics at the Metrology Light Source

General characteristics of the low-α optics applied for user operation at the MLS can be obtained from Tab. 1.1. The momentum compaction factor applied in low-α user optics is $\alpha_0 \approx 1.3 \times 10^{-4}$ (see chapter 4). Figure 3.1 shows the corresponding optical functions $\beta_{x,y}(s)$ and $D_0(s)$. The

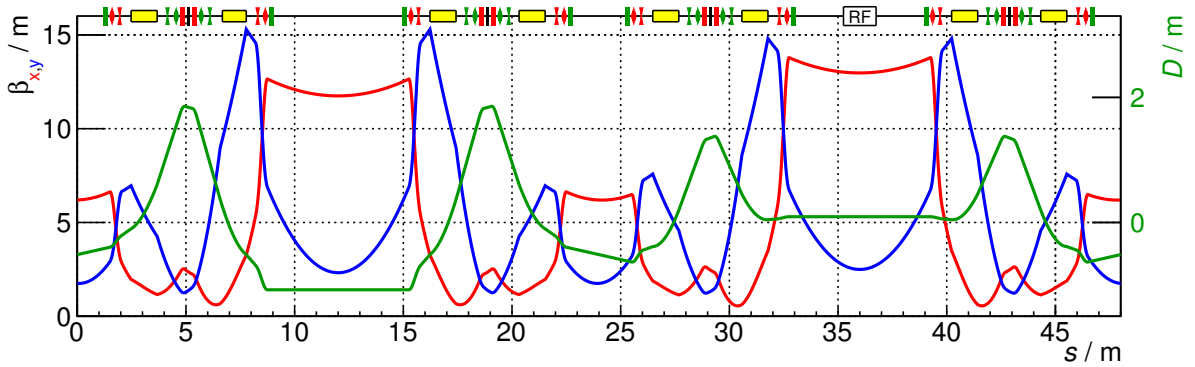

Figure 3.1: MLS magnet optics for low-α user operation: The horizontal (red) and vertical (blue) β-functions as well as horizontal dispersion (green) were measured by fitting a model to the BPM-corrector response matrix (LOCO).

values for the horizontal and vertical β-functions were obtained by applying the LOCO technique [26] and confirmed by the method of individual quadrupole strength variation [28]. The magnet lattice is indicated at the top of the frame including dipole (yellow), quadrupole (red), sextupole (green) and octupole magnets (black).

At the MLS the value of α_0 for the low-α user operation was chosen such to compromise the following conditions:

- reproducibility with respect to dipole and quadrupole magnet strengths,
- target bunch length,
- orbit stability.

The direct measurement of α to control the beam optics setup is usually too time-consuming to be applied permanently during operation (see chapter 4). However, the synchrotron oscillation frequency f_s is a very effective way to characterize the momentum compaction factor of an optics by evaluation Eq. 2.33 when U_0 is known. Figure 3.2(a) shows such a measurement performed in the low-α user mode using a stripline detector. The signal is plotted around a carrier frequency of $6f_{\mathrm{rf}}$. For α_0 towards zero, the measurement of f_s becomes more difficult. This is due to higher

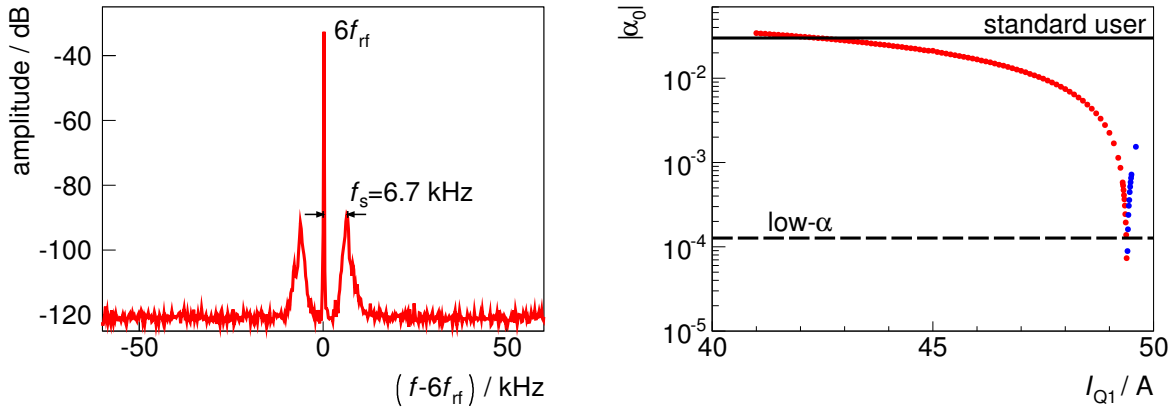

(a) measurement of f_s

(b) sensitivity of α on quadrupole current

Figure 3.2: Measurement of the synchrotron oscillation frequency in the low-α user mode of the MLS (a). Measurement of the impact of an example quadrupole on the momentum compaction factor (b), measured by evaluation of f_s for $\alpha_0 > 0$ (red) and $\alpha_0 < 0$ (blue).

order momentum compaction as well as RF noise distorting the harmonic oscillation. When approaching $\alpha_0 \to 0$ the sensitivity of α on the excitation current in the quadrupole magnets increases. This effect is shown in Fig. 3.2(b) indicating positive (red) and negative momentum compaction (blue), whereas α_0 was estimated by evaluating Eq. 2.33. For the low-α user mode at the MLS a relative quadrupole detuning of about 10^{-4} would result in a zero-crossing of the momentum compaction factor introducing severe distortions of the experimental condition. As the MLS is a designed metrology machine it is equipped with dipole and quadrupole power supplies with a relative accuracy of better than 10^{-5}, which are ideally suited for low-alpha operation.

3.2 Impact of Higher Order Momentum Compaction

When reducing α_0 towards zero, the approximation of a constant momentum compaction factor becomes invalid (see Eqs. 2.11, 2.42 and 2.44). Higher orders of the momentum compaction factor (Eq. 2.10) have to be taken into account modifying the shape of the RF bucket. In addition, for specific momentum compaction functions new buckets are introduced to the longitudinal phase space. These "α-buckets" will be addressed in detail in chapter 5.

A mechanism to control higher orders of the momentum compaction factor by multipole magnets is derived in [47]. To first order, the higher orders of α can be controlled by the corresponding multipole magnets placed at locations with high dispersion:

$$\alpha(\delta) = \underbrace{\alpha_0}_{\text{quadrupole}} + \underbrace{\alpha_1}_{\text{sextupole}} \delta + \underbrace{\alpha_2}_{\text{octupole}} \delta^2 \ldots \tag{3.1}$$

For this reason the MLS is equipped with three families of sextupole magnets placed at locations with linearly independent values of (β_x, β_y, D). Two families are needed to control the transverse chromaticities, whereas the third family enables control of α_1. In addition, the MLS was constructed containing one family of octupole magnets to control α_2 [18].

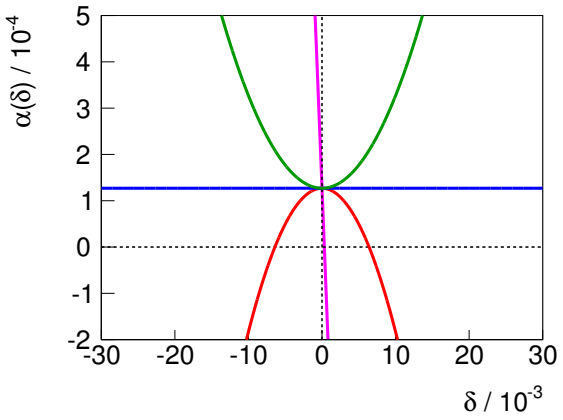

Figure 3.3: Different levels of correction of $\alpha(\delta)$ at the MLS low-α user mode within measurement limits. Without higher order correction (magenta), including sextupole correction (red), including octupole correction (blue) and α_2-overcompensation (green).

Figure 3.3 shows calculations for the momentum dependence of $\alpha(\delta)$ for different setups of the low-α user mode at the MLS. In the first case (magenta), $\alpha_0 = 1.3 \times 10^{-4}$ is shown without controlling α_1 and α_2 by sextupole and octupole magnets. Slope and curvature are mainly given by two sextupole families needed to correct the transverse chromaticities. The second case (red) includes the correction of $\alpha_1 = 0$ by the third sextupole magnet family, whereas the third case (blue) additionally regards the correction of $\alpha_2 = 0$ by octupole magnets. The forth case (green) corresponds to the operational low-α user mode at the MLS using sextupole correction for $\alpha_1 = 0$ as well as octupole correction to intentionally set $\alpha_2 \approx 2$.

The momentum acceptance of the RF-bucket δ_{acc} including higher order momentum compaction can be calculated by starting from Eq. 2.38. The value of the Hamiltonian $\mathcal{H}$ is a constant of motion in the longitudinal phase space (φ, δ). By evaluating $\mathcal{H}$ at the unstable fixed point, which is limiting the RF-bucket, the momentum acceptance at the stable fixed phase can be determined by solving the expression:

$$\mathcal{H}\left(\varphi(\text{unstable fixed point}), \delta(\text{unstable fixed point})\right) = \mathcal{H}\left(\varphi(\text{stable fixed point}), \delta_{\mathrm{acc}}\right), \quad (3.2)$$

see [27] for more details. Assuming $\alpha_0 > 0$ and $U_0 > 0$, the stable fixed point of the RF bucket is located at $(\pi - \varphi_s, 0)$, whereas the the unstable fixed point, defining the separatrix, is located at $(\varphi_s, 0)$. Therefore, Eq. 3.2 can be evaluated to:

$$-\frac{eU_0}{2\pi h}\left[\cos\left(\varphi_s\right) + \varphi_s \sin\left(\varphi_s\right)\right] = -\beta_0^2 E_0 \int \alpha(\delta)\delta \ \mathrm{d}\delta - \frac{eU_0}{2\pi h}\left[\cos\left(\pi - \varphi_s\right) + \left(\pi - \varphi_s\right)\sin\left(\varphi_s\right)\right], \quad (3.3)$$

$$\int \alpha(\delta)\delta \ \mathrm{d}\delta = \frac{eU_0}{\pi h \beta_0^2 E_0}\left[\cos\left(\varphi_s\right) - \left(\frac{\pi}{2} - \varphi_s\right)\sin\left(\varphi_s\right)\right], \quad (3.4)$$

with the commonly used result for the momentum acceptance with $\alpha(\delta) = \alpha_0$:

$$\delta_{\mathrm{acc}}\Big|_{\alpha(\delta)=\alpha_0} = \sqrt{\frac{2eU_0}{\pi h \beta_0^2 E_0 \alpha_0}\left[\cos\left(\varphi_s\right) - \left(\frac{\pi}{2} - \varphi_s\right)\sin\left(\varphi_s\right)\right]}, \quad (3.5)$$

with the scaling law $\delta_{\mathrm{acc}} \propto \sqrt{U_0}$ in the limit of small a synchronous phase. Solving Eq. 3.4 including higher orders of the momentum compaction factor may yield more complex terms.

3.2.1 Increasing RF Bucket Momentum Acceptance Using Octupoles

For $\alpha(\delta) = \alpha_0 + \alpha_1\delta$ the longitudinal phase space is distorted asymmetrically, which in turn leads to an asymmetric shift of momentum acceptance. Therefore, introducing α_1 may increase the momentum acceptance for one sign of momentum deviation while decreasing it for the other sign [48].

In contrast, $\alpha(\delta) = \alpha_0 + \alpha_2\delta^2$ leads to a symmetric distortion increasing or decreasing the momentum acceptance on both sides in δ. For values of α_2 with the same sign as α_0, Eq. 3.4 yields a decrease in momentum acceptance. However, the octupole magnet can be suited to increase the momentum acceptance RF bucket when α_0 and α_2 have opposite signs.

Taking the MLS standard user mode as an example, powering the octupole with maximum excitation ($\alpha_0 = 0.03, \alpha_2 \approx -14$) leads to an estimated increase in RF bucket momentum acceptance of 2.7% following Eq. 3.4. However, using Eq. 3.4 to calculate the momentum acceptance is only valid in a limited regime. When the momentum compaction function $\alpha(\delta)$ crosses zero, additional fixed points are introduced to the longitudinal phase space corresponding to Eq. 2.41. The roots of the momentum compaction function act as outer limits for the momentum accep-

tance given by:

$$\delta_{\mathrm{FP}} = -\frac{\alpha_0}{\alpha_1} \qquad \text{for} \qquad \alpha(\delta) = \alpha_0 + \alpha_1\delta, \tag{3.6}$$

$$\delta_{\mathrm{FP}} = -\frac{\alpha_1}{2\alpha_2} \pm \sqrt{\frac{{\alpha_1}^2}{4\alpha_2^2} - \frac{\alpha_0}{\alpha_2}} \qquad \text{for} \qquad \alpha(\delta) = \alpha_0 + \alpha_1\delta + \alpha_2\delta^2. \tag{3.7}$$

Therefore the momentum acceptance of the RF-bucket can be heavily constrained by the higher orders of α imposing an upper limit given by the roots of the momentum compaction function.

For a momentum compaction function of $\alpha(\delta) = \alpha_0+\alpha_1\delta+\alpha_2\delta^2$ maximum achievable momentum acceptance for the RF bucket on both sides is achieved for $\alpha_1 = 0$. Maximized momentum acceptance is reached when the value of $\mathcal{H}$ at the unstable fixed point in phase is equal to the value of $\mathcal{H}$ at the unstable fixed point introduced by the root of the momentum compaction function. Therefore:

$$\mathcal{H}\left(\varphi_s, 0\right) = \mathcal{H}\left(\pi - \varphi_s, \delta_{\mathrm{FP}}\right). \tag{3.8}$$

It is convenient to rewrite $\alpha(\delta)$ in dependence of $\delta_{\mathrm{FP}} = \sqrt{-\alpha_0/\alpha_2}$ as:

$$\alpha(\delta) = \alpha_2\left(\delta + \delta_{\mathrm{FP}}\right)\left(\delta - \delta_{\mathrm{FP}}\right) = \alpha_0 - \frac{\alpha_0}{{\delta_{\mathrm{FP}}}^2}\delta^2, \tag{3.9}$$

yielding for the Hamiltonian from Eq. 2.39:

$$\mathcal{H}\left(\varphi, \delta\right) = \frac{\beta_0^2 E_0 \alpha_0}{4{\delta_{\mathrm{FP}}}^2}\left(\delta^2 - 2{\delta_{\mathrm{FP}}}^2\right)\delta^2 - \frac{eU}{2\pi h}\left[\cos\left(\varphi\right) + \varphi\sin\left(\varphi_s\right)\right]. \tag{3.10}$$

Solving the system of equations given by Eqs. 3.8 and 3.10, the maximum achievable momentum acceptance being the position of the fixed point follows:

$$\max\left(\left.\delta_{\mathrm{acc}}\right|_{\alpha(\delta)=\alpha_0+\alpha_2\delta^2}\right) = \sqrt{-\frac{\alpha_0}{\alpha_2}} = \sqrt{\frac{4eU_0\left(\cos\left(\varphi_s\right) - \left(\frac{\pi}{2} - \varphi_s\right)\sin\left(\varphi_s\right)\right)}{E_0\alpha_0\pi h{\beta_0}^2}}, \tag{3.11}$$

which is a factor of $\sqrt{2}$ larger than the common acceptance of the RF bucket as given in Eq. 3.5. Therefore, an optimal value of α_2 yields a 41% increase δ_{acc} compare to $\alpha_2 = 0$. In order to achieve maximum RF bucket acceptance by applying α_2 for MLS standard operation at $\alpha_0 = 0.03$ Eq. 3.11 has to be solved for α_2. The yielded octupole strength corresponds $\alpha_2 = -71$, exceeding the design strength by a factor of 4.

Longitudinal phase space distortions by either α_1 or α_2 are shown in Fig. 3.4 at the example of the MLS with $E_0 = 629\,\mathrm{MeV}$, $U_0 = 500\,\mathrm{kV}$ and $\alpha_0 = 0.03$. Energy loss was neglected for reasons of clarity. Figure 3.4(a) shows the phase space distortion for a momentum compaction function of $\alpha(\delta) = \alpha_0 + \alpha_1\delta$ with $\alpha_1 = +1$ (red) and $\alpha_1 = -1$ (blue), whereas Fig. 3.4(b) corresponds to $\alpha(\delta) = \alpha_0 + \alpha_2\delta^2$ with $\alpha_2 = -71$ (red) and $\alpha_2 = -300$ (blue).

The overall bucket structure for momentum compaction functions with zero crossings is discussed in more detail in chapter 5.

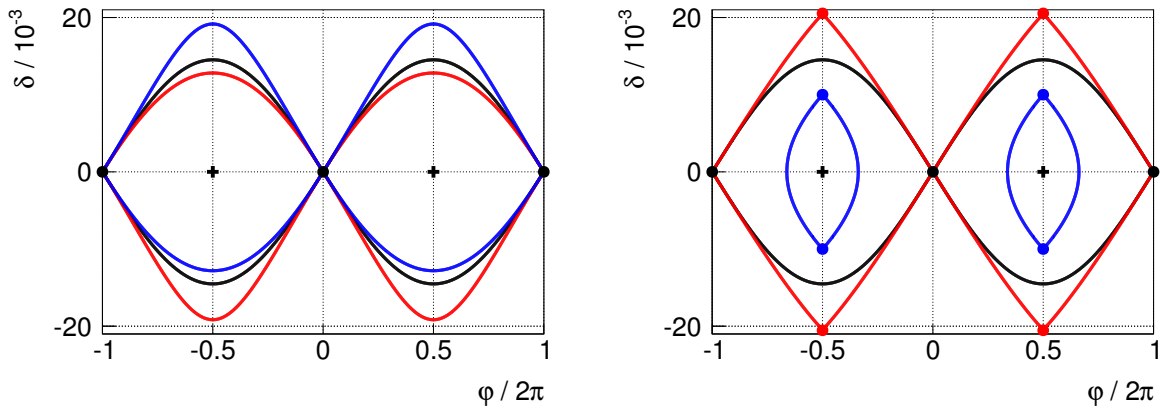

(a) $\alpha(\delta) = \alpha_0 + \alpha_1\delta$ (b) $\alpha(\delta) = \alpha_0 + \alpha_2\delta^2$

Figure 3.4: RF bucket distortion by higher orders of the momentum compaction factor for $\alpha_0 = 0.03$ with $\alpha_1 = \pm 1$ (left: red, blue) respectively $\alpha_2 = -71, -300$ (right: red, blue). The black graph corresponds to the standard RF-bucket for $\alpha(\delta) = \alpha_0$.

3.2.2 Octupole Relevance for Low-α Operation at the MLS

To avoid the reduction of the momentum acceptance by higher order momentum compaction, α_1 and α_2 have to be controlled. Whereas the correction of α_1 is a standard step towards low-α operation the capability to control α_2 by octupole magnets over a large range is a feature unique to the MLS. The octupole magnet is placed in the center of the double bend achromat section. For operation at design beam optics, the dispersion function has its maximum value at this location (Figs. 1.3 and 3.1) to maximize the chromatic impact of the octupole. Figure 3.5 shows a measurement to evaluate the relevance of the octupole magnet for low-α operation. A beam of about 20 mA was stored in the machine, whereas α_1 was adjusted to approximately zero by sextupole magnets. For a single measurement set, α_0 was set to a specific value using the quadrupole magnets. Afterwards a scan of the octupole excitation current over its full range was performed. The quantity measured is the beam lifetime derived from a beam current measurement using a parametric current transformer [49]. This procedure was repeated for seven different values of small momentum compaction factors. Measurements were performed at the standard operation energy of 629 MeV as well as for 250 MeV, which further amplifies the effect of the octupole. Measurements show a negligible change in lifetime over a large range for negative octupole currents. For every α_0 there is a certain octupole current, where the lifetime starts to decrease drastically. This indicates, that there is a threshold for α_2 that is needed to stably store beam. The effect is observed at both energies and corresponds to the deformation of the RF bucket by α_2.

Taking the relation between octupole excitation current and measured α_2 into account (see chapter 4), it is possible to calculate the needed $\Delta\alpha_2$ term introduced by the octupole to stably operate at a given α_0 as shown in Fig. 3.6. A beam lifetime of one hour was used as a threshold indicating stable operation. Data obtained at 629 MeV is shown in blue, whereas red corresponds

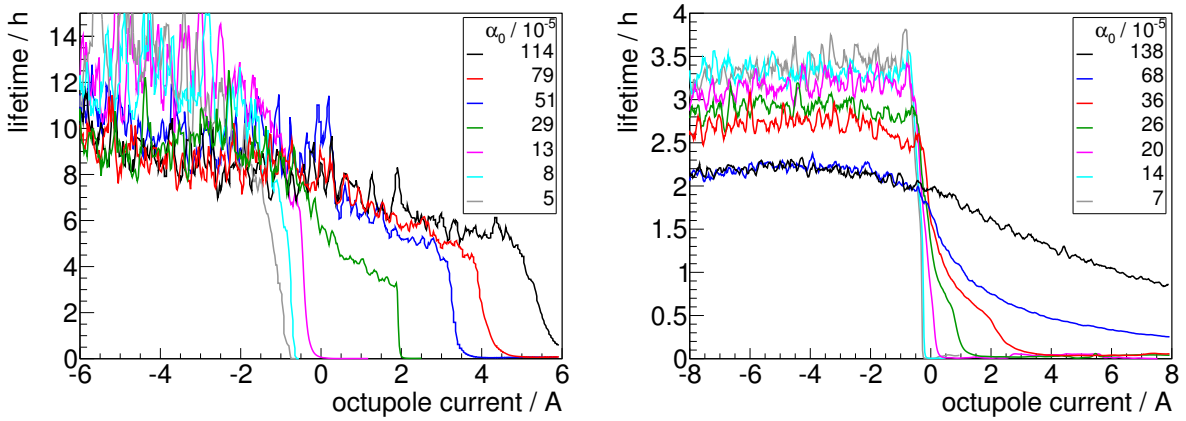

(a) 629 MeV (b) 250 MeV

Figure 3.5: Relevance of the octupole magnet for low-α operation of the MLS. The lifetime is measured in dependence of the octupole excitation current at the standard operation energy of 629 MeV (left) as well as 250 MeV (right).

to 250 MeV. The vertical axis indicates $\Delta\alpha_2$ needed to be introduced by the octupole magnet. The discontinuity in the slope of the blue data is caused by a crossing of the bursting instability threshold (see chapter 6). In the limits of isochronous operation, $\alpha_0 \to 0$, the measurement result at both energies agrees to $\Delta\alpha_2(\alpha_0 = 0) \approx 4.2$. The data for 629 MeV is described in the limit of $\alpha_0 \to 0$ by:

$$\Delta\alpha_{2_{629\,\mathrm{MeV}}} = (-28000 \pm 2000)\,\alpha_0 + (4.3 \pm 0.3)\,, \tag{3.12}$$

whereas the result for 250 MeV is:

$$\Delta\alpha_{2_{250\,\mathrm{MeV}}} = (-8600 \pm 300)\,\alpha_0 + (4.2 \pm 0.1)\,. \tag{3.13}$$

Data analysis throughout the whole work was performed using ROOT [50]. Solving Eqs. 3.12 and 3.13 for $\Delta\alpha_2 = 0$ yields the minimum α_0 that would be accessible without having octupole correction. For the MLS at 629 MeV this limit estimates to $\alpha_{0\,\mathrm{no\ oct\ 629\,MeV}} = (1.5 \pm 0.2) \times 10^{-4}$. Therefore, low-$\alpha$ user operation as presently practiced at the MLS would not be possible without the octupole magnets.

Another relevant advantage of low-α operation with significant α_2 is to backup reproducibility issues. When the RF frequency is not accurately adjusted for α_0 towards zero, the beam may be trapped on largely dispersive orbits eventually hitting the aperture. A large α_2 term with the same sign as α_0 may drastically reduce the dispersive displacement and therefore the probability of beam loss.

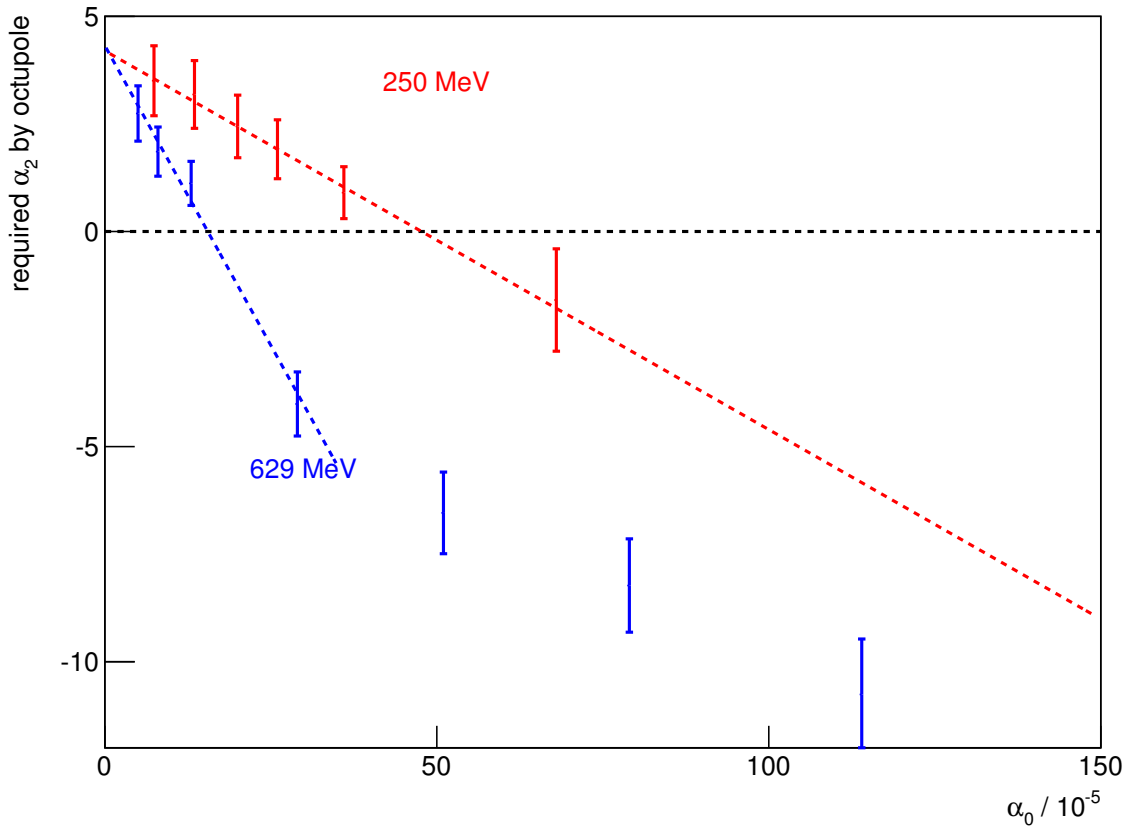

Figure 3.6: Minimum α_2 needed to be introduced by the octupole magnet for low-α operation at the MLS ($\Delta\alpha_2$).

3.3 Operation at Negative Momentum Compaction

Electron storage rings can be operated at negative momentum compaction, e.g. the DIAMOND light source [42]. The involved beam dynamics are slightly different, as particles are rotating the opposite direction in longitudinal phase space. To investigate the effects of the sign of the momentum compaction factor, operation at negative momentum compaction at the MLS had to be established.

At $\alpha_0 < 0$ particles are stored at the opposite synchronous phase, i.e. stable and unstable fixed points of the RF bucket swap their position in phase space. This is due to the sign combination between voltage gradient and momentum compaction factor needed for stable oscillations, which can be deduced from Eq. 2.33. When significant energy loss is present, it is not possible to smoothly change from positive to negative momentum compaction, while keeping the beam stored. Transition with beam can be done by generating a 180° phase jump in the RF voltage, whereas at the same time the sign of α has to be changed [39]. However, the longitudinal phase space has to be restored before particles leave the stable area to be regenerated. When full

energy injection is available, crossing $\alpha_0 = 0$ is usually of little consequence, as it is possible to detune the injector phase and inject directly into the new RF bucket at the new synchronous phase. However, as the MLS is a ramped synchrotron this was not an option. Therefore, a new injection state as well as a new energy ramp with negative momentum compaction had to be established as depicted in Fig. 1.1(b).

Generating the injection state with negative momentum compaction at the MLS turned out to be a challenge not solvable by simply detuning $\alpha_0 = 0.03 \rightarrow -0.01$. Different approaches were taken resulting in injection geometries incompatible with standard operation at positive momentum compaction. Eventually, the generation of the injection state for negative α operation was performed utilizing additional buckets in longitudinal phase space – α-buckets – which will be examined in detail in chapter 5. When crossing $\alpha_0 = 0$ with stored beam, α-buckets turn to common RF buckets. Therefore, it was possible to approach, characterize and optimize the injection state with stored beam before trying to inject. A rough sketch of the procedure to generate the injection state:

- apply octupole to generate a large α_2 with the opposite sign of α_0 ($\alpha_0\alpha_2 < 0$),
- inject beam in RF bucket at $\alpha_0 > 0$,
- reduce absolute value of α_0 to the point of domination of α_2 (e.g. lifetime reduction),
- inject beam again by taking care of storing beam in alpha buckets,
- cross to negative α_0, i.e. beam previously stored in RF buckets is lost, beam from alpha buckets is conserved and fills the newly formed RF bucket,
- increase the absolute value of $\alpha_0 < 0$,
- correct beam parameters: response matrix measurement, orbit correction, tune and chromaticity,
- adjust storage ring energy to account for a changed dispersion function at the injection point,
- finally beam could be injected into the RF bucket of the new beam optics with $\alpha_0 < 0$.

The beam optics characterization of the injection state for operation at negative momentum compaction is given in Fig. 3.7, whereas the applied working point corresponds to operation at positive momentum compaction.

Negative momentum compaction is now an available operational mode of the MLS. Optical functions of negative low-α correspond to the ones from positive low-α as shown in Figs. 1.1(b) and 3.1, as for small $|\alpha_0|$ the change in $\beta_{x,y}(s)$ an $D(s)$ becomes negligible.

For low-α user optics at the MLS without octupole correction, the uncorrected momentum compaction function (see red graph in Fig. 3.3) features a negative curvature, i.e. $\alpha_2 < 0$. A direct result is the momentum acceptance reduction as described in section 3.2. An advantage of operation at negative momentum compaction is the correspondence of the signs of α_0 and the residual α_2 for zero octupole excitation. Therefore, in the limit of isochronous operation there

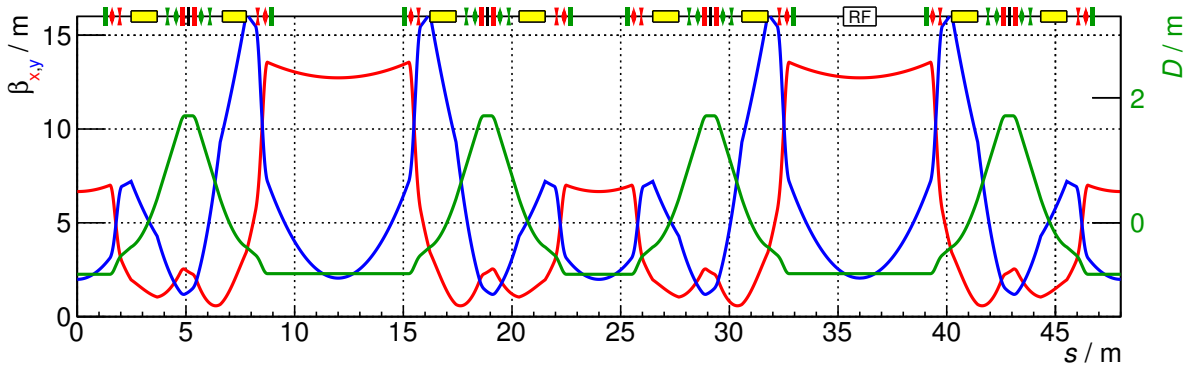

Figure 3.7: MLS magnet optics for negative α operation: The horizontal (red) and vertical (blue) β-functions as well as horizontal dispersion (green) were measured by fitting a model to the BPM-corrector response matrix (LOCO).

is no reduction of momentum acceptance and $\alpha_0 \to 0$ can be achieved without beam loss and without applying octupole correction.

3.4 Emittance in Low-α

The emittance ε of the beam is a quantity that describes the area occupied by the beam in phase space. In electron storage rings, emittance is the result of an equilibrium between quantum excitation and radiation damping. Stochastic emission of photons leads to an energy spread as well as a continuous excitation of transverse oscillations [37]. Commonly the emittance in the horizontal and longitudinal plane are of interest. For calculations, it is convenient to use the following simplified synchrotron radiation integrals as given in [31, 51]:

$$\mathcal{I}_1 = \oint \frac{D(s,\delta)}{\rho} \mathrm{d}s = C_0 \alpha\left(\delta\right), \tag{3.14}$$

$$\mathcal{I}_2 = \oint \frac{1}{\rho^2} \mathrm{d}s \overset{\text{MLS}}{\approx} 4.112 \text{ m}^{-1}, \tag{3.15}$$

$$\mathcal{I}_3 = \oint \frac{1}{|\rho^3|} \mathrm{d}s \overset{\text{MLS}}{\approx} 2.691 \text{ m}^{-2}, \tag{3.16}$$

$$\mathcal{I}_{4\text{w}} = \sum^{\text{dipoles}} \left[\frac{D_{\text{initial}} \tan\theta_{\text{initial}}}{\rho^2} + \int \frac{D}{\rho^3}\left(1 + 2\rho^2 k\right) \mathrm{d}s + \frac{D_{\text{final}} \tan\theta_{\text{final}}}{\rho^2} \right] \overset{\text{MLS}}{\approx} -0.2253 \text{ m}^{-1}, \tag{3.17}$$

$$\mathcal{I}_5 = \oint \frac{\mathcal{H}}{|\rho^3|} \mathrm{d}s, \tag{3.18}$$

whereas $\mathcal{I}_{4\mathrm{w}}$ is a the special case of $\mathcal{I}_4$ for a wedged bending magnet. The chromatic invariant $\mathcal{H}$, not to be confused with the Hamiltonian, is given by [31]:

$$\mathcal{H}(s) = \beta_x(s)D'(s)^2 + 2\alpha_x(s)D(s)D'(s) + \gamma_x(s)D(s)^2. \tag{3.19}$$

The vertical plane was omitted, as $\rho_y \approx \infty$. The values are calculated for the MLS R-bend magnets with $\rho_x = 1.528$ and $\phi_{\mathrm{bend}} = \pi/4$. Equilibrium energy spread can then be estimated by [31]:

$$\left(\frac{\sigma_E}{E_0}\right) = \delta_0 = \sqrt{\frac{55}{32\sqrt{3}}\frac{\hbar c}{mc^2}\gamma^2\frac{\mathcal{I}_3}{2\mathcal{I}_2 + \mathcal{I}_4}} \overset{\text{standard user}}{\approx} 4.4 \times 10^{-4}, \tag{3.20}$$

$$\tag{3.21}$$

as well as the horizontal emittance:

$$\varepsilon_x = \frac{55}{32\sqrt{3}}\frac{\hbar c}{mc^2}\gamma^2\frac{\mathcal{I}_5}{\mathcal{I}_2 - \mathcal{I}_4} \overset{\text{standard user}}{\approx} 120\,\mathrm{nm\,rad}. \tag{3.22}$$

The electron energy spread is only dependent on the electron energy, bending radius and bending angle, with the exception of modifying $\mathcal{I}_4$ by sections with $\rho^2 k \neq 0$ e.g. Robinson wigglers [52, 53]. However, at the MLS there is currently no section with significant $\rho^2 k$ and therefore the variation of $\mathcal{I}_{4w}$ with D is negligible. In contrast $\mathcal{H}(s)$ may vary for different beam optics and in consequence $\mathcal{I}_5$. Horizontal emittance as well as momentum compaction factor are linked to the dispersion function inside the bending magnets by Eqs. 2.12 and 3.22. Therefore both quantities cannot be varied independently of each other.

Nevertheless, the ability to change the emittance in low-α operation is a desirable option. First, users of incoherent synchrotron radiation are interested in low-emittance operation to increase brilliance. Second, users of coherent synchrotron radiation in the THz regime are usually not interested in a small transverse beam size. Therefore, high-emittance is a requested mode of operation too, as the beam lifetime in the Touschek-limit roughly scales with $\tau_{\mathrm{Touschek}} \propto \varepsilon$.

To fully explore the optic capabilities of the MLS, an algorithm was written [54] following the ideas of [55]. The basic idea is to do a numerical brute force scan for stable solutions in the scope of linear beam optics. The strengths of all quadrupole magnets of the lattice is varied within limits in nested loops. To keep the required computation time acceptable the 24 single quadrupole magnets were grouped together into five different families as depicted in Fig. 3.8(a) accounting for the 4-fold symmetry of the MLS. Two quadrupoles in the middle of the achromat Q1 were treated as one family, as they are spatially very close and therefore the optical functions are very similar. The algorithm was written in Fortran and optimized for runtime. To save computation time a vertically decoupled motion was assumed. A sketch of the algorithm is given by:

1. check vertical revolution matrix for stability criterion,
2. check horizontal revolution matrix for stability criterion,
3. apply feasibility filters: $\beta_{x,y} \leq 20$ m, $|D| \leq 2$ m,

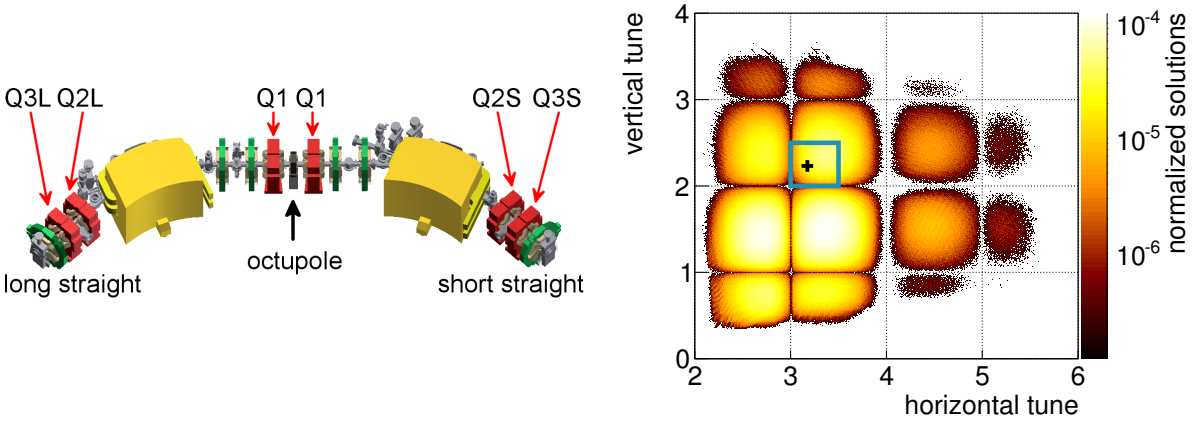

(a) quadrupole synopsis

(b) regions of stability

Figure 3.8: Left: DBA segment of the MLS containing dipole (yellow), quadrupole (red), sextupole (green) magnets and an octupole magnet (black) in the center. Right: Regions of stability for the MLS lattice in the tune diagram. The black cross marks the standard working point, whereas the blue box marks an easily accessible area.

4. calculate optics quantities of interest,

5. calculate Touschek lifetime [25, 54],

whereas quantities such as chromaticities or dynamic aperture are to be determined in further steps.

In a first rough scan the quadrupole strengths were varied within the full design range including polarity reversal, which corresponds to $k = -6\,\mathrm{m}^{-2} \ldots 6\,\mathrm{m}^{-2}$ at an electron energy of 629 MeV. Constant step size was used for all quadrupole excitation strengths. The first scan covered about 10^{12} optics configurations, whereas about 2×10^6 solutions passed feasibility filters and were saved to a database. Scan runtime on a 2.66 GHz single core machine was about 200 h. The 5-dimensional scan result is depicted in Fig. 3.8(b) as a projection into the transverse tune plane. The color code indicates the number of solutions found in one bin normalized by the total number of solutions found in the scan. The blue box marks the currently used tune quadrant at the MLS. This area is easily accessible for investigation and operation as it is possible to transit from standard operation, while keeping the beam stored. The database was analyzed with respect to the quadrupole ranges yielding solutions in the blue area defining new scan ranges for the individual quadrupole families. As a consequence the step size could be decreased by a factor of four without significantly increasing the runtime generating a much larger database containing 2×10^8 optics configurations.

Figure 3.9 shows projections of global and refined scan results in the ε-α-plane. Standard user operation is marked by a black cross, whereas the low-α user operation is marked by a red cross. Horizontal emittance was calculated using Eqs. 3.22 whereas the momentum compaction

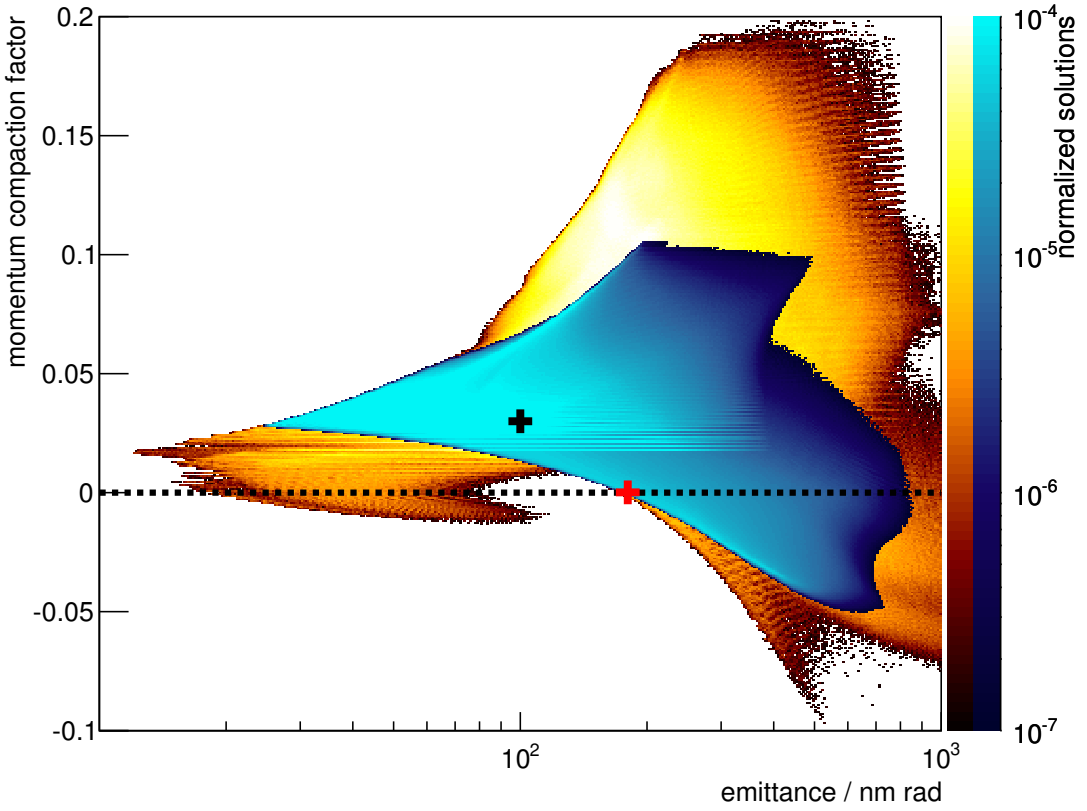

Figure 3.9: Optic capabilities of the MLS to adjust momentum compaction as a function of horizontal emittance. The black cross marks standard user operation whereas the red cross marks low-α user operation. A global scan (yellow) as well as a data subset within the currently operated tune quadrant (blue) are shown.

factor was estimated by evaluating the revolution matrix R [31]:

$$\frac{\Delta C}{C_0} = \frac{R_{51}D + R_{52}D' + R_{56}}{C_0}. \tag{3.23}$$

The histogram color code corresponds to the solution density as described in Fig. 3.8(b). The blue color code is a data subset and contains all solutions found in a specific tune quadrant marked by the blue area in Fig. 3.8(b). A direct finding is the lack of existence for solutions capable of low-α operation at the design emittance of $\approx 100\,\mathrm{nm\,rad}$. Such an operation mode could be used by both user groups, those interested in brilliance and those interested in short pulses or coherent synchrotron radiation. In addition, the currently operated low-α user mode is ideal with respect to minimum emittance in the applied tune quadrant. However, it is possible to operate the MLS in low-α-low-emittance by increasing the horizontal tune by about +1.5.

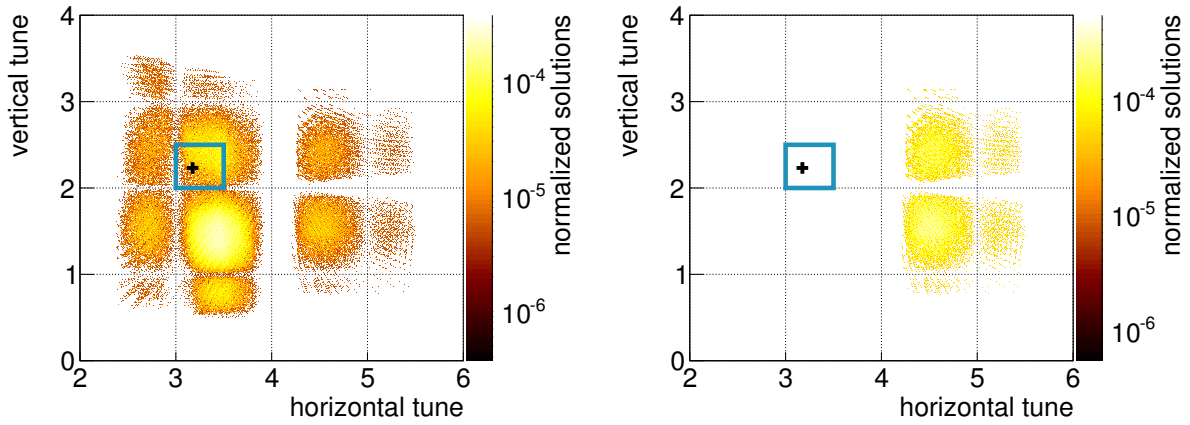

(a) $|\alpha_0| \leq 0.002$

(b) $|\alpha_0| \leq 0.002$ & $\varepsilon < 100\,\mathrm{nm\,rad}$

Figure 3.10: Low-α capable optics solutions for the MLS lattice with $|\alpha_0| \leq 0.002$ (a). Low-α-low-ε filtered results with $|\alpha_0| \leq 0.002$ as well as $\varepsilon < 100\,\mathrm{nm\,rad}$ (b).

In Fig. 3.10(a) a subset of the global scan data is shown capable of low-α operation, whereas low-α capability was defined as $|\alpha_0| \leq 0.002$ In Fig. 3.10(b) an additional filter condition of $\varepsilon < 100\,\mathrm{nm\,rad}$ was applied. To investigate this mode of operation a new injection state as well as an energy ramp have to be created, which is work in progress at the MLS.

High-α optics with a momentum compaction of $\alpha_0 \approx 0.1$ have been experimentally verified. However, at maximum RF voltage the longitudinal tune of 0.032 is still restricted well within the regime of longitudinal weak focusing $Q_s \ll 0.5$ [56].

To further exploit beam optics optimization it seems promising to break the storage ring symmetry. However, the computational time will be greatly increased, generating the need to parallelize the code. An alternative technique to brute force scanning is the use of optimization techniques like multi objective genetic algorithms (MOGA) [57]. However, in this case a well defined optimization goal as well as figure of merit is required.

3.5 Dynamic Aperture in Low-α

Betatron and synchrotron oscillation amplitudes of particles trapped in storage rings are subject to various aperture limitations. These limitations apply to the transverse plane in the form of collision with vacuum chamber walls defining the minimum and maximum displacement from the reference orbit. Particle dynamics in the longitudinal plane may be coupled to the transverse plane introducing a momentum dependence. The momentum acceptance is defined as the maximum momentum deviation leading to a stably stored particle motion. These aperture limitations restrict essential storage ring characteristics such as injections efficiency or beam lifetime [58].

Introduction of nonlinear elements such as chromatic or harmonic sextupole magnets or even higher multipoles yields a nonlinear particle motion. At sufficiently large amplitudes the regime

of chaotic dynamics is entered. The oscillation amplitude available to stably store particles is therefore dependent on the applied multipole strength. However, eventually particles can only be lost by collision with the vacuum chamber walls, therefore this "dynamic aperture" is not an independent magnet lattice parameter.

To investigate the aperture limitation at the MLS a single particle tracking was set up using the PTC extension of MAD-X [59]. Six-dimensional element-by-element tracking was conducted observing horizontal, vertical and longitudinal particle motion.

Figure 3.11 shows tracking results for standard user operation with transverse chromaticities corrected to $\xi_{x,y} = 1$. Tracking was started at the septum magnet ($s = 0$ in Fig. 1.3) using nested loops to vary initial particle coordinates x_{initial}, y_{initial} and δ_{initial} with $x'_{\text{initial}} = y'_{\text{initial}} = \varphi_{\text{initial}} = 0$. Survival of 10000 turns was used as stability indicator corresponding to approximately 10% damping time at an electron energy of 629 MeV. Figure 3.11(a) shows the dynamic aperture, i.e. a large geometric aperture of $|x| \leq 0.1$ m and $|y| \leq 0.1$ m was assumed for the tracking. Figure 3.11(b) shows tracking results using realistic vacuum chamber dimensions including the standard vacuum chamber (solid black), insertion device chamber (dashed black) as well as septum magnet chamber (dotted black). Apertures are scaled by a factor of $\beta_{\text{septum}}/\beta$ in both planes. Tracking simulations as well as experimental results indicate a negligible dynamic aperture, i.e. standard user operation at the MLS is limited by physical apertures.

When operating a storage ring in quasi-isochronous mode, at least α_1 has to be corrected to zero. Usually, adjusting α_1 is performed by applying an additional sextupole family. Therefore, the dynamic aperture in low-α may be affected. To investigate this effect, additional tracking simulations using a model of the low-α user mode at the MLS were performed. In contrast to standard user operation, transverse chromaticities are set to $\xi_{x,y} = 0$ to avoid amplitude dependent orbit lengthening (see section 2.4). In addition, octupole correction was applied to adjust α_2 to a small positive value.

The dynamic aperture in low-α operation depicted in Fig. 3.12(a) is smaller than in standard user operation (see Fig. 3.11(a)). However, it is still significantly larger than the aperture imposed by the vacuum chambers depicted in Fig. 3.12(b), which corresponds to experimental observations at the storage ring. Therefore, dynamic aperture is not a limiting effect for low-α operation.

In addition to correcting chromaticity, chromatic sextupole magnets distort the harmonic potential well trapping the beam. As a result, the oscillation frequency become amplitude dependent. If required, storage rings are equipped with "harmonic sextupoles" operating in dispersion-free or low-dispersion sections. Harmonic sextupoles are able to compensate for the amplitude dependence of the tune introduced by chromatic sextupoles. At the MLS, harmonic sextupoles are not used. Therefore, there is an amplitude dependent tune shift.

Figure 3.13 shows the on-momentum amplitude dependent tune spread at the working point for standard user operation (Fig. 3.13(a)) and low-α operation (Fig. 3.13(b)) corresponding to dynamic aperture limitation (blue) and vacuum chamber limitation (red). For low-α operation the amplitude dependent tune shift is significantly smaller than in standard user operation and therefore not a limiting feature.

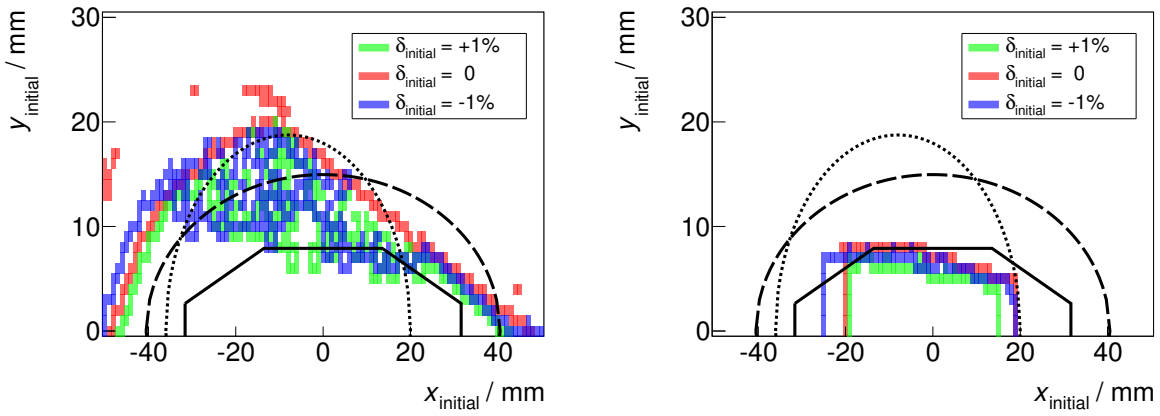

(a) dynamic aperture

(b) geometric aperture

Figure 3.11: Aperture in standard user operation: Dynamic (left) and physical (right) aperture obtained by single particle tracking for standard user operation at the MLS: on momentum (red), $\delta = -0.01$ (green) and $\delta = 0.01$ (blue). Physical aperture limitations are given by standard vacuum chamber (solid black line), insertion device vacuum chamber (dashed black line) and septum (dotted black line).

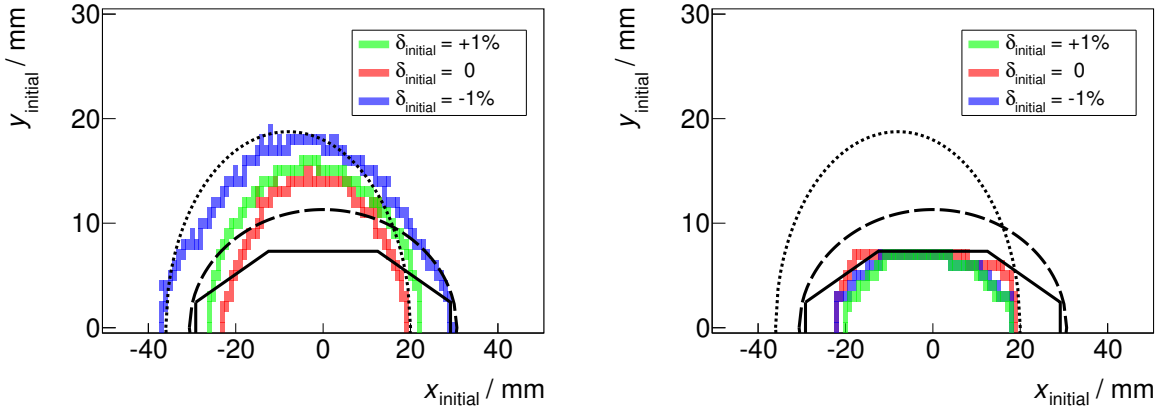

(a) dynamic aperture

(b) geometric aperture

Figure 3.12: Aperture in low-α user operation: Dynamic (left) and physical (right) aperture obtained by single particle tracking for low-α operation at the MLS: on momentum (red), $\delta = -0.01$ (green) and $\delta = 0.01$ (blue). Physical aperture limitations are given by standard vacuum chamber (solid black line), insertion device vacuum chamber (dashed black line) and septum (dotted black line).

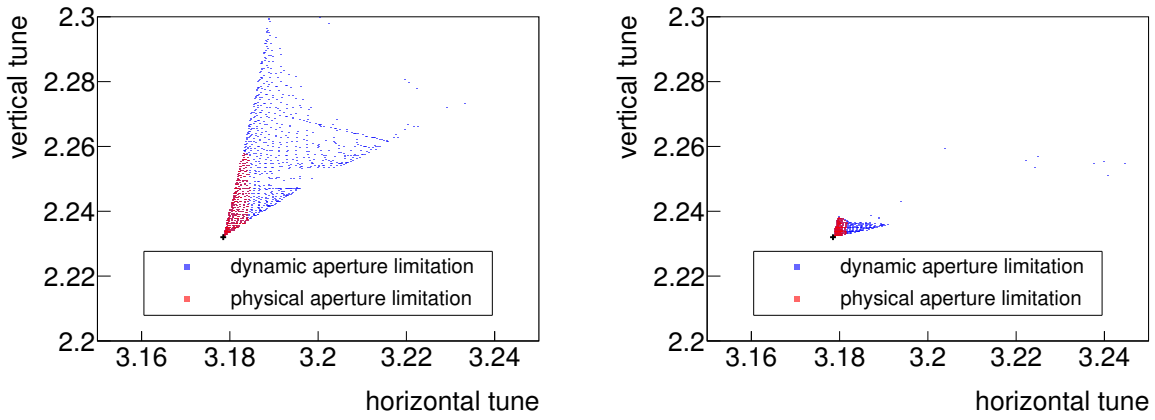

(a) standard user

(b) low-α

Figure 3.13: Amplitude dependent tune shift for standard user operation (left) and low-α operation (right) at the MLS. Blue corresponds to dynamic aperture limitation, whereas red corresponds to limitation due to the vacuum chamber (see Figs. 3.11 and 3.12).

3.6 Horizontal-Longitudinal Coupling

Oscillation of particles in the longitudinal plane can be coupled to the horizontal plane. One coupling mechanism is established by the behaviour of the dispersion function at the RF cavities. With a non-negligible horizontal-longitudinal coupling it could be possible to introduce emittance originating from the horizontal plane to the longitudinal plane. This effect is similar to the well known vertical emittance increase due to horizontal-vertical coupling in the transverse plane and could potentially smear out small bunch lengths or substructures. Although this effect could not be measured at the MLS, it can be observed in tracking simulations. Therefore it was decided to tune the dispersion as well as its derivative at the RF cavity towards zero for all optics considered for low-α operation as depicted in Fig. 3.1.

Another mechanism coupling horizontal and longitudinal plane is closely connected to the value of the chromatic invariant $\mathcal{H}$ given in Eq. 3.19 at the point of observation [35, 60, 61]. Similar to an increase of the beam size in the transverse plane due to energy spread in combination with D at the point of observation, there is an analogue effect increasing the bunch length through transverse emittance. The effect originates from the rotation of the reference system against the laboratory frame. For the simplified case of an infinitesimal short bunch starting in a section with $\mathcal{H} = 0$, a bunch lengthening inside the first dipole is introduced, which is dependent on the bending angle. However, this effect is reversible and localized to points of observation with a non-vanishing $\mathcal{H}$. Therefore, at the RF cavity of the MLS the bunch remains short.

As the MLS features strong bending magnets with $\varphi_{\mathrm{bend}} = \pi/4$ the chromatic invariant may increase to large values. In addition, in low-α operation the bunch length is reduced to small

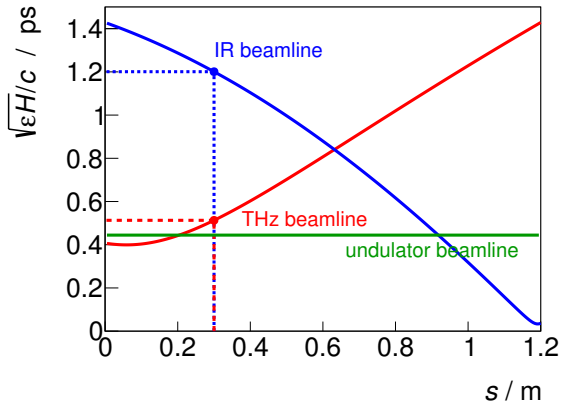

Figure 3.14: Value of the chromatic invariant $\mathcal{H}$ at different observation points of the MLS. The behavior inside the dipole of the THz beamline (red), infrared beamline (blue) as well as the insertion device section (green) are shown. The points of observations are marked by dashed lines.

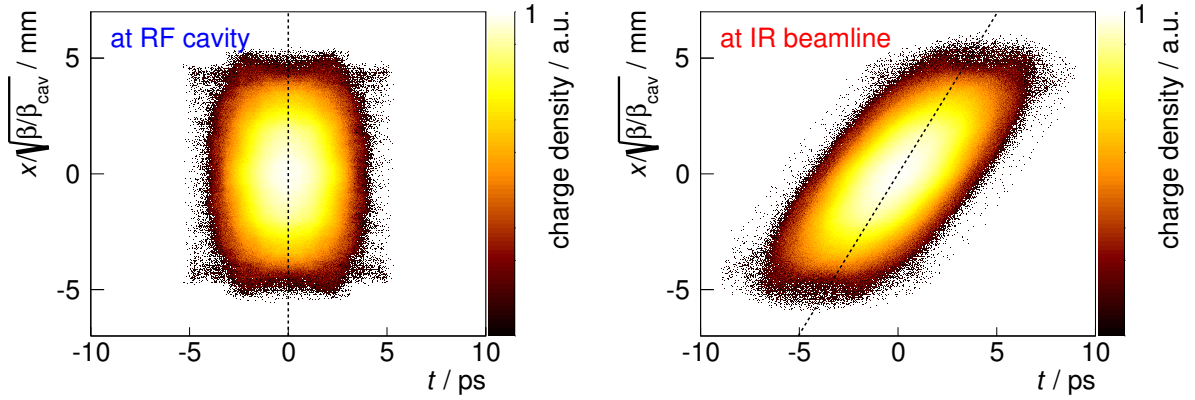

(a) observed at RF cavity

(b) observed at IR beamline

Figure 3.15: Particle tracking for MLS low-α user operation with observation points at RF cavity (left) and IR beamline (right). The tilt corresponds to the viewing angle introduced by the dipole magnet rotating the reference system. The dashed line in both plots indicates a transversely spread but infinitesimal short bunch.

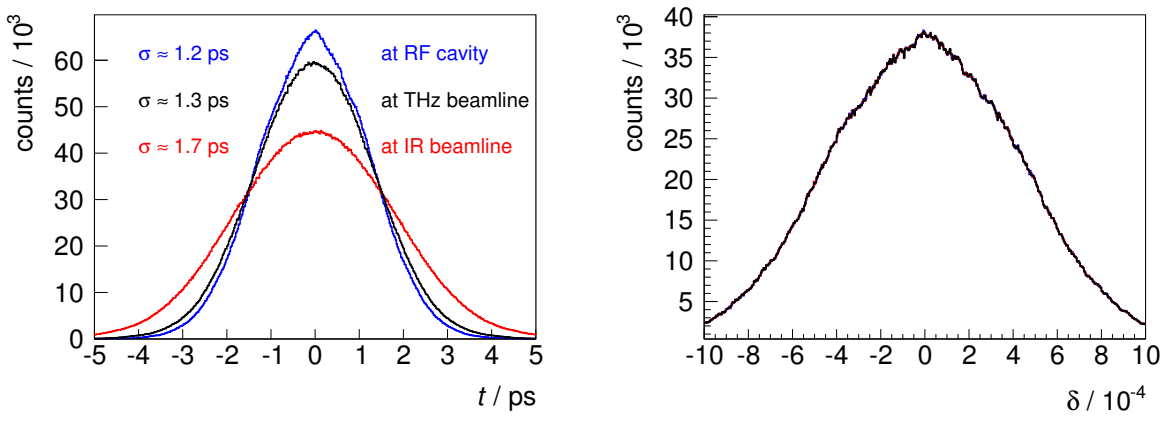

(a) bunch length

(b) energy spread

Figure 3.16: Bunch length (left) and energy spread (right) in low-α user operation at different observation points obtained by single particle tracking for 150 damping times. Colors correspond to observation at RF cavity (blue), at THz beam port (black) and IR beam port (red).

values in the order of $\sigma_0 \approx 1\,\mathrm{ps}$. Bunch lengthening can be calculated by evaluating [35]:

$$\sigma^2 = {\sigma_0}^2 + \varepsilon\mathcal{H}. \tag{3.24}$$

Figure 3.14 shows a calculation of the bunch lengthening for an infinitesimal short bunch at the RF cavity ($\sigma_0 = 0$) introduced by the rotation of the bunches inside the dipole magnets. The chromatic invariant was calculated based on LOCO measurements performed in low-α user operation. For the dipole magnet of the THz beamline (red) there is a rising chromatic invariant and therefore a bunch lengthening. The value of $\mathcal{H}$ at the point of observation corresponds to $\mathcal{H}_{\mathrm{THz}} \approx 0.12$ m. At the IR beamline, located at a dipole magnet with a falling chromatic invariant, the value is $\mathcal{H}_{\mathrm{THz}} \approx 0.67$ m. The order of magnitude of the bunch lengthening effect usually is negligible as most light sources operate with low emittance and longer bunches, e.g. BESSY II: $\sqrt{\varepsilon\mathcal{H}} \approx 100\,\mathrm{fs}$. However, the MLS is operating at a comparatively large emittance of $\varepsilon \approx 200\,\mathrm{nm\,rad}$ in low-α at targeted bunch lengths of $\sigma_0 \approx 1\,\mathrm{ps}$. Therefore, this is a potentially limiting effect for the bunch length – dependent on the point of observation.

Figure 3.15 shows particle tracking results for MLS low-α user operation to investigate the relevance of the observation point. Particles were tracked in six-dimensional phase space including quantum excitation and radiation damping for about 150 damping times. RF cavity, THz beam port as well as IR beam port were chosen as observation points . Figure 3.15(a) shows an upright particle distribution in the t-x-plane. The root mean square value of the longitudinal coordinate is $\sigma_{\mathrm{cav}} = (1.2 \pm 0.1)$ps an corresponds to the value predicted by Eq. 2.44. However, at THz and IR beam port, particle distribution is sheared as shown in Fig. 3.15(b). Therefore the bunch length is increased to values of $\sigma_{\mathrm{THz}} = (1.3 \pm 0.1)$ps and $\sigma_{\mathrm{IR}} = (1.7 \pm 0.1)$ps. The dashed line in both plots corresponds to an infinitesimal short but transversely spread bunch

in the local reference system. Longitudinal bunch profiles at all points of observation are given in Fig. 3.16(a), where the bunch lengthening at IR beamline is clearly visible. At the THz beamline, the bunch lengthening is negligible, however, this may change for operation with even smaller α_0. As a cross reference particle distributions in the δ-plane are given in Fig. 3.16(b). At all observation points the energy spread is the same, which is expected but indicates the coupling nature of the effect.

At the IR beamline this is the dominant bunch lengthening effect, which can be observed by streak camera measurements – see section 6.2. However, to the time of writing this thesis, this effect does not seem to be hampering experiments at the THz beamline.

3.7 Longitudinal Radiation Excitation

Photon emission in electron storage rings is a stochastic process. Therefore, in principle it matters for the longitudinal phase delay of an electron whether photon emission occurs right at the beginning of a turn or right before its end. Starting from the point of emission, this electron will see a "partially different momentum compaction factor" for the rest of the turn. Usually this effect can be neglected leading to the commonly used approximation of continuous phase advance as used in Eq. 2.28. However, in the regime of very short bunches, stochastic emission may smear out the bunch length or sub-structures in longitudinal bunch density and therefore imposes a lower boundary for the bunch length. The effect was treated analytically in [38] yielding a lower boundary for the bunch length based on a single particle effect.

To evaluate the impact of longitudinal radiation excitation at the MLS, tracking simulations were performed using MAD-X. Figure 3.17 shows the result of a bunch length variation by a drastic increase of RF cavity voltage. The higher orders α_1, α_2 of the momentum compaction factor as well as the transverse chromaticities ξ_x, ξ_y were adjusted to zero by sextupole and octupole elements. Simulation was performed at $E = 629\,\mathrm{MeV}$ for standard user operation $\alpha_0 = 0.03$ (hollow squares) as well as for low-α user operation $\alpha_0 = 1.3 \times 10^{-4}$ (dots). Bunch length (red) and energy spread (blue) were calculated by observing a single particle for 10^7 turns, which corresponds to about 150 damping times. For standard user (blue) the effect could not be observed due to the limitation of longitudinal weak focusing $Q_s \ll 0.5$. For low-α user operation the limitation due to longitudinal radiation excitation is approximately 120 fs. When the bunch length limitation is approached, energy spread starts to increase significantly.

3.8 Beam Based Measurement of the Acceleration Voltage

The accelerating voltage respectively the voltage gradient experienced by the electrons in RF cavities is usually not precisely known.

It is possible to calculate the field amplitude U_0 by measuring the RF power coupled into the cavity as well as the reflected power. When the shunt impedance R of the cavity is known, the field amplitude may be estimated by $|U_0| \approx \sqrt{2P_{\mathrm{loss}}R}$. The shunt impedance of the cavity at the MLS is $R = 3.4\ \mathrm{M\Omega}$ [24]. In addition, at the MLS there is an antenna in the RF-cavity to measure off-axis field amplitude, from which the effective on-axis acceleration voltage gets calculated.

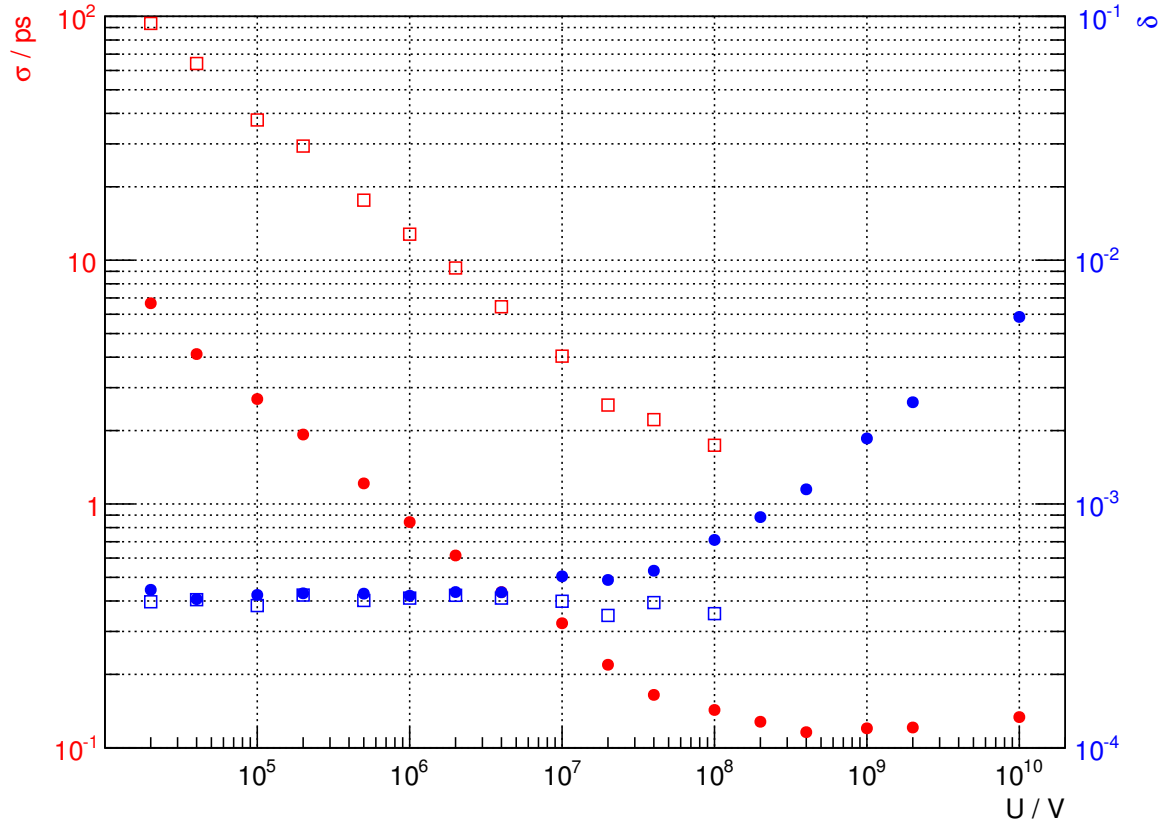

Figure 3.17: Tracked bunch length (red) and energy spread (blue) as a function of RF cavity voltage at the MLS. Tracking was done for the standard user mode (hollow squares, $\alpha_0 = 0.03$) and for low alpha user operation $\alpha_0 = 1.3 \times 10^{-4}$ (dots).

For longitudinal beam dynamics the integral energy loss or gain over one turn plays an important role. The scaling of ${f_s}^2 \propto U_0$ for negligible synchronous phases can be used to calibrate the voltage scaling by application of Eq. 2.33. However, the voltage is then undefined by an unknown factor. The absolute value of U_0 can be calibrated when all other quantities of Eq. 2.33 are known, which applies for the MLS (see chapter 4). Figure 3.18(a) shows a measurement of the synchrotron oscillation frequency as a function of RF voltage conducted in standard user operation. A fit invoking the knowledge of f_{rf}, E and α_0 yields the calibration factor:

$$U = (1.055 \pm 0.004)\, U_{\mathrm{meas}}, \tag{3.25}$$

whereas the measurement error is dominated by the error introduced through the measurement of the RF voltage U_{meas}.

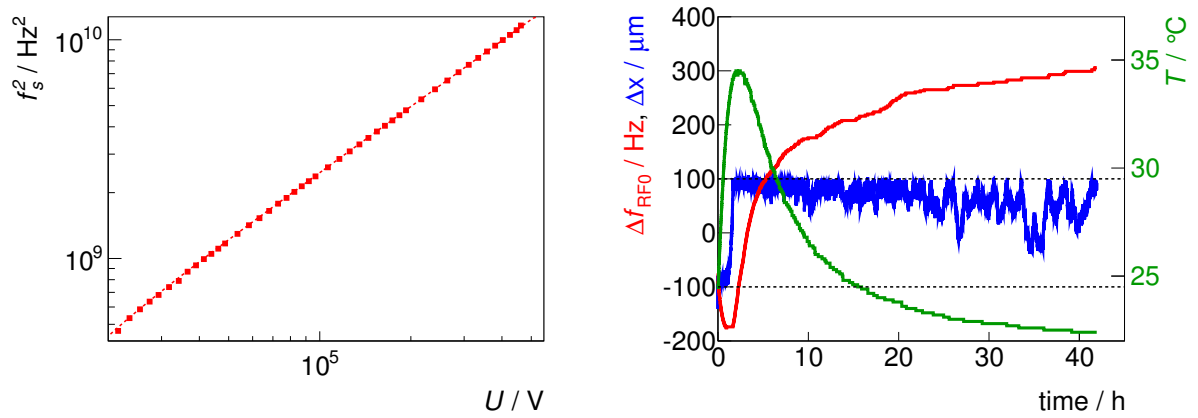

(a) f_s: voltage scaling

(b) RF frequency based orbit control during low-α run

Figure 3.18: Measured synchrotron oscillation frequency in dependence applied cavity voltage (left). RF frequency feedback used for low-α operation at the MLS (right) showing RF frequency detuning (red), dispersive displacement (blue) and temperature measured at a selected dipole magnet chamber (green).

3.9 RF Frequency Controller

Orbit distortions such as thermal drifts of bending or corrector magnets may significantly increase in impact for low-α operation. An orbit distortion in low-α will not only introduce a beam displacement, but also change the orbit length and therefore the revolution time. The change in orbit length is then propagated by a factor of $1/\alpha$ to a dispersive displacement following Eqs. 2.5 and 2.8:

$$x_D \approx \frac{D}{\alpha}\frac{\Delta C}{C}. \tag{3.26}$$

Therefore, orbit distortions in low-α usually show up as dispersive orbit pattern. For investigation of momentum dependent momentum compaction effects in low-α operation, it is crucial to be able to stabilize the momentum deviation, i.e. the dispersive displacement. Therefore, for low-α operation at the MLS an RF frequency controller was introduced as an replacement for the traditional response matrix based orbit correction. The RF frequency controller uses an estimate for the dispersive displacement of the beam to stabilize its position in δ by adjusting the RF frequency. The following devices may be used to deliver input parameters for the RF frequency feedback:

- average horizontal displacement at BPMs with high dispersion,
- horizontal displacement at a single high sensitivity, high dispersion BPM,
- optical source point imaging system with a dispersive point of view.

For low-α user operation, usually at ring currents greater than 1 mA, the BPM based RF frequency feedback is well established. However, for small current experiments, e.g. 1 µA single bunch, correction based on the optical source point imaging system is necessary.

Figure 3.18(b) shows the RF frequency detuning (red) applied by the feedback during a low-α user run at the MLS. The blue graph corresponds to the average horizontal displacement of the beam in the center of the achromat segments where the dispersion is at its maximum. This signal was used as input parameter for the feedback. The dashed lines represent the feedback dead band. Following the injection and energy ramp, it is necessary to reduce the RF frequency in the beginning of the run up to −175 Hz indicating a lengthening of orbit in the order of 20 µm. After a runtime of about 90 minutes the reference orbit starts to shorten, therefore the RF frequency has to be detuned to higher values saturating at a value of 300 Hz. The total RF frequency detuning range of about 500 Hz corresponds to a relative change of orbit length of 10^{-6}.

Orbit lengthening in the beginning of the run occurs due to high thermal load imposed by the synchrotron radiation as well as thermal drifts of the electromagnets. The green graph in Fig. 3.18(b) corresponds to the temperature of the vacuum chamber of a selected dipole magnet. Within thermal time constants the maximum of the measured temperature coincides with the tipping point of the RF frequency feedback.

Arbitrariness of f_{rf0} The beam orbit in a storage ring is different from the design orbit. This is due to effects like magnet misalignments, hysteresis or undesired magnetization of elements in the vicinity of the beam path. Corrector magnets are used to minimize the rms deviation of the beam from the design orbit. By powering the corrector magnets not only the beam path is changed, but also its length. However, depending on the values of horizontal rms deviation and maximum dispersion, the RF "center" frequency is uncertain. At the MLS the horizontal orbit rms is about 0.2 mm whereas the maximum dispersion is about 2 m. Therefore, the reference energy E_0 is undefined by a factor of 10^{-4} propagating to f_{rf0} via Eq. 2.15 to:

$$\frac{\Delta C}{C_0} = \alpha(\delta)\delta \approx -\frac{\Delta f_{\mathrm{rf}}}{f_{\mathrm{rf}}} = \frac{1}{1+\frac{\Delta f_{\mathrm{rf}}}{f_{\mathrm{rf0}}}} - 1 \approx -\frac{\Delta f_{\mathrm{rf}}}{f_{\mathrm{rf0}}} + \mathcal{O}\left(\left(\frac{\Delta f_{\mathrm{rf}}}{f_{\mathrm{rf0}}}\right)^2\right). \tag{3.27}$$

3.10 Chromaticity Tool

When approaching small values of α_0, it is crucial to control the first order of the momentum compaction function $\alpha_1 = 0$ to avoid zero-crossings of $\alpha(\delta)$. The intention is to minimize the absolute value of α_1 to conserve momentum acceptance of the RF bucket (section 3.2). Usually, the measurement of α_1 by the means of a direct energy measurement is too time-consuming.

However, it is possible to obtain α_1 by investigating the chromatic shift of the longitudinal tune. For reasons of practical measurability, the longitudinal chromaticity shall be defined as:

$$\xi_s = \left.\frac{\mathrm{d}Q_s}{\mathrm{d}\delta}\right|_{\delta=0} = \left.\frac{\mathrm{d}Q_s}{\mathrm{d}\left(\frac{f_{\mathrm{rf0}}}{\alpha_0 f_{\mathrm{rf}}}\right)}\right|_{f_{\mathrm{rf}}=f_{\mathrm{rf0}}} \approx -\alpha_0 h \frac{\Delta f_s}{\Delta f_{\mathrm{rf}}}, \tag{3.28}$$

which is directly connected to α_1. Based on theory presented in section 4.3 it is possible to calculate α_1 from the longitudinal chromaticity solving equation:

$$\xi_s = \sqrt{\frac{heU_0 \cos(\varphi_s)}{2\pi E_0}} \frac{2\alpha_1 - {\alpha_0}^2}{2\sqrt{\alpha_0}} = \quad Q_s \Big|_{f_{\mathrm{rf}}=f_{\mathrm{rf0}}} \frac{2\alpha_1 - {\alpha_0}^2}{2\alpha_0}. \tag{3.29}$$

The measurement of the longitudinal chromaticity is done by evaluating the synchrotron oscillation frequency as a function of RF frequency detuning: $f_s(\Delta f_{\mathrm{rf}})$. This a much faster procedure to measure α_1, assuming knowledge of α_0. Therefore, in low-α operation or generally for $\alpha_0 \to 0$ the longitudinal chromaticity should be adjusted to zero to achieve $\alpha_1 = 0$.

In addition, control of the transverse chromaticities is necessary, e.g. to avoid chromatic resonance crossing or to fight the head-tail instability. Hence all three chromaticities have to be controlled for low-α operation. To correct the chromaticity, the MLS features three independent families of sextupole magnets. First order correction is done by solving a system of three coupled linear equations relating sextupole excitation currents and chromaticities. As chromaticity correction has to be done for every low-α state to be explored, a software tool based on MATLAB was developed for measurement as well as correction. Figure 3.19 shows the graphical user interface of a software implementation to automatically measure the chromaticities $\xi_{x,y,s}$. In addition, the 3-dimensional sextupole-chromaticity-response can be measured. Correction coefficients are calculated to be able to orthogonally adjust the chromaticity in the selected plane without affecting other planes. This tool is now implemented in the control system and its application part of standard maintenance procedures for low-α states at the MLS.

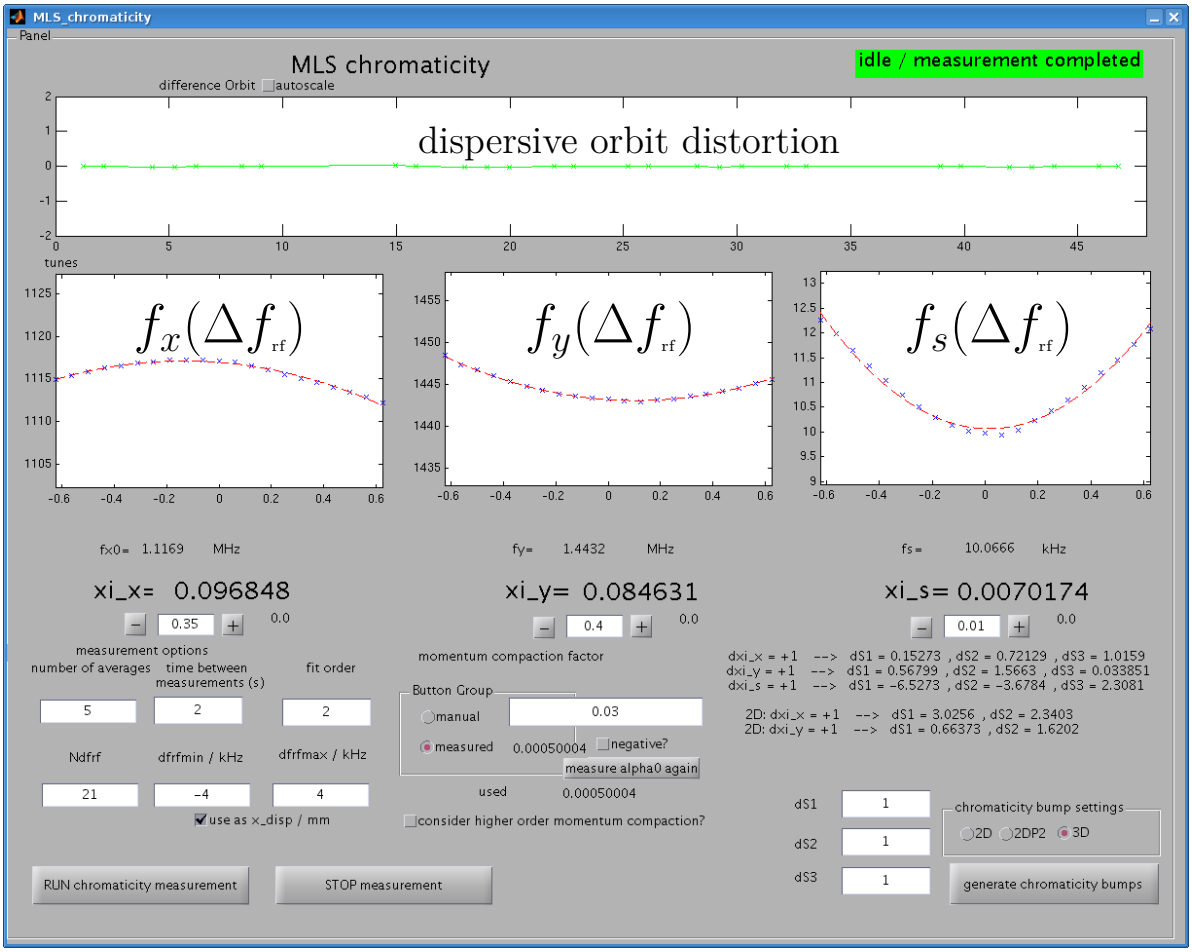

Figure 3.19: Screenshot of a software tool based on MATLAB to automatically determine and correct the first order chromaticity in all three planes.

4 Measurement Techniques for the Momentum Compaction Factor at the MLS

Regarding quasi-isochronous operation of storage rings, the momentum compaction factor cannot be assumed to be constant. While approaching α towards zero, it is crucial to conserve momentum acceptance. Therefore, knowledge and control of the momentum compaction factor including its higher orders is presumed. To measure the momentum dependence of $\alpha(\delta)$ there are different approaches. The most intuitive one is to use the means of a direct measurement of the electron energy such as Compton backscattering. Often such a direct measurement is not available, too time-consuming or insufficient in resolution. If that is the case, a model based approach has to be applied. This chapter will address different methods to determine $\alpha(\delta)$ applied at the MLS.

4.1 Beam Based Model Fitting

Predicting the momentum compaction factor is strongly dependent on the applied optical model especially for low-α operation. It is common at light sources to determine α based on MAD-X, *elegant* or other beam optics codes. The model quality can be refined by conducting measurements such as BPM-corrector response matrix measurements. The measurement results are then

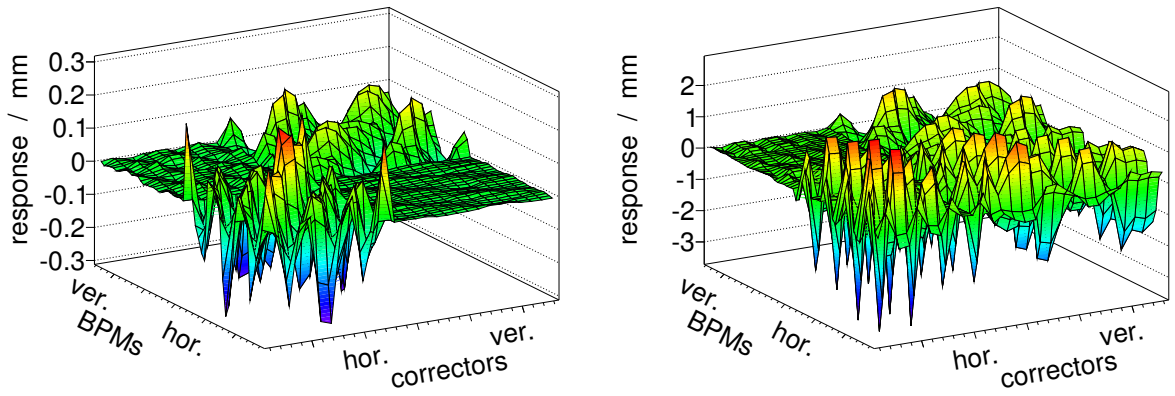

(a) standard user

(b) low-α

Figure 4.1: Orbit response matrix measurement performed in the MLS standard user mode (left) and in low-α user operation (right). Corrector kick strengths of approximately 0.03 mrad were applied in standard user operation and reduced for low-α operation.

fed back to the applied model by fitting selected model parameters. This technique was applied at the MLS using the tools Accelerator Toolbox, Matlab Channel Access, Matlab Middle Layer and LOCO [26, 62, 63]. The named tools are routinely used at the MLS to measure BPM-corrector response matrices as well as to evaluate the optical functions $\beta_{x,y}$ and D as depicted in Figs. 1.3, 3.1 and 3.7 [26].

Raw measurement results of orbit response matrix measurements performed at the MLS are shown in Fig. 4.1 for standard user operation (left) and low-α user operation (right). Kicks of approximately 0.03 mrad were applied by corrector magnets measuring the orbit response Δx and Δy compared to the undistorted orbit at 28 BPMs distributed around the storage ring. This process was conducted successively for all 12 horizontal and 16 vertical corrector magnets yielding the orbit response matrix.

By adjusting model parameters such as quadrupole magnet strength, BPM gain or corrector magnet kick strength, the model-predicted orbit response matrix is fitted to the measurement data. As a figure of merit for the model quality it is common to directly compare measured and model-predicted response matrices. Such an evaluation is shown in Fig. 4.2(a) for the standard

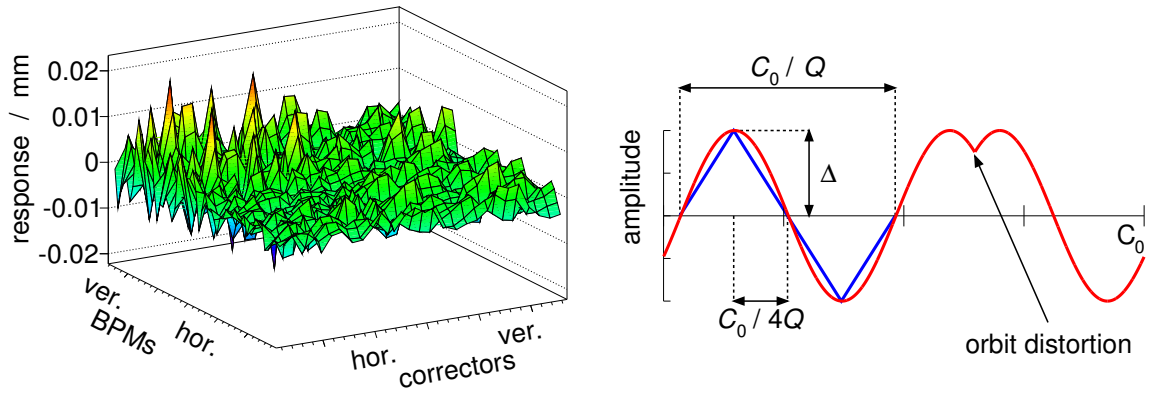

(a) standard user

(b) orbit lengthening due to orbit distortion

Figure 4.2: Left: Difference between measured and model based orbit response matrices for the standard user mode after fitting model parameters to measurement results. Right: Pythagorean approximation (blue) to estimate orbit lengthening (red) due to an orbit distortion.

user mode, whereas the difference between measured and predicted response matrix is plotted. The difference is more than one order of magnitude smaller compared to the absolute values and within the order of the BPM noise.

For standard user operation coupling between horizontal and vertical plane is minimal. This is indicated by the flat areas in Fig. 4.1(a), which relate horizontal correctors with vertical BPM response and vice versa. This is due to a minimized horizontal-vertical coupling of $\epsilon_y/\epsilon_x \approx 0.5\%$ achieved by application of skew quadrupoles [64].

Measurements of the orbit response matrix performed in standard user mode indicated sta-

bility with respect to small distortions in reference orbit, transverse coupling and RF center frequency. The data to model fitting result by LOCO for the standard user mode at the MLS yields a momentum compaction factor of:

$$\text{LOCO standard user:} \qquad \alpha_0 = 0.029 \pm 0.001, \tag{4.1}$$

which is within the expected range predicted by design models. Higher orders of the momentum compaction factor could not be determined within significance.

Similar measurements of the orbit response were performed at low momentum compaction. For low-α operation there is a strong coupling between horizontal and vertical plane as shown in Fig. 4.1(b). An applied vertical corrector kick introduces a vertical as well as a horizontal orbit response. In contrast, the reverse situation applying a horizontal corrector kick only generates negligible vertical orbit response, which is due to the responsible coupling mechanism. Introducing an orbit distortion generates a change of the orbit length resulting in a mismatch of particle revolution time to RF frequency. Therefore, particles will be forced on a dispersive orbit. As there is no vertical dispersion of significance, a change of orbit length will be compensated by the horizontal plane. To estimate the path lengthening by an orbit distortion, integration along the new closed orbit is necessary. However, to get an impression about the magnitude of the effect, a pythagorean approximation assuming a constant β-function yields:

$$l \approx \sqrt{\Delta^2 - \left(\frac{C}{4Q}\right)^2} - \frac{C}{4Q}, \tag{4.2}$$

$$\Delta C \approx 4Ql, \tag{4.3}$$

$$\frac{\Delta C}{C_0} \approx \sqrt{\left(\frac{4Q\Delta}{C_0}\right)^2 + 1} - 1, \tag{4.4}$$

whereas Q is the tune and Δ the displacement amplitude in the corresponding plane. The nature of the approximation is depicted in Fig. 4.2(b). Impact of the effect increases when α is small, as the dispersive displacement is amplified by the factor $1/\alpha$ as described by Eq. 3.26. Evaluation of Eq. 4.4 for an orbit distortion with an amplitude of $\Delta = 2$ mm, a tune of $Q = 3.18$, $D \approx 1.8$ m and $\alpha_0 = 1.3 \times 10^{-4}$ yields a dispersive displacement of $x_D \approx 2.0$ mm. Therefore, the applied corrector kick strengths were reduced by about a factor of five, to restrict the beam to the orbit range of BPM linearity. However, for measurements performed in low-α user operation at $\alpha_0 = 1.3 \times 10^{-4}$, reproducibility as well as fit quality showed poorer performance than in standard user mode. It was not possible to determine the momentum compaction factor based on the model within significance. Characterization of the low-α mode by orbit response measurements is the objective of ongoing beam studies at the MLS.

Even though model based characterization of the low-α user mode is not yet available, it is still of relevance for low-α operation. By determining the model based momentum compaction factor for larger values of α_0, it is possible to apply the scaling of the synchrotron oscillation frequency $f_s \propto \sqrt{\alpha_0}$ as given in Eq. 2.33. Therefore, a precise value for α_0 in a low-α state can be obtained by measuring f_s.

The effect of orbit lengthening introduced by corrector kicks, limits the classical way of mea-

suring of the orbit response matrices for $\alpha \to 0$. In this case, the measured orbit distortions will be completely dominated by a dispersive contribution for smallest corrector kick strengths. In addition, the dispersive displacement may be dominated by higher order terms of the dispersion function in δ. However, an approach could be to slowly introduce the orbit distortion by a corrector magnet while simultaneously adjusting the RF frequency to compensate the change in path length.

4.2 Direct Measurement using Compton Backscattering

The most common technique to measure the particle energy in electron or positron storage rings is resonant spin depolarization [65–67]. This method is applicable for electron storage rings due to the Sokolov–Ternov effect leading to a self-polarization driven by the emission of synchrotron radiation. Resonant spin depolarization is a very accurate method to measure the electron energy yielding a relative uncertainty of better than 10^{-4}. However, this method is restricted to electron energies in the GeV range, as the radiative polarization time scales with γ^{-2} for constant bending field strength exceeding electron beam lifetime and practicability for low energy machines, which is the case for the MLS.

An alternative approach to measure the energy of the electrons in a synchrotron light source directly is to utilize the effect of Compton scattering [68]. Although the Compton backscattering method is not applicable on all sources, it is a well understood technique for low energy machines [69]. Laser photons with a well known initial photon energy are scattered in a head-on collision with stored electrons as depicted in Fig. 4.3(a). The spectrum of the backscattered photons is

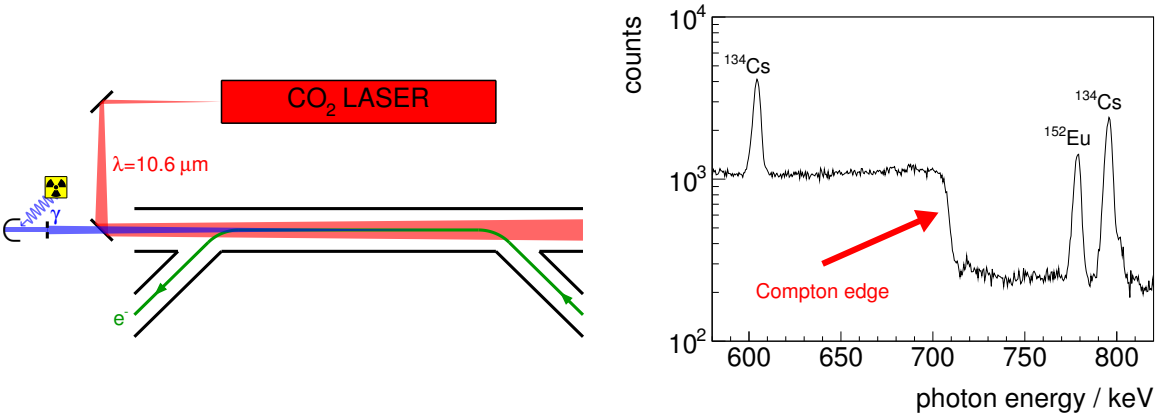

(a) measurement setup

(b) example measurement

Figure 4.3: Measurement of the electron energy by the Compton backscattering method. Sketch of the experimental setup (a). Example measurement: spectrum of backscattered photons at 629 MeV (b). Sharp peaks correspond to radioactive isotopes used for the energy calibration of the detector.

then characterized by a sharp edge at a certain photon energy. The "Compton edge" is formed by

photons that encountered the maximum energy transfer from their scattering partner - electrons from the beam. This is the case for head-on collision. Given the photon energy of the Compton edge, the electron energy can be calculated by solving equation:

$$E^{\max}_{\text{photon, final}} = \frac{4\gamma^2 E_{\text{photon, initial}}}{1 + 4\gamma E_{\text{photon, initial}} / (m_e c^2)}, \tag{4.5}$$

whereas γ denotes the Lorentz-factor of the stored electrons [69], $E_{\text{photon, initial}}$ the initial photon energy and $E^{\max}_{\text{photon, final}}$ the photon energy of 180° backscattered photons forming the Compton edge.

Figure 4.3(b) shows an example measurement of the electron energy by Compton backscattering performed at the MLS at $(628.9 \pm 0.6)\,\text{MeV}$. The measurement was conducted using the insertion device straight to overlap photon beam and electron beam. A carbon dioxide laser was used as a source of photons with an energy of $E_{\text{photon, initial}} = 0.117\,\text{eV}$ yielding backscattered photons of up to $E^{\max}_{\text{photon, final}} \approx 709\,\text{keV}$. The value of $E^{\max}_{\text{photon, final}}$ was obtained by fitting a step-like function folded with a Gaussian to the spectrum, whereas the width of the Gaussian is given by the energy spread of the beam as well as the energy resolution of the detector. The spectrum was taken over a detector live time of 120 s counting a total number of 1.8×10^6 photons, whereas a fraction of about 61% account to backscattered laser photons. The remaining photons are contributed by natural background radiation, Bremsstrahlung as well as decaying radioactive isotopes used for the energy calibration of the energy-dispersive detector.

The relative uncertainty of the Compton backscattering method to measure the electron energy at the MLS is approximately 10^{-4}, which is in the order of the natural energy spread of the beam. It is dominated by the uncertainty introduced by the energy calibration of the detector as well as its resolution. Further contributions are accumulated statics as well as laser beam to electron beam misalignment, which are negligible for the experiments conducted at the MLS.

By changing the RF frequency, particles can be forced on dispersive trajectories to match the right revolution frequency as given in Eq. 3.27. Due to symmetry properties of beam optics, the dispersion in the insertion device straight is constant ($D' = 0$) for all investigated beam optics, as is exemplarily visualized in Fig. 3.1. Therefore, the collision angle of photon and electron beams is preserved for dispersive orbits. From the storage ring side, RF frequency detuning Δf_{rf} is limited by the dispersive displacement of the electron beam in the horizontal plane according to Eq. 2.5. Laser to electron beam alignment can be kept constant during the measurement, as the laser beam width is large compared to the dispersive displacement of the electron beam. By measuring the electron energy in dependence of the RF-detuning it is possible to map the momentum dependence of the momentum compaction factor $\alpha(\delta)$ by evaluation of Eqs. 2.13 or 3.27.

Figure 4.4 shows two selected sets of Compton backscattering measurements performed at the MLS yielding the relation $\Delta f_{\text{rf}}(\delta)$, which is suitable to derive $\alpha\,(\delta)$. A measurement in the standard user mode is shown in Fig. 4.4(a), whereas the curvature of the momentum compaction function is negligible. In contrast, Fig. 4.4(b) corresponds to a low-α setting, whereas a strong α_2 was introduced by the octupole magnets. Data was obtained by successively measuring the electron beam energy for different values of RF frequency detuning $E(\Delta f_{\text{rf}})$. For evaluation of the data an expanded power series in the form of Eq. 2.10 was used, to describe the momentum

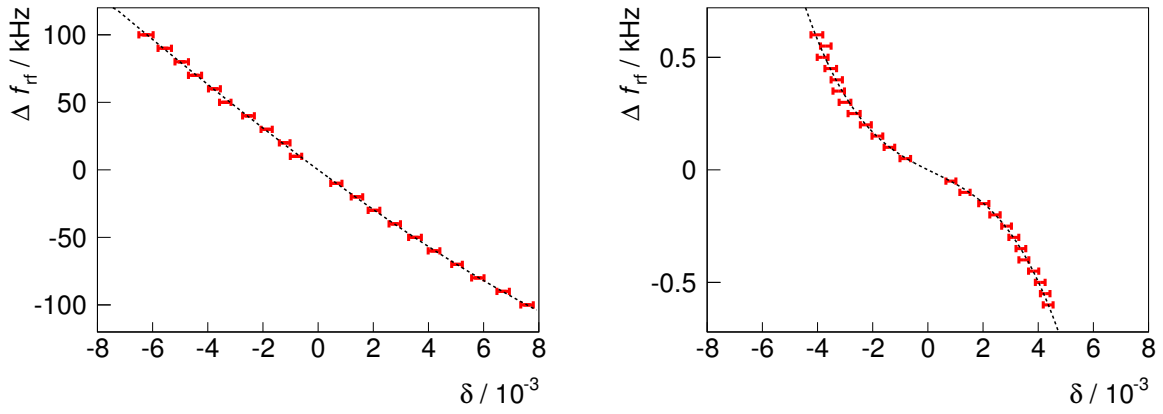

(a) standard user, $\alpha(\delta) \approx \alpha_0$

(b) low-α with large α_2, $\alpha(\delta) \approx \alpha_0 + \alpha_2\delta^2$

Figure 4.4: Measurement of the momentum dependent revolution time at the MLS in standard user operation (left) as well as low-α operation with strongly excited octupole (right). Momentum deviation was determined by measuring the energy of Compton-backscattered laser photons for multiple RF frequencies. It should be noted, that the RF frequency scales of both figures differ by a factor of 200.

compaction function in the three leading orders. Equation 3.27 then yields:

$$\frac{1}{1+\frac{\Delta f_{\mathrm{rf}}}{f_{\mathrm{rf0}}}} - 1 = \alpha\left(\delta\right)\delta \approx \sum_{i=0}^{2} \alpha_i \delta^{i+1}. \tag{4.6}$$

Using Eq. 4.6, analysis of the Compton backscattering data taken in standard user mode yields a momentum dependent momentum compaction factor:

$$\alpha(\delta)_{\text{standard user}} = (0.0302 \pm 0.0009) + (-0.38 \pm 0.20)\,\delta + (-9 \pm 35)\,\delta^2. \tag{4.7}$$

Higher orders of $\alpha\left(\delta\right)$ in standard user mode were not measurable within significance. The value of α_0 is well within the expected range of model predictions obtained in section 4.1.

For low-α user operation the analog evaluation of Compton backscattering data yields a momentum compaction factor of:

$$\alpha(\delta)_{\text{low-}\alpha} = (1.3 \pm 0.1) \times 10^{-4} + (0.005 \pm 0.001)\,\delta + (8.5 \pm 1.3)\,\delta^2, \tag{4.8}$$

whereas α_0 was drastically decreased by a factor of:

$$\frac{\alpha_{0_{\text{standard user}}}}{\alpha_{0_{\text{low-}\alpha}}} \approx 232 \pm 25. \tag{4.9}$$

The ratio of α_0 given in Eq. 4.9 is in agreement with the ratio of measured synchrotron oscillation

frequencies:

$$\frac{f^2_{s_{\text{standard user}}}}{f^2_{s_{\text{low-}\alpha}}} \approx 243 \pm 5, \tag{4.10}$$

whereas the measurement was performed at $E_0 = 629\,\text{MeV}$ and $U_0 = 250\,\text{kV}$ using a ring current of $I \approx 1\,\text{mA}$.

In standard user mode, the value of α_1 obtained in Eq. 4.7 is the result of the chromaticity correction in the transverse planes $\xi_{x,y} \approx 1$. This is in agreement with measurements of the longitudinal chromaticity $\xi_s = -0.16 \pm 0.01$ (see Eq. 3.29) as well as MAD-X model predictions. In addition, to investigate the impact of the octupole magnet for low-α operation, multiple measurement sets for different excitation currents of the octupole magnet were performed.

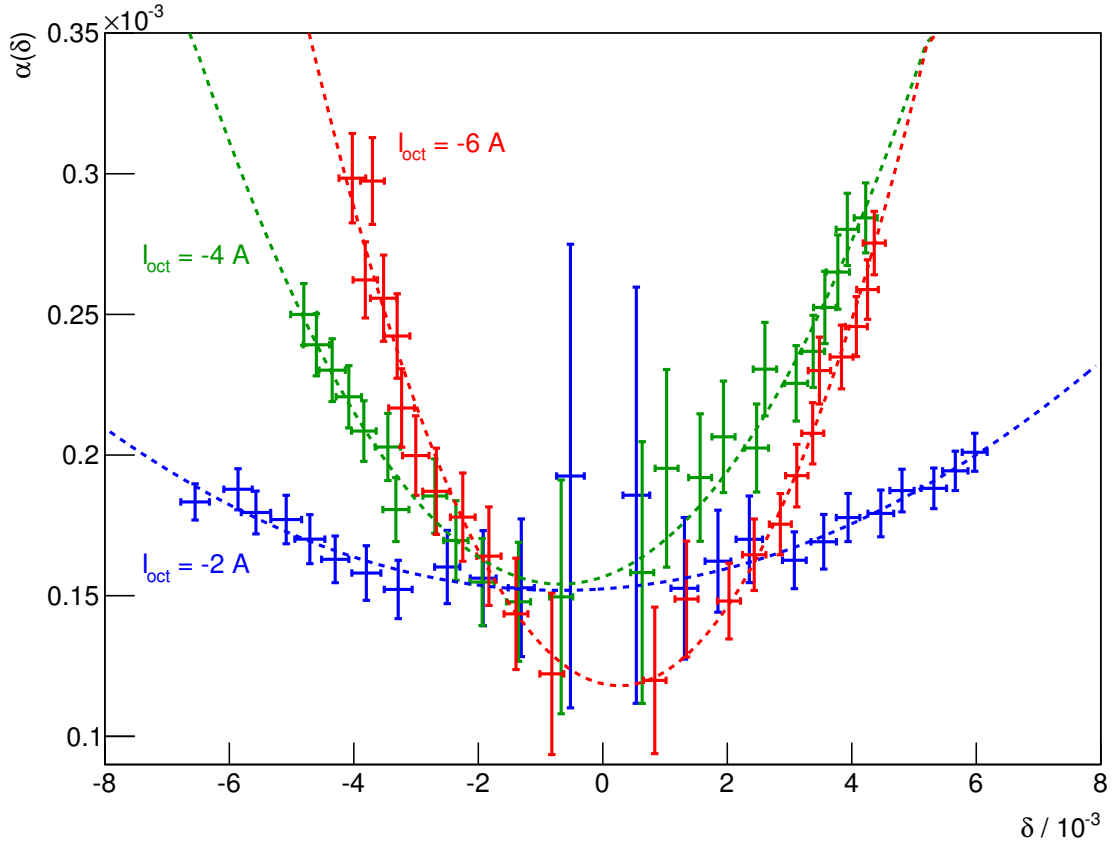

Figure 4.5: Compton-backscattering based measurement of the momentum compaction factor in the low-α user mode of the MLS for different excitation currents of the octupole magnets.

Selected measurement sets are given in Fig. 4.5 and Tab. 4.1. The large uncertainties of the measurement depicted in Fig. 4.5 for small momentum deviations are introduced by the small

I_{octupole} / A	α_0 / 10^{-4}	α_1 / 10^{-3}	α_2
-1 A	0.9 ± 0.2	0.7 ± 1.8	0.7 ± 1.1
-2 A	1.52 ± 0.05	1.5 ± 0.4	1.1 ± 0.2
-4 A	1.57 ± 0.08	7.6 ± 1.0	5.6 ± 0.6
-6 A	1.19 ± 0.08	-5.0 ± 1.3	9.3 ± 0.7

Table 4.1: Compton backscattering measurement results for manipulation of α_2 by octupole magnet excitation for the MLS low-α user operation.

value of α_0. A constant step width of $\Delta f_{\text{rf}} = 50$ Hz was used to map the momentum compaction function. For the first steps the momentum deviation being the difference of two slightly different large values yields a large relative uncertainty.

The impact of the octupole excitation current on the term α_2 shows an approximately linear dependence:

$$\alpha_2 \left(I_{\text{octupole}}\right)_{629\,\text{MeV low-}\alpha} = (-2.11 \pm 0.17)\,\frac{1}{\text{A}} I_{\text{octupole}} + (-3.1 \pm 0.4)\,, \tag{4.11}$$

whereas the value of $\alpha_2 \left(I_{\text{octupole}} = 0\right) = -3.1 \pm 0.4$ corresponds to the "natural" curvature of the momentum compaction function in MLS low-α user optics when not applying the octupole correction. The maximum applicable octupole excitation current is 8 A. The measured curvature agrees well with a model-based value of $\alpha_2 \left(I_{\text{octupole}} = 0\right)_{\text{model}} \approx -3.0$ predicted by MAD-X. Applying Eq. 3.11 yields an estimated reduction of momentum acceptance to approximately 0.6% for operation without octupoles, which may be additionally reduced by the contribution of a non vanishing α_1.

4.3 Higher Order Measurement based on Local Momentum Compaction

Another approach to investigate the momentum compaction factor was proposed in [70] based on the idea to evaluate the response function $f_s(f_{\text{rf}})$. A similar approach is given in [71]. However, the method is restricted to yield results only for the higher orders of the momentum compaction factor. On the contrary, it relies on the knowledge of the zeroth order term α_0. The advantage of the presented method is easy accessibility as well as fast and precise measurability of the involved quantities. Therefore a detailed examination is conducted.

Particles forced on a dispersive closed orbit by detuning the RF frequency will perform longitudinal oscillations around this orbit. In the limit of small amplitude oscillations around the dispersive closed orbit, it is possible to scan the nonlinear potential given by $\alpha(\delta)$ by probing it through "local" harmonic oscillators. Therefore, it is relevant to distinguish between the momentum compaction factor α as defined in Eq. 2.8 and the local momentum compaction factor

α_p:

$$\alpha = \frac{\Delta C}{C_0} \Big/ \frac{\Delta p}{p_0}, \qquad \alpha_p = \frac{\mathrm{d}C}{C(p)} \Big/ \frac{\mathrm{d}p}{p}. \tag{4.12}$$

The momentum compaction function $\alpha(\delta)$ describes the change of orbit length with respect to the reference particle (p_0, f_{rf0}), whereas α_p describes the differential change of the orbit length around a new reference trajectory defined by (p, f_{rf}). Using the definition of $\alpha(\delta)$ given in Eq. 2.8 it is possible to derive the relation $\alpha_p(\delta, \alpha(\delta))$:

$$C = C_0 \left(1 + \alpha(\delta)\delta\right), \tag{4.13}$$

$$\alpha_p\left(\delta\right) = \frac{\mathrm{d}C}{\mathrm{d}p}\frac{p}{C} = \frac{\mathrm{d}C}{\mathrm{d}\delta}\frac{\mathrm{d}\delta}{\mathrm{d}p}\frac{p}{C}, \tag{4.14}$$

with the result of:

$$\alpha_p\left(\delta\right) = \frac{1+\delta}{1+\alpha\left(\delta\right)\delta}\frac{\mathrm{d}\left(\alpha\left(\delta\right)\delta\right)}{\mathrm{d}\delta} = \frac{1+\delta}{1+\sum_{i=0}^{\infty}\alpha_i\delta^{i+1}}\sum_{i=0}^{\infty}\left(i+1\right)\alpha_i\delta^i, \tag{4.15}$$

whereas the right part of Eq. 4.15 already uses the series expansion of the momentum compaction function. Figure 4.6(a) shows the comparison of momentum compaction $\alpha(\delta)$ (blue) and local

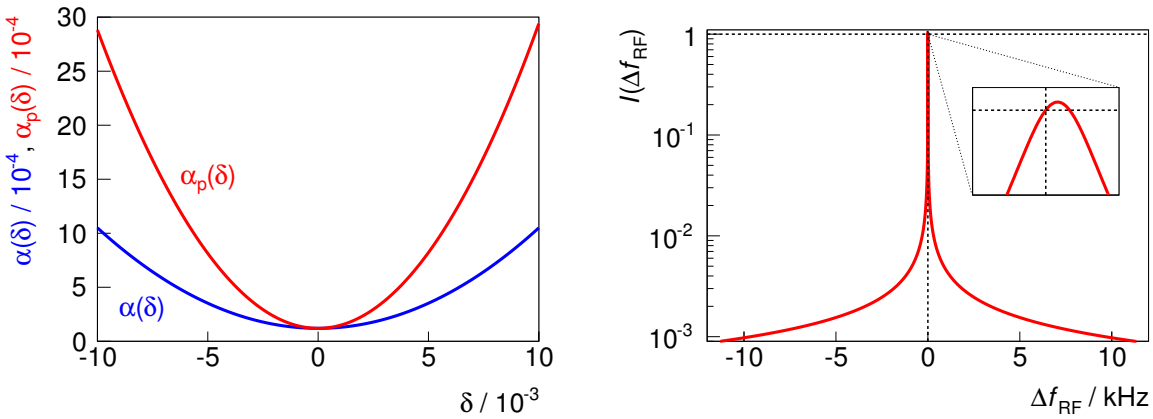

(a) $\alpha(\delta) = 1.2 \times 10^{-4} + 9.3\delta^2$

(b) $\alpha(\delta) = 10^{-5} + 0.01\delta + 100\delta^2$

Figure 4.6: Left: Quantitative comparison of calculated values for momentum compaction $\alpha(\delta)$ shown in blue and local momentum compaction $\alpha_p(\delta)$ shown in red. Right: Evaluation of the integrand $I(\Delta f_{\mathrm{rf}})$ given in Eq. 4.20 (right).

momentum compaction $\alpha_p(\delta)$ (red) for a momentum compaction function of $\alpha(\delta) = 1.2 \times 10^{-4} + 9.3\delta^2$.

In the limit of $f_{\mathrm{rf}} \to f_{\mathrm{rf0}}$ respectively $p \to p_0$ both quantities correspond to each other:

$$\lim_{p \to p_0} \alpha(\delta) = \alpha_0 = \lim_{p \to p_0} \alpha_p. \tag{4.16}$$

From here, quantities marked by the index p correspond to qualities of a particle stored on a dispersive closed orbit featuring the momentum p. For a particle oscillating with an infinitesimal amplitude around its dispersive reference orbit, the synchrotron oscillation frequency $f_{s,p}$ corresponding to Eq. 2.33 is then given by:

$${f_{s,p}}^2 = -\frac{f_{\mathrm{rf,p}}^2 \alpha_p e U_0 \cos(\varphi_{s,p})}{2\pi \beta_p p c h}. \tag{4.17}$$

As the effective RF voltage is commonly not well known, it is practical to regard the ratio $f_{s,p}/f_{s,p_0}$:

$$\frac{f_{s,p}^2}{f_{s,p_0}^2} = \frac{f_{\mathrm{rf,p}}^2 \alpha_p \cos(\varphi_{s,p}) \beta_0 p_0}{f_{\mathrm{rf0}}^2 \alpha_0 \cos(\varphi_{s,p_0}) \beta_p p} \approx \frac{f_{\mathrm{rf,p}}^2}{f_{\mathrm{rf0}}^2} \frac{p_0}{p} \frac{\alpha_p}{\alpha_0}, \tag{4.18}$$

whereas the approximation $\beta_0/\beta_p \approx 1$ was used as particles are highly relativistic. In addition, the term $\cos(\varphi_{s,p}) / \cos(\varphi_{s,p_0}) \approx 1$ was neglected, as usually the synchronous phase is in the order of less than a few degrees and its dispersive change is negligible.

Substituting Eq. 4.12 in Eq. 4.18 yields:

$$\frac{\mathrm{d}p}{p_0} = \frac{f_{s,p_0}^2}{f_{s,p}^2} \frac{f_{\mathrm{rf,p}}^2}{f_{\mathrm{rf0}}^2} \frac{1}{\alpha_0} \frac{\mathrm{d}C}{C_p}. \tag{4.19}$$

Inserting $\frac{\mathrm{d}C}{C_p} = -\frac{\mathrm{d}f_{\mathrm{rf,p}}}{f_{\mathrm{rf,p}}}$, $\Delta f_{\mathrm{rf,p}} = f_{\mathrm{rf,p}} - f_{\mathrm{rf0}}$ and integrating on both sides from p_0 to p yields:

$$\delta = -\frac{1}{\alpha_0 f_{\mathrm{rf0}}} \int_0^{\Delta f_{\mathrm{rf,p}}} \underbrace{\frac{f_{s,p_0}^2}{f_{s,p}^2} \left(1 + \frac{\Delta f_{\mathrm{rf}}}{f_{\mathrm{rf0}}}\right)}_{I(\Delta f_{\mathrm{rf}})} \mathrm{d}\Delta f_{\mathrm{rf,p}}. \tag{4.20}$$

Therefore, if the relation $f_s = f_s(\Delta f_{\mathrm{rf}})$ is known sufficiently well, it is possible to calculate the momentum deviation $\delta(\Delta f_{\mathrm{rf}})$. However, for a momentum compaction function dominated by the first few orders, the integrand $I(\Delta f_{\mathrm{rf}})$ in Eq. 4.20 shows a sharp peak around $\Delta f_{\mathrm{rf}} = 0$ as show in Fig. 4.6(b), which is a pitfall for integration.

The involved quantities needed to evaluate Eq. 4.20 are easy to measure with small uncertainties, with the exception of α_0. Therefore, this method yields a fast and accurate measurement of high orders of the momentum compaction factor. To check applicability of the proposed method independently from the analytical approach, a forward simulation was performed. The main driving questions to be investigated are:

- What is the needed density of sampling points for $f_s(\Delta f_{\mathrm{rf}})$?
- What is the impact of non-vanishing oscillation amplitudes?

Results from Compton-backscattering measurements (see Tab. 4.1) were used as input parameters as well as an overstated momentum compaction function $\alpha(\delta) = 10^{-5} + 0.01\delta + 100\delta^2$ to ensure that the investigated regime covers the MLS tuning range.

Tracking Algorithm

A tracking code was set up to obtain synchrotron oscillation frequencies for particles stored on dispersively displaced closed orbits. Single particle tracking restricted to the longitudinal plane was done within highly relativistic approximation ($1/\gamma^2 \ll \alpha$). Quantum excitation as well as radiation damping was neglected. The new reference momentum p will be treated in the form of momentum deviation $\delta = p/p_0 - 1$.

A rough sketch of the algorithm look like:

- input new reference electron energy,
- regard the synchronous phase,
- calculate the length of the new, dispersive reference orbit respectively f_{rev}, f_{rf} and Δf_{rf} for a given $\alpha(\delta)$ and f_{rf0},

$$f_{\mathrm{rf}} = \frac{f_{\mathrm{rf0}}}{1 + \alpha(\delta)\,\delta}, \tag{4.21}$$

$$\Delta f_{\mathrm{rf}} = -\frac{f_{\mathrm{rf0}}}{1 + \frac{1}{\alpha(\delta)\delta}}, \tag{4.22}$$

- track (φ_i, δ_i) for given initial values over N turns using equations:

$$\varphi_{i+1} = \varphi_i + 2\pi h \left(\frac{C(\delta_i)}{C_{\text{new ref orbit}}} - 1 \right), \tag{4.23}$$

$$\delta_{i+1} = \delta_i + \frac{eU_0}{E\beta^2} \left(\sin(\varphi_{i+1}) - \sin(\varphi_s) \right), \tag{4.24}$$

- obtain synchrotron oscillation frequency from track.

Here, δ_i describes the momentum deviation from the new reference energy $\delta_i = \Delta p/p \neq \Delta p/p_0$ in the i-th turn. The momentum dependent orbit length is calculated turnwise, to be able to investigate impact of oscillation amplitudes scanning a locally not constant momentum compaction function.

The impact of electron energy dependent energy loss was negligible for all simulations within the regime relevant for measurements.

Tracking Results

Figure 4.7(a) shows the comparison between tracked synchrotron oscillation frequency f_s and an estimate based on local momentum compaction using a momentum compaction function of

$\alpha(\delta) = 10^{-5} + 0.01\delta + 100\delta^2$ as input parameter. Tracking was performed with a small longitudinal oscillation amplitude of $\delta_{\text{amp}} \approx 10^{-8}$ to avoid distortion of locally harmonic oscillations by higher orders of $\alpha(\delta)$. The estimation $f_{s_{\text{calc}}} = f_s(\alpha_p)$ was obtained by evaluating Eqs. 4.15 and 4.17. Data obtained by tracking for $f_s(\Delta f_{\text{rf}})$ shows agreement between tracking and analytical calculation within the regime investigated by measurements at the MLS. The scattering for small momentum deviations is numerical noise due to limited frequency resolution determined by the number of tracked turns. There is a systematic deviation that can be identified for larger δ, which is in the order of sub-permille and will be neglected.

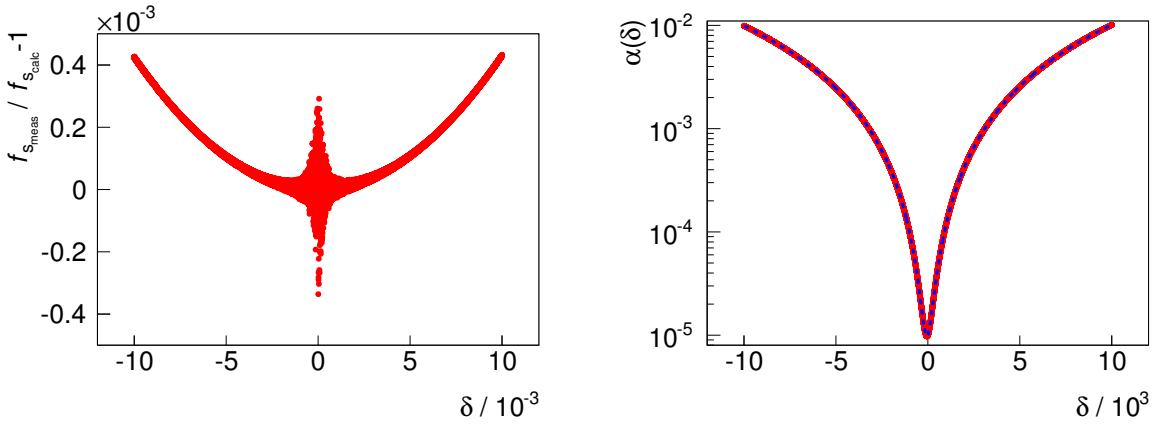

(a) f_s: tracking vs. calculation

(b) method consistency check

Figure 4.7: Tracking feasibility test: Comparison of analytically calculated and tracked synchrotron oscillation frequency for particles on dispersive closed orbits (left). Method self-consistency check (right): Comparison of momentum compaction functions used as input parameter (black) and yielded result (blue).

However, the inversion of $f_s(\delta)$ to $\delta(f_s)$ yields data analysis pitfalls. When evaluating Eq. 4.20 the peak-like shape of the integrand has to be treated correctly by the integration procedure. Naive integration by using the trapezoidal rule and a dense grid of sampling points in δ was used as a first brute force approach with a resolution of $\Delta\delta = 2 \times 10^{-5}$. A comparison of input and output momentum compaction function is given in Fig. 4.7(b), with to following fit results:

$$\alpha(\delta) = 10^{-5} + (9.962 \pm 0.007) \times 10^{-3}\delta + (99.89 \pm 0.01)\,\delta^2. \tag{4.25}$$

Deviation of the fit result from input values for $\alpha(\delta)$ outside the error margins are due to the limited number of sampling points. A comparison of $\alpha_{i_{\text{in}}}$ and $\alpha_{i_{\text{out}}}$ in dependence of the density of sampling points $\Delta\delta$ is given in Fig. 4.8(a). Blue data points correspond to $\alpha_{2_{\text{out}}}/\alpha_{2_{\text{in}}}$, whereas red data points correspond to $\alpha_{1_{\text{out}}}/\alpha_{1_{\text{in}}}$. A dense grid of sampling points with a spacing in the order of $\Delta\delta = 10^{-4}$ seems to be necessary to account for the nonlinearity of the momentum compaction function. Sampling point densities of this magnitude are not applicable for practical measurements. Integration techniques such as Newton-Cotes integration have not shown significant improvement, which is due to the unusual shape of the integrand.

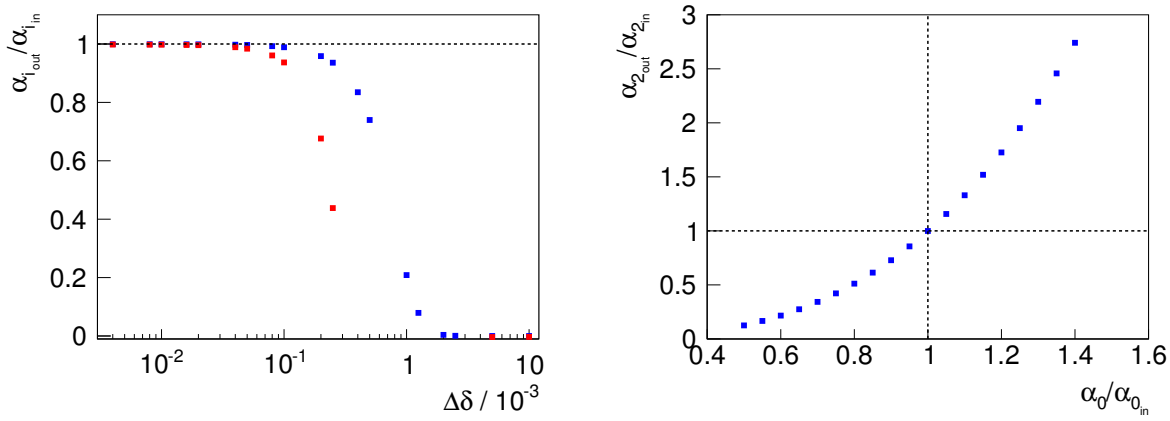

(a) impact of sampling point density

(b) impact of α_0

Figure 4.8: Left: Required density of sampling points to determine α_1 (red) and α_2 (blue) using naive integration. A comparison of input and output values is shown (see text). Right: Impact of α_0-uncertainty (right) on the retrieved value of α_2.

Alternatively, the integrand $I(\Delta f_{\mathrm{rf}})$ can be measured with a rough sampling density of $\Delta\delta = 10^{-3}$. A polynomial fit can be performed separately for every branch, followed by naive integration yielding acceptable results for δ_p.

The occurrence of α_0 in Eq. 4.20 introduces a strong sensitivity to the applied value of α_0. The relative error of $\alpha_{2_{\mathrm{out}}}$ increases with the third order of the relative error of $\alpha_{0_{\mathrm{in}}}$ as shown in Fig. 4.8(b), which can be deduced from Eqs. 3.27 and 4.20. Therefore a good knowledge of α_0 is mandatory for the application of this method to determine α_2.

An additional effect in the real machine is the impact of a locally non-constant momentum compaction. When the beam is forced on a dispersive trajectory, the fixed point of the RF bucket in δ will shift to off-reference values. However, to be able to measure the synchrotron oscillation frequency around this fixed point, the beam has to be excited to exert small coherent oscillations. Furthermore, the beam will always be excited longitudinally by a non-ideal RF cavity voltage. The introduced oscillation amplitude in δ may lead to a distortion of locally harmonic oscillation for a strongly non-linear $\alpha(\delta)$. To investigate the impact of oscillation amplitudes, additional tracking simulations were performed as show in Fig. 4.9. Therefore, the measurement results obtained by Compton backscattering, as described in section 4.2, were used as $\alpha(\delta)$ input parameters for the tracking algorithm. Particles were started at the synchronous phase φ_s with amplitudes of $\delta_{\mathrm{amp}} = 0\delta_0$ (black), $\delta_{\mathrm{amp}} = 1\delta_0$ (red), $\delta_{\mathrm{amp}} = 2\delta_0$ (blue), $\delta_{\mathrm{amp}} = 3\delta_0$ (green), $\delta_{\mathrm{amp}} = 5\delta_0$ (magenta) and $\delta_{\mathrm{amp}} = 10\delta_0$ (yellow). Here $\delta_0 \approx 4.4 \times 10^{-4}$ corresponds to the natural rms energy spread of the beam at 629 MeV. Fourier analysis of the tracking data yields the synchrotron oscillation frequency f_s. For large amplitude oscillations there is a clear impact of higher order momentum compaction on f_s.

Simultaneously to performing the Compton backscattering measurements described in section 4.2, the synchrotron oscillation frequency was measured as shown by red error bars in

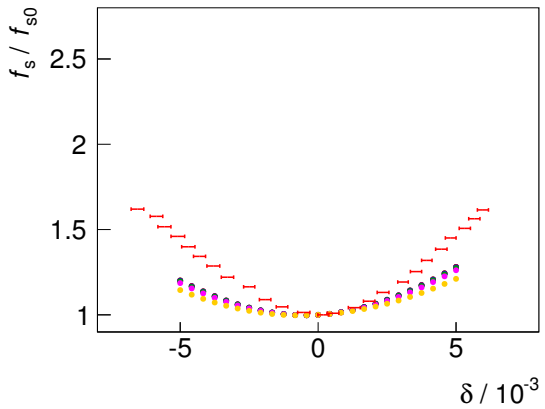

(a) $\alpha(\delta) = 1.52 \times 10^{-4} + 1.5 \times 10^{-3}\delta + 1.1\delta^2$

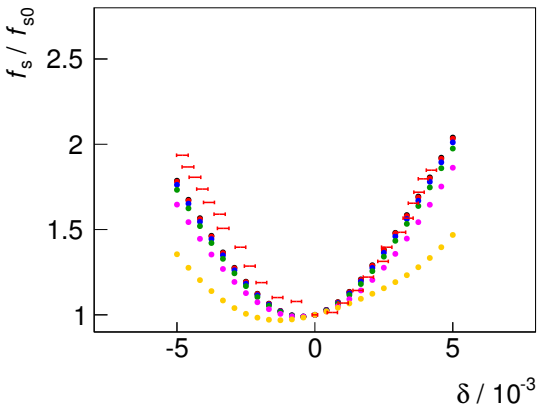

(b) $\alpha(\delta) = 1.57 \times 10^{-4} + 7.6 \times 10^{-3}\delta + 5.6\delta^2$

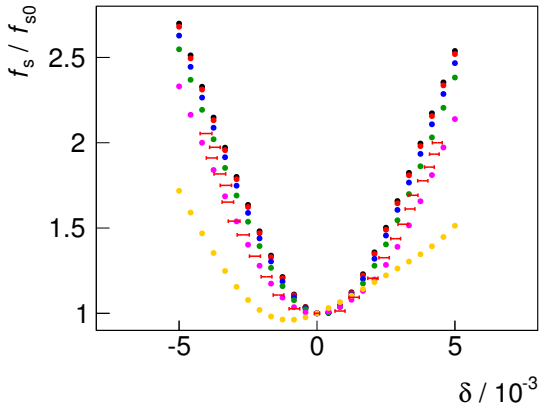

(c) $\alpha(\delta) = 1.19 \times 10^{-4} - 5 \times 10^{-3}\delta + 9.3\delta^2$

Figure 4.9: Longitudinal tune shift for dispersive closed orbits: CBS measurement results (red error bars) and oscillation amplitude resolved tracking results (colored dots).

Fig. 4.9. However, the measurement results for f_s are inconsistent with the predictions by the tracking code especially for Fig. 4.9(a). Therefore the yielded values for higher orders of the momentum compaction factor do not agree.

At the time of writing this work, the mismatch of this method to determine higher orders of the momentum compaction factor with the results obtained by the well established Compton backscattering method is still under study. However, the method has proven to yield precise, self-consistent results comparing particle tracking and analytical calculation.

5 α-Buckets

The momentum dependence of $\alpha(\delta)$ may lead to a modified longitudinal phase space enabling new operation possibilities. In particular, momentum compaction functions possessing zero-crossings form a subgroup of special interest for this work. Solutions of the equation $\alpha(\delta) = 0$ introduce new fixed points to the longitudinal phase space, which form the so-called "α-buckets" depicted in Fig. 5.1 (cf. Fig. 2.4(b)). Early references of this bucket type are given in [72, 73]. Simultaneously populated α-buckets were first observed at the National Synchrotron Light Source (NSLS) [74] and later at DIAMOND [75] the MLS [23] and SOLEIL [76]. This chapter will deduce basic characteristics of α-buckets, present experimental results obtained at the MLS and give a brief overview of possible applications for user operation at electron storage rings.

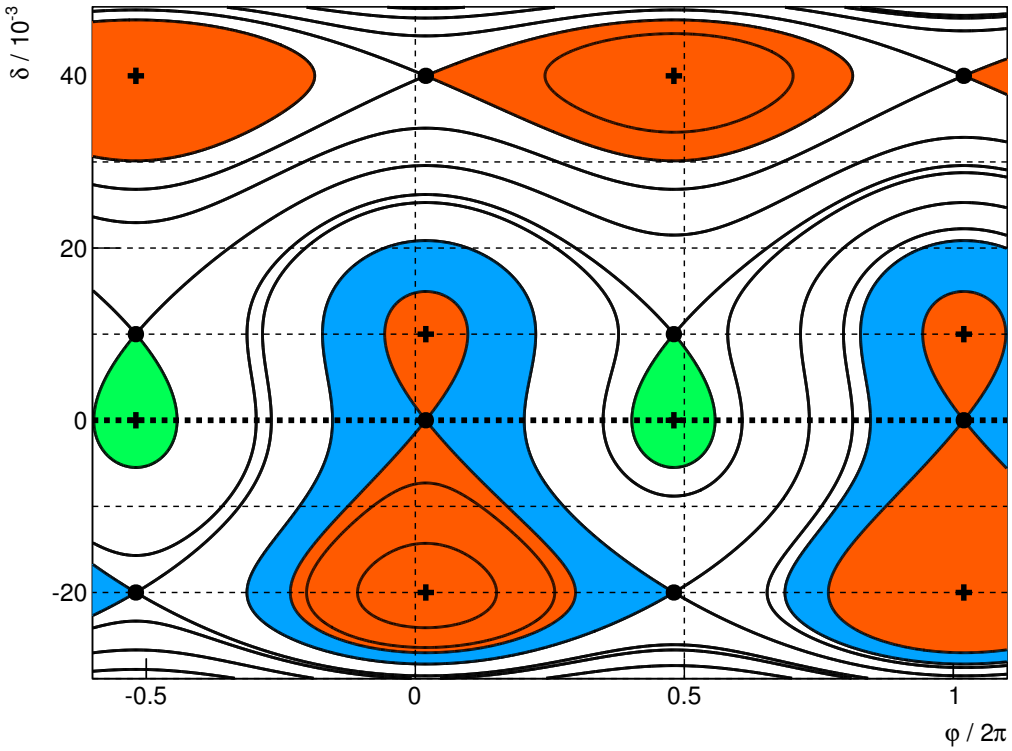

Figure 5.1: Example of a longitudinal phase space featuring α-buckets (red & blue areas). Stable (crosses) and unstable (dots) fixed points are given, whereas colors indicate areas of closed trajectories, i.e. particles are bound to the corresponding fixed points.

5.1 α-Bucket Definition

Buckets in nonlinear longitudinal phase space may be of different nature, however, buckets are located around fixed points defined by Eqs. 2.40 and 2.41. From Eq. 2.39 follows:

$$\alpha(\delta_{\mathrm{FP}})\delta_{\mathrm{FP}} = 0, \tag{5.1}$$

which is solved by either of the following cases:

$$\delta_{\mathrm{FP}} = 0 \quad \longrightarrow \quad \text{RF-bucket}, \tag{5.2}$$

$$\alpha(\delta_{\mathrm{FP}}) = 0 \quad \longrightarrow \quad \alpha\text{-bucket}. \tag{5.3}$$

Two generally different bucket types exist that shall be referenced throughout this work by "RF-bucket" and "α-bucket".

The RF-bucket, as discussed in section 2.7, is generated by the solution of Eq. 5.1 through $\delta = 0$ for arbitrary $\alpha(\delta)$. Therefore, particles stored in an RF-bucket perform oscillations around a fixed point at $\delta_{\mathrm{FP}} = 0$, where the zero-crossing of δ yields phase focusing as given in Eq. 2.28. The RF-bucket repeats in phase every 2π. However, multiple RF-buckets with different properties are possible for non-trivial RF voltages e.g. [13].

Alpha-buckets shall be defined as buckets generated by a zero-crossing of the momentum compaction function. Equation 5.1 is then solved through $\alpha(\delta_{\mathrm{FP}}) = 0$ independently of δ. Therefore, particles can be stably stored at non-zero momentum deviation.

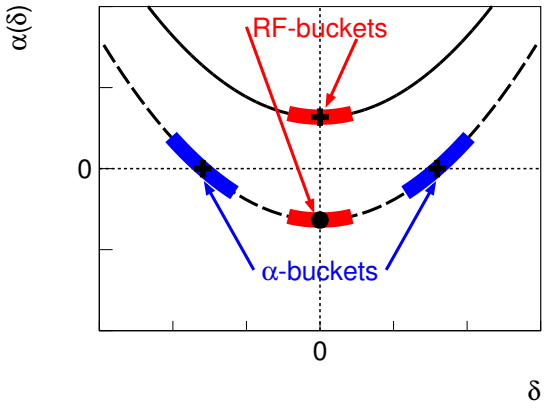

Figure 5.2: Distinction of RF-buckets (red) and α-buckets (blue) at a specific phase φ. RF-buckets are formed around fixed points at $\delta_{\mathrm{FP}} = 0$, in contrast, α-buckets arise around zero-crossings of $\alpha(\delta)$. For stability properties – see text.

A fundamental difference of RF-buckets and α-buckets following this definition is the principle of phase focusing. In the picture of Eqs. 2.28 and 2.32 describing the oscillation in longitudinal phase space, there are two possibilities to generate the right sign combination $\mathrm{d}\varphi \leftrightarrow \mathrm{d}\delta$ for stable storage. In the RF-bucket case, the direction of phase focusing $\mathrm{d}\varphi$ changes whenever δ crosses 0, i.e. $\Delta\varphi$ and δ are oscillating around zero. On the other hand, α-buckets lead to off-momentum

fixed points, there is no zero-crossing in δ. However, phase focusing is generated by $\alpha(\delta)$ crossing 0, i.e. $\Delta\varphi$ and $\alpha(\delta)$ are oscillating around zero. Higher order momentum compaction may be used to generate multiple zero-crossings with different α-bucket characteristics (see section 5.2).

Figure 5.2 shows both bucket types in the δ-$\alpha(\delta)$-plane. Two different momentum compaction functions of the nature $\alpha(\delta) = \alpha_0 + \alpha_2\delta^2$ are plotted with $\alpha_0 > 0, \alpha_2 > 0$ (solid line) and $\alpha_0 < 0, \alpha_2 > 0$ (dashed line). RF-buckets are marked in red, α-buckets are marked in blue. It should be noted that the Fig. 5.2 corresponds to specific phase φ. The RF-bucket in the $\alpha_0 > 0$ case (upper red) is located at the same phase as the α-buckets (blue). At this specific phase the RF-bucket in the $\alpha_0 < 0$ case (lower red) is unstable, however, at the opposite phase the RF-bucket is stable – see Eq. 2.39. Thickened areas mark the range scanned by a selected particle stored inside the bucket at a given oscillation amplitude.

The above definition of RF-buckets and α-buckets uses the nature of the stable fixed point to distinguish between bucket types. An alternative approach is to use the nature of the unstable fixed point defining the bucket separatrix as given in [48] for a linear momentum compaction function. However, the roots of the momentum compaction function and therefore the existence of "new" buckets are a lattice property. In contrast, the separatrix, which is defined by an unstable fixed point of either $\delta = 0$ or $\alpha(\delta) = 0$, is a bucket characteristic dependent on the applied RF.

5.2 Properties of α-Buckets

For reasons of clarity different approximations will be used for investigating the characteristics of α-buckets. A negligible synchronous phase will be assumed as well as negligible wakefield interaction and amplitude dependent orbit lengthening. In addition, an RF voltage of the nature given in Eq. 2.21 will be used.

5.2.1 Hamiltonian and Fixed Points

Alpha-buckets arise around new fixed points introduced by roots of the momentum compaction function $\alpha(\delta) = 0$. Therefore, α-buckets become relevant when approaching quasi-isochronous operation. Using the stated approximations, the Hamiltonian given in Eq. 2.38 simplifies to:

$$\mathcal{H}(\varphi, \delta) = -\beta_0^2 E_0 \delta^2 \int \alpha(\delta)\delta \, \mathrm{d}\delta - \frac{eU_0 \cos(\varphi)}{2\pi h}. \tag{5.4}$$

Occasionally it is convenient to rewrite the momentum compaction function $\alpha(\delta)$ with respect to the fixed point values:

$$\alpha(\delta) = \sum_{i=0}^{n} \alpha_i \delta^i = \alpha_n \prod_{i=0}^{n} \delta - \delta_{\mathrm{FP}_i}, \tag{5.5}$$

where δ_{FP_i} corresponds to the value of the i-th fixed point. Hence, the Hamiltonian considering the three leading orders of $\alpha(\delta)$ controllable at the MLS is given by:

$$\mathcal{H}(\varphi,\delta) = -\beta_0^2 E_0 \delta^2 \left(\frac{\alpha_0}{2} + \frac{\alpha_1}{3}\delta + \frac{\alpha_2}{4}\delta^2\right) - \frac{eU_0\cos(\varphi)}{2\pi h}, \tag{5.6}$$

alternatively in terms of fixed point representation:

$$\mathcal{H}(\varphi,\delta) = -\beta_0^2 E_0 \delta^2 \left(\frac{\alpha_2\delta_{\mathrm{FP}_1}\delta_{\mathrm{FP}_2}}{2} + \frac{\alpha_2\left(-\delta_{\mathrm{FP}_1} - \delta_{\mathrm{FP}_2}\right)}{3}\delta + \frac{\alpha_2}{4}\delta^2\right) - \frac{eU_0\cos(\varphi)}{2\pi h}, \tag{5.7}$$

For convenience, the solutions of $\alpha(\delta)\delta = 0$ for the first few orders in δ are given by:

$$\alpha(\delta) = \alpha_0 \quad \rightarrow \quad \left\{ \delta_{\mathrm{FP0}} = 0, \right. \tag{5.8}$$

$$\alpha(\delta) = \alpha_0 + \alpha_1\delta \quad \rightarrow \quad \begin{cases} \delta_{\mathrm{FP0}} = 0, \\ \delta_{\mathrm{FP1}} = -\frac{\alpha_0}{\alpha_1}, \end{cases} \tag{5.9}$$

$$\alpha(\delta) = \alpha_0 + \alpha_1\delta + \alpha_2\delta^2 \quad \rightarrow \quad \begin{cases} \delta_{\mathrm{FP0}} = 0, \\ \delta_{\mathrm{FP1}} = -\frac{\alpha_1}{2\alpha_2} + \sqrt{\frac{{\alpha_1}^2}{4\alpha_2^2} - \frac{\alpha_0}{\alpha_2}}, \\ \delta_{\mathrm{FP2}} = -\frac{\alpha_1}{2\alpha_2} - \sqrt{\frac{{\alpha_1}^2}{4\alpha_2^2} - \frac{\alpha_0}{\alpha_2}}. \end{cases} \tag{5.10}$$

The fixed points in φ are given by $\varphi_{\mathrm{FP1}} = 0$ and $\varphi_{\mathrm{FP2}} = \pi$. Whether a fixed point is stable or unstable depends on the charge of the particle as well as the sign combination of U_0 and α_0. For electrons with $U_0 > 0$, $\alpha_0 > 0$ the Hamiltonian given in Eq. 5.6 yields the following stable fixed points (φ, δ):

$$\text{stable fixed point 0:} \qquad (\pi, 0), \tag{5.11}$$

$$\text{stable fixed point 1:} \qquad (0, \delta_{\mathrm{FP1}}), \tag{5.12}$$

$$\text{stable fixed point 2:} \qquad (0, \delta_{\mathrm{FP2}}), \tag{5.13}$$

whereas unstable fixed points are located at:

$$\text{unstable fixed point 0:} \qquad (0, 0), \tag{5.14}$$

$$\text{unstable fixed point 1:} \qquad (\pi, \delta_{\mathrm{FP1}}), \tag{5.15}$$

$$\text{unstable fixed point 2:} \qquad (\pi, \delta_{\mathrm{FP2}}). \tag{5.16}$$

5.2.2 α-Bucket Types

The number of α-buckets introduced to the longitudinal phase space depends on the number of roots of the momentum compaction function. Figure 5.1 shows an example of a longitudinal phase space for a momentum compaction function of $\alpha(\delta) = \alpha_0 + \alpha_1\delta + \alpha_2\delta^2 + \alpha_3\delta^3$ with three zero-crossings. There is an RF type bucket indicated by the green area. This bucket always remains in phase space independent of the momentum compaction function. However its ac-

ceptance in phase and momentum depends on $\alpha(\delta)$ and can become negligible. Alpha-buckets arising around the roots of the momentum compaction functions are indicated by red areas. There is a third type of bucket indicated by the blue area. This bucket has no own stable fixed point. However, it encloses multiple fixed stable points, i.e. buckets of red type. Multiple nesting of blue and red type buckets is possible for momentum compaction functions with more than two zero-crossings.

For further investigation, the momentum compaction function will be restricted to the three leading orders: $\alpha(\delta) = \alpha_0 + \alpha_1\delta + \alpha_2\delta^2$. Hence it is possible to name the buckets. Figure 5.3

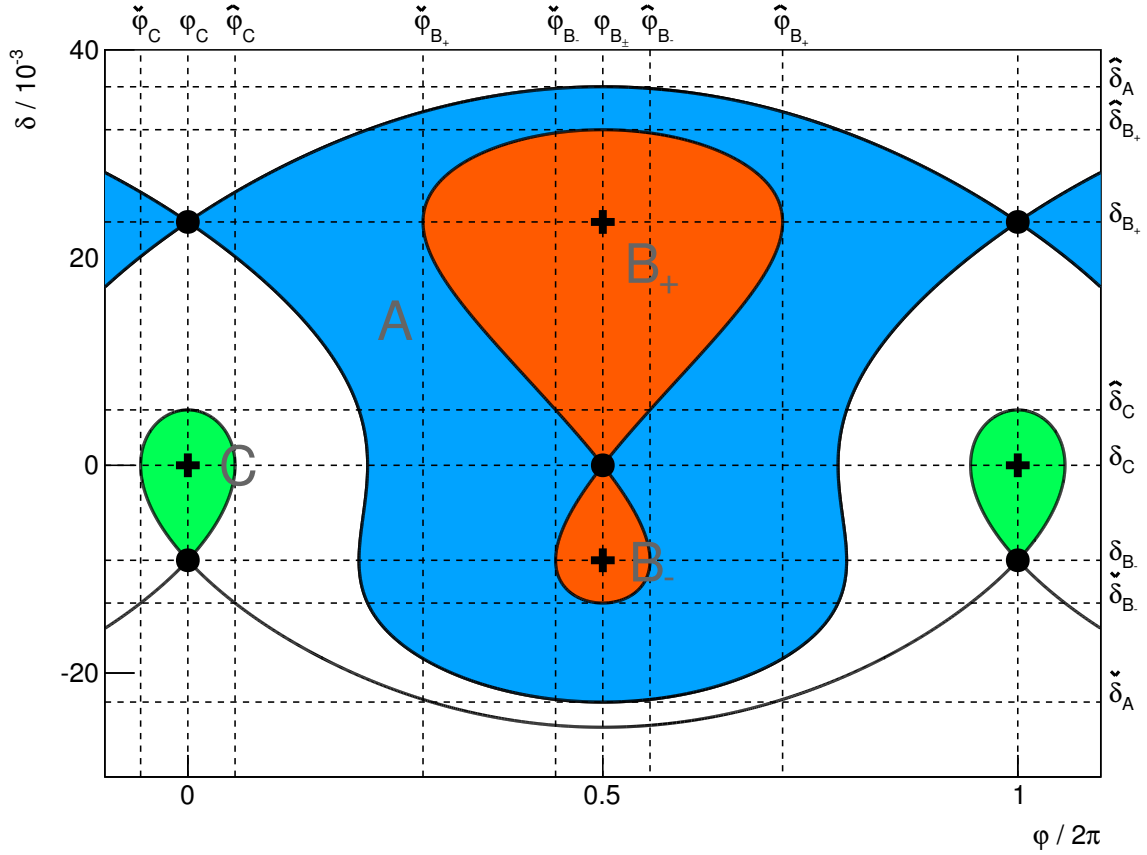

Figure 5.3: Alpha-bucket types and characteristics for $\alpha(\delta) = \alpha_0 + \alpha_1\delta + \alpha_2\delta^2$ dominated by α_2 with $(\alpha_0, \alpha_1 < 0\,;\ \alpha_2 > 0)$.

shows the longitudinal phase space with all three bucket types, that may arise including different bucket properties of interest. The green RF-type bucket will be referenced as "C-bucket". Its fixed point in δ corresponds to $\delta_C = \delta_{\mathrm{FP0}} = 0$ following Eq. 5.10. The red α-buckets will be referenced as "B-buckets", with their fixed points given by $\delta_{B_+} = \delta_{\mathrm{FP1}}$ and $\delta_{B_-} = \delta_{\mathrm{FP2}}$ following Eq. 5.10. The blue bucket surrounding the $B_\pm$-buckets will be named "A-bucket" without a stable fixed point in δ.

Figure 5.4 shows the evaluation of the Hamiltonian given in Eq. 5.4 for $E_0 = 629\,\mathrm{MeV}$,

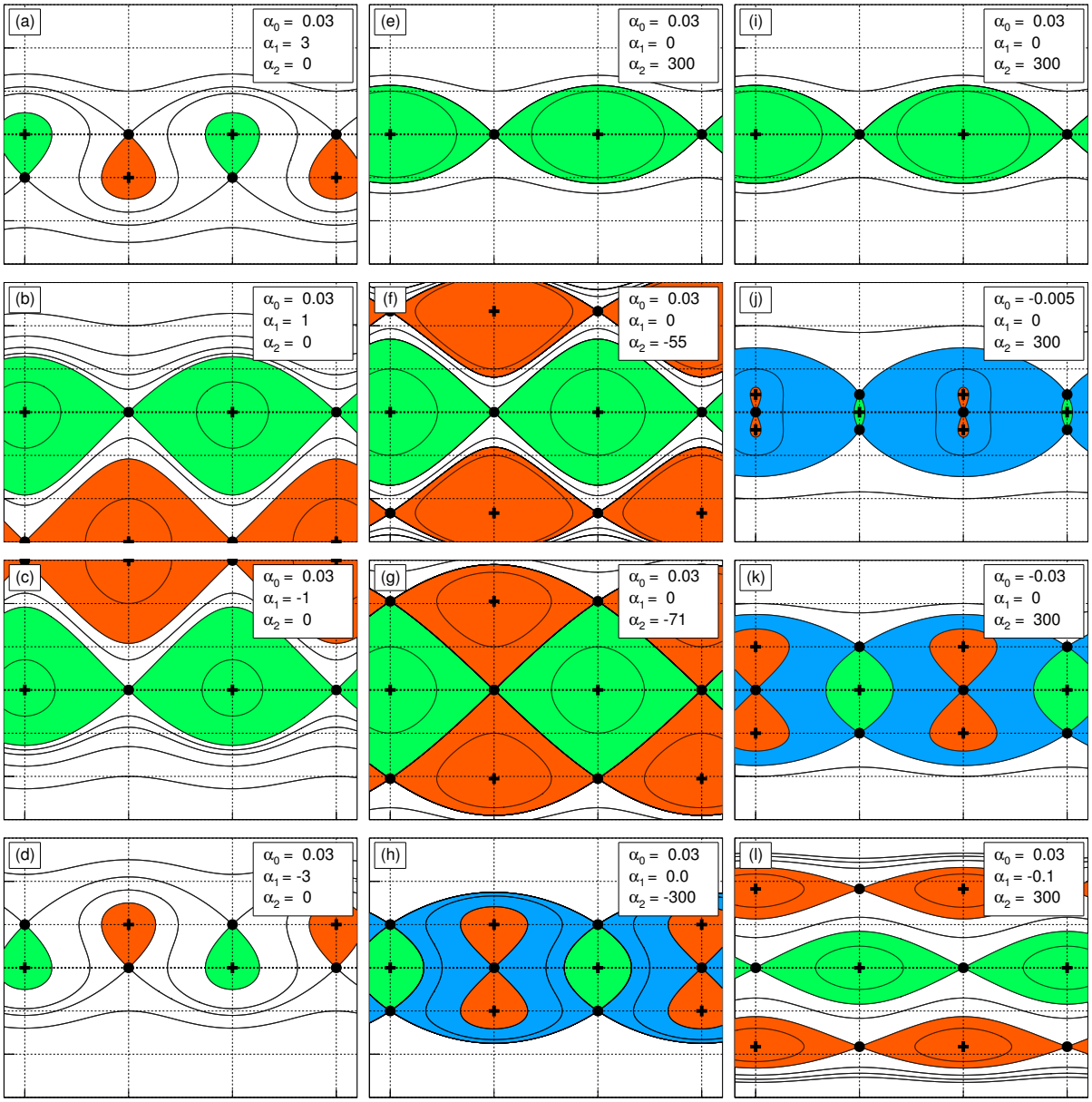

Figure 5.4: Longitudinal phase space dominated by α_1 (a-d) and α_2 (e-l). The vertical axis describes momentum deviation in the range $\delta = -3\% \ldots 3\%$, whereas the horizontal axis describes the phase in the range $\varphi/2\pi = -0.6 \ldots 1.1$.

$U_0 = 500\,\mathrm{keV}$ and $h = 80$. The vertical axis describes momentum deviation in the range $\delta = -3\% \ldots 3\%$, whereas the horizontal axis describes the phase in the range $\varphi/2\pi = -0.6 \ldots 1.1$.

A variation of α_1 is shown in the left column for $\alpha(\delta) = 0.03 + \alpha_1\delta$. The introduction of α_1 to the momentum compaction function forces the existence of a zero-crossing of $\alpha(\delta)$. A single α-bucket exists, therefore, the number of stable buckets in longitudinal phase space is doubled compared to the common RF-bucket-only situation. For small absolute values of α_1 the fixed point of the single α-bucket lies at large momenta. In contrast, the fixed point of the α-bucket is shifted towards smaller absolute values for large absolute values of α_1, making the bucket available for electron storage. However, in this process the momentum acceptances of RF-bucket and α-bucket are reduced drastically. Therefore, α-buckets of α_1-nature are not as attractive for operation at synchrotron light sources as the following α-buckets based on α_2.

The center column of Fig. 5.4 shows a variation of α_2 for a momentum compaction function of $\alpha(\delta) = 0.03 + \alpha_2\delta^2$. For a large α_2 with the same sign as α_0 as shown in Fig. 5.4(e), there is only the RF bucket with reduced momentum acceptance corresponding to Eq. 3.4. Towards smaller absolute values of α_2 with the same sign as α_0 the momentum acceptance of the C-bucket will increase. When α_2 is zero, the C-bucket corresponds to the standard RF bucket. Increasing the absolute value of α_2 with the opposite sign as α_0 leads to a further increase of momentum acceptance of the C-bucket. In addition, due to roots of the momentum compaction function the α-buckets $B_\pm$ arise, whereas the fixed points $\delta_{B_\pm}$ move inwards for larger absolute values of α_2. Figure 5.4(g) shows the combination of α_0 and α_2 where the momentum acceptance of the C-bucket reaches its maximum, as is given by Eq. 3.11 (see section 3.2). Further increasing α_2 in this direction leads to the emergence of the A-bucket and in the process a monotonous decrease of momentum acceptances for $B_\pm$ and C-buckets.

The right column of Fig. 5.4 shows a variation of α_0 for a momentum compaction function of $\alpha(\delta) = \alpha_0 + 300\delta^2$. Figure 5.4(i) corresponds again to the situation where α_0 and α_2 are large and with same signs. Decreasing the absolute value of α_0 now leads to an increase of momentum acceptance for the C bucket. However, when α_0 flips to the opposite sign of α_2 (Fig. 5.4(j)) the C-bucket smoothly turns into an A-bucket. At the formerly stable fixed point of the C-bucket the to $B_\pm$-buckets arise turning the nature of the fixed point unstable. At the formerly unstable fixed point of the C-bucket the inverse process is happening. Its nature is turned stable spawning two unstable fixed points on both sides in momentum. A new C-bucket is formed.

Alpha-buckets could be used to upgrade existing light sources. Therefore, these types of α-buckets may be of interest, which do not reduce the momentum acceptance of the RF bucket. Two longitudinal phase space configurations may be of particular interest. The first interesting case corresponds to Fig. 5.4(g), yielding a maximized momentum acceptance for the RF bucket (+41% compared to $\alpha(\delta) = \alpha_0$) - see section 3.2. Second, the $B_\pm$-buckets could be used to store additional beam under the assumption of sufficient geometrical momentum acceptance. In this case, all buckets are well separated from each other. Third, an interesting phase space configuration is shown in Fig. 5.4(h) involving the A-bucket. This bucket enables the possibility to redistribute particles stored in the $B_\pm$-bucket to the $B_\mp$-bucket exploiting synchrotron radiation damping. For a more detailed review of possible applications of α-buckets see section 5.3.

5.2.3 Momentum and Phase Acceptance

Phase and momentum acceptance of buckets play an important role for injection as well as for storage of particles inside the buckets. To refer to the corresponding acceptance quantities the symbols "ˆ" and "ˇ" will be used to indicate upper and lower boundaries of buckets as depicted in Fig. 5.3. Of particular relevance are the momentum acceptances $\hat{\delta}$ and $\check{\delta}$, as these quantities are determining the quantum as well as Touschek lifetime. The momentum acceptance of α-buckets can be calculated by using the approach presented in section 3.2. However, when applying Eq. 3.2 it is of relevance which unstable fixed point is determining the separatrix. B-buckets may be limited by unstable fixed points in energy as depicted in Fig. 5.3 or by unstable fixed points in phase as depicted in Fig. 5.4(l). For momentum compaction functions with more than two zero-crossings both situations may apply simultaneously as shown Fig. 5.1.

In the case of limitation by an unstable fixed point in δ, Eq. 3.2 yields a notably simple result for the momentum acceptance of the B-buckets [77]:

$$\hat{\delta}_{B_+} = -\frac{2\alpha_1}{3\alpha_2} + \sqrt{\frac{4{\alpha_1}^2}{9{\alpha_2}^2} - \frac{2\alpha_0}{\alpha_2}}, \tag{5.17}$$

$$\check{\delta}_{B_+} = 0, \tag{5.18}$$

$$\hat{\delta}_{B_-} = 0, \tag{5.19}$$

$$\check{\delta}_{B_-} = -\frac{2\alpha_1}{3\alpha_2} - \sqrt{\frac{4{\alpha_1}^2}{9{\alpha_2}^2} - \frac{2\alpha_0}{\alpha_2}}, \tag{5.20}$$

or in terms of fixed point representation:

$$\hat{\delta}_{B_+} = \frac{4}{6}\left(\delta_{B_+} + \delta_{B_-}\right) + \sqrt{\frac{4}{9}\left(\delta_{B_+} + \delta_{B_-}\right)^2 - 2\delta_{B_+}\delta_{B_-}}, \tag{5.21}$$

$$\check{\delta}_{B_-} = \frac{4}{6}\left(\delta_{B_+} + \delta_{B_-}\right) - \sqrt{\frac{4}{9}\left(\delta_{B_+} + \delta_{B_-}\right)^2 - 2\delta_{B_+}\delta_{B_-}}. \tag{5.22}$$

Although the same fixed points in δ can be achieved by different combinations of α_0, α_1 and α_2, the momentum acceptance of both B-buckets is a parameter of their fixed points in δ only. For the bucket extension in phase Eq. 3.2 yields [77]:

$$\hat{\varphi}_{B_\pm} = \varphi_{B_\pm} + \cos^{-1}\left(1 - \frac{2\pi h E_0}{eU_0\cos\left(\varphi_{B_\pm}\right)}\left[\frac{\alpha_0}{2} + \frac{\alpha_1}{3}\delta_{B_\pm} + \frac{\alpha_2}{4}{\delta_{B_\pm}}^2\right]\right), \tag{5.23}$$

$$\check{\varphi}_{B_\pm} = \varphi_{B_\pm} - \cos^{-1}\left(1 - \frac{2\pi h E_0}{eU_0\cos\left(\varphi_{B_\pm}\right)}\left[\frac{\alpha_0}{2} + \frac{\alpha_1}{3}\delta_{B_\pm} + \frac{\alpha_2}{4}{\delta_{B_\pm}}^2\right]\right), \tag{5.24}$$

$$\hat{\varphi}_C = \varphi_C + \min\left(\hat{\varphi}_{B_\pm}\right), \tag{5.25}$$

$$\check{\varphi}_C = \varphi_C - \min\left(\hat{\varphi}_{B_\pm}\right). \tag{5.26}$$

In case of bucket limitation by a non-zero unstable fixed point in φ as it applies to the A-bucket, Eq. 3.2 yields a quartic equation. However, solving the yielded equation for the general case

results in bulky expressions for all acceptance quantities. The same applies for the momentum acceptance of the C-bucket.

5.2.4 Orbit Separation

An important characteristic of α-buckets are different fixed points in δ as given in Eqs. 5.10. Hence, beam stored in α-buckets is intrinsically separated in the δ-plane, which is translated to the transverse plane depending on the dispersion function. How well electron beams stored in the $B_{\pm}$-buckets are transversely separated from each other depends on the relation between emittance, energy spread, α-bucket fixed points and dispersion.

However, an orbit measurement of simultaneously populated α-buckets may yield considerable practical challenges. Fast bunch-by-bunch based orbit diagnostics could distinguish between beam stored in the $B_{\pm}$-buckets and beam stored in the C-buckets. It should be noted, that the bunch spacing is halved compared to the pure RF-bucket situation. If successfully applied, such an approach would yield the possibility perform orbit corrections based on data obtained from the C-bucket beam only. Therefore, standard orbit correction techniques and existing software may be applied. Succeeding an orbit correction of the on-momentum beam, the orbits of beams stored in the $B_{\pm}$-buckets may be manipulated by adjusting the dispersion functions. However, at the MLS an orbit diagnostic with sufficient temporal resolution is not available.

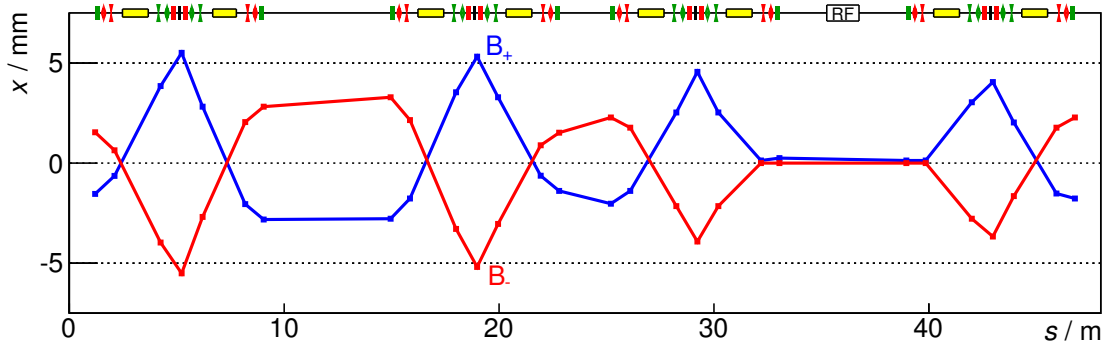

Figure 5.5: Separation of electron beams stored in B_+ and B_- buckets measured by BPMs in two consecutive measurements, whereas either B_+ or B_- buckets were populated. The top axis indicates the position of dipole (yellow), quadrupole (red), sextupole (green) and octupole (black) magnets.

Figure 5.5 shows an orbit measurement of electron beams stored in the $B_{\pm}$-buckets. To generate the data set the machine was set up in low-α user mode, whereas α_2 was set to a large positive value. Following an orbit and chromaticity ($\alpha_1 = 0$) correction applied in the RF-bucket regime, α_0 was decreased to a negative value entering the α-bucket regime. For the orbit measurement, beam was exclusively stored in the B_+-bucket or the B_--bucket. The B_+-bucket is shown in blue, whereas the B_--bucket is shown in red. The measured orbits match the measured behaviour of the dispersion function as depicted in Fig. 3.1. The symmetry of both orbits is due to the symmetry of fixed points, i.e. the setting of $\alpha_1 = 0$.

While following the dispersion function, the beams stored in buckets B_+ and B_- "oscillate" around the on-momentum beam stored in the C-bucket. This is due to the zero-crossings of the dispersion function, which typically are present in low-α optics. For beam optics without zero-crossings of the dispersion function, the beams would propagate "side by side" through the storage ring.

The spatial and angular orbit separation of RF-bucket and α-buckets generated by D and D' is transferred to each of the generated photons beams. This feature enables the option to supply multiple photon beams possibly yielding different properties to users. Figure 5.6 shows the photon beam separation at the IR beam port of the MLS. The $B_\pm$-buckets were populated with different currents $I(B_+) > I(B_-)$ yielding differently bright spots. The overall separation of the photon beams is larger than 6 cm dominated by $D'_{\mathrm{IR}} \approx -0.52$ at the point of observation.

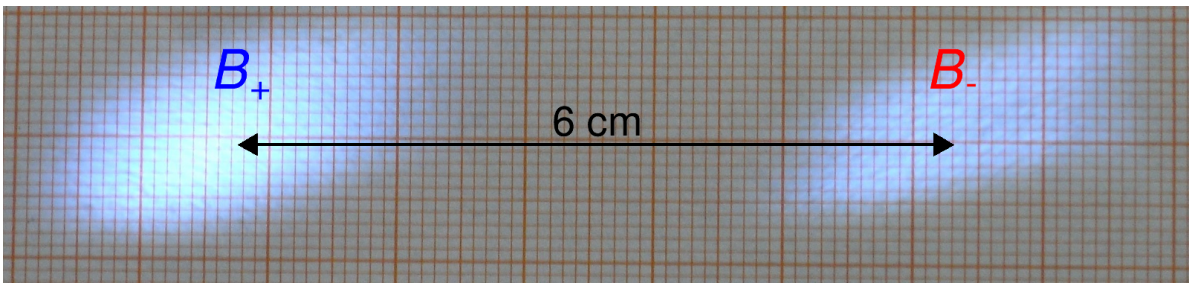

Figure 5.6: Separation of photon beams emitted by beams simultaneously stored in the α-buckets $B_\pm$ measured at the IR beam port of the MLS. A total ring current of 170 mA was stored at a beam lifetime of $\tau \approx 10$ h, whereas the B_+-bucket was populated with higher current than the B_--bucket. The beams are separated in energy by about $\Delta\delta_{\mathrm{FP}} \approx 2\%$.

To investigate the orbit separation of RF-bucket and α-bucket beams, two source point imaging systems [78] have proven to be a valuable tool. Figure 5.7 shows the source points of simultaneously stored beams in B_+, B_- and C. Beam optics were set up with a momentum compaction function of $\alpha(\delta) = -5.4 \times 10^{-4} + 4.0\delta^2$. Measurements were performed at an electron energy of $E = 629$ MeV using beam currents of about 1 mA stored in each bucket [77]. The longitudinal chromaticity ξ_s was varied using an orthogonalized combination of all three sextupole families, whereas the transverse chromaticities were kept constant at $\xi_{x,y} \approx 0$. The covered range of $\xi_s = -0.2 \ldots 0.2$ corresponds to a variation of $\alpha_1 = -4.4 \times 10^{-2} \ldots 4.4 \times 10^{-2}$ following Eq. 3.29. Dashed black lines in Fig. 5.7 show the calculated position $x_D = D\delta_{\mathrm{FP}}$, with fixed points given in Eq. 5.10. As expected, the fixed point of the C-bucket does not depend on α_1. Deviation from the predicted positions of source points of the $B_\pm$ are within limits of the uncertainties of $\alpha_{0,1,2}$ and D. The right column of Fig. 5.7 shows a sketch of the momentum compaction function for each measurement. Similar measurements were performed varying α_0 as well as α_2 with $\alpha_1 = 0$. Therefore, the measured fixed point positions as a function of $\alpha_{0,1,2}$ are agreement with theory within the involved measurement uncertainties.

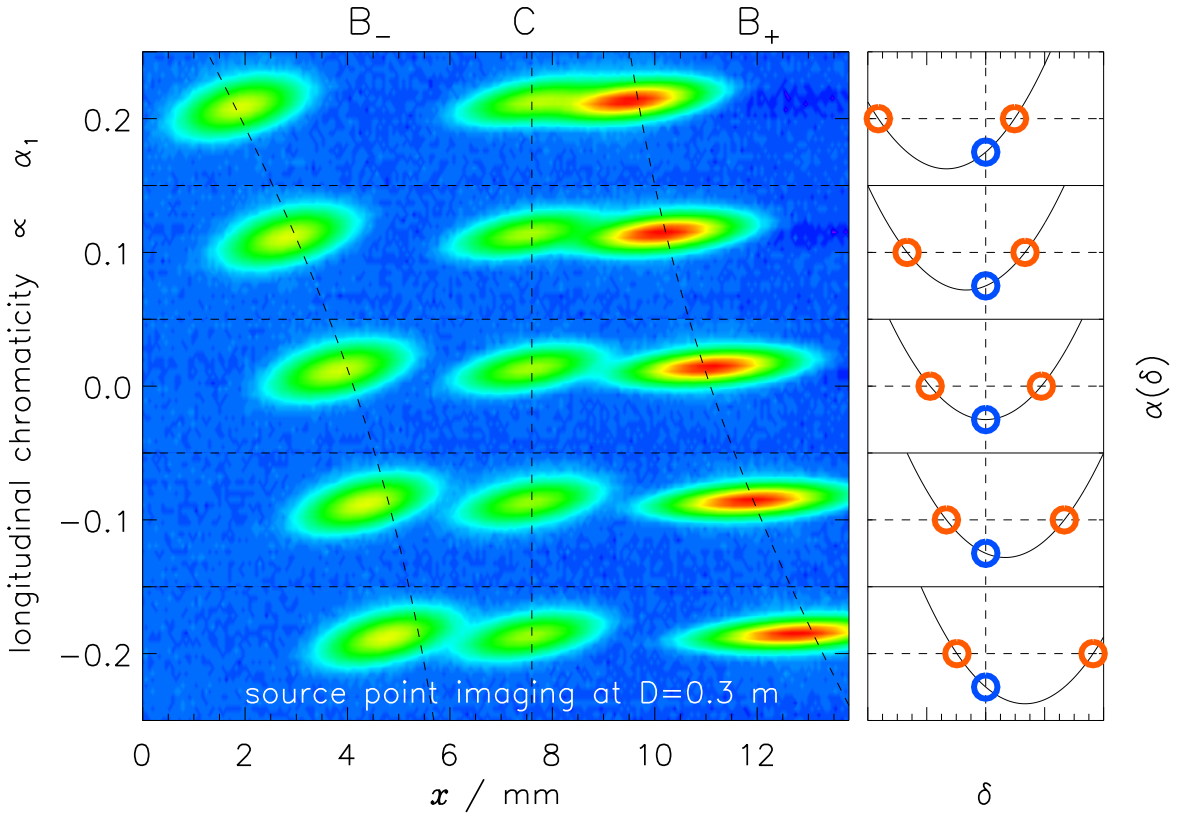

Figure 5.7: Measurement of synchrotron radiation source points of simultaneously populated buckets B_+, B_- and C. An optical imaging system at an observation point with $D \approx 0.3\,\mathrm{m}$ was used while varying the longitudinal chromaticity ξ_s.

5.2.5 Tunes and Bunch Lengths

Tune characteristics of α-buckets can be obtained by investigating small amplitude oscillation around the fixed points [23, 77]. Therefore, the Hamiltonian given in Eq. 5.6 is evolved for small amplitudes $(\Delta\varphi, \Delta\delta)$ around the fixed point $(\varphi_{B\pm,C}, \delta_{B\pm,C})$. Within the approximation of small amplitudes, only orders of $\mathcal{O}(\Delta\varphi) \leq 2$ and $\mathcal{O}(\Delta\delta) \leq 2$ were regarded yielding a harmonic oscillator with the characteristic frequency of:

$$B_\pm\text{-buckets}: \qquad Q_{B_\pm} = \frac{f_{s_{B_\pm}}}{f_{\mathrm{rev}0}} = \sqrt{\frac{heU_0\cos(\varphi_{B_\pm})}{2\pi E_0}(2\alpha_0 + \alpha_1\delta_{B_\pm})}, \tag{5.27}$$

$$C\text{-buckets}: \qquad Q_C = \frac{f_{s_C}}{f_{\mathrm{rev}0}} = \sqrt{\frac{heU_0\cos(\varphi_C)}{2\pi E_0}\alpha_0}, \tag{5.28}$$

or expressed as ratio:

$$\frac{f_{s_{B_\pm}}}{f_{s_C}} = \sqrt{2 + \frac{\alpha_1}{\alpha_0}\delta_{B_\pm}}. \tag{5.29}$$

A direct result is that the longitudinal tune in the C-bucket is independent from higher order momentum compaction and corresponds to the RF-bucket tune. Additionally, for $\alpha_1 = 0$ the tune in the $B_\pm$-buckets is a factor of $\sqrt{2}$ larger than in the C-bucket, independent of the values of α_0 and α_2. Concurrent results can be obtained by a different technique evaluating the local momentum compaction factor at the fixed points $\alpha_p(\delta_{\mathrm{FP}})$ as described in section 4.3.

Investigation of a momentum compaction function of the nature $\alpha(\delta) = \alpha_0 + \alpha_1\delta$, i.e. $\alpha_2 = 0$, yields a single α-bucket. The longitudinal tune in this α-bucket is the same tune as in the RF-bucket given in Eqs. 2.33 or 5.28.

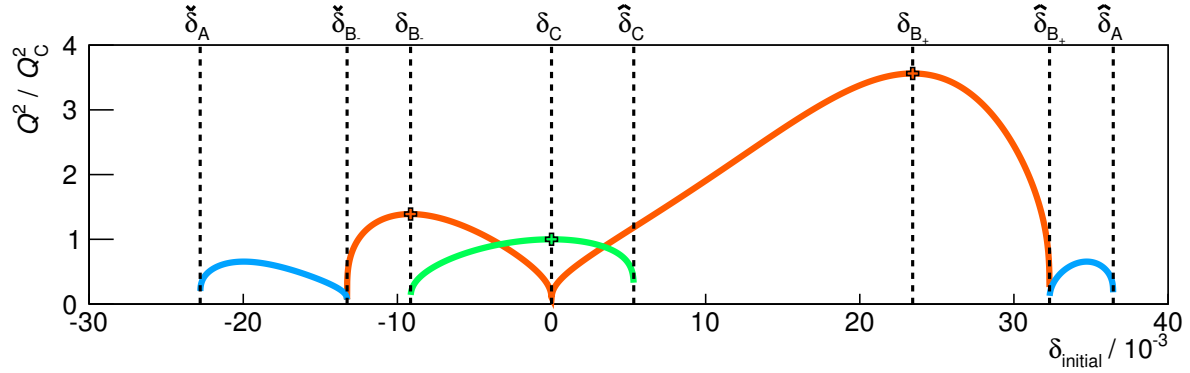

Figure 5.8: Normalized synchrotron tune in α-buckets A (blue), $B_\pm$ (red) and C (green) as a function of particle momentum derived from particle tracking. Particles were started at the corresponding stable phase (depending on the bucket) and tracked for 10^7 turns, whereas the initial momentum deviation $\delta_{\mathrm{initial}}$ was varied. The phase space configuration corresponds to Fig. 5.3.

Figure 5.8 shows results of particle tracking simulations as described in section 4.3. The applied parameters correspond to the phase space depicted in Fig. 5.3. Particles were tracked with initial parameters of $(\varphi = 0, \delta_{\mathrm{initial}})$ as well as $(\varphi = \pi, \delta_{\mathrm{initial}})$. The synchrotron oscillation tune was obtained by means Fourier analysis and is presented normalized to the tune obtained at the fixed point of the C-bucket $(\varphi = 0, \delta_{\mathrm{initial}} = 0)$. The color code was chosen such to indicate the bucket membership as shown in Fig. 5.3. The cross symbol marks the tune ratio at the stable fixed points calculated following Eq. 5.29. For increasing momentum deviation from the fixed point, i.e. $\delta_{\mathrm{initial}} - \delta_{\mathrm{FP}}$, the oscillation frequency decreases to zero upon the point of reaching the separatrix. On the separatrix, or more precisely in the vicinity of unstable fixed points, the longitudinal motion freezes to zero due to an infinitely slow motion.

Figures 5.9 and 5.10 show raw data of a measurement of the synchrotron oscillation frequency with simultaneously populated RF-bucket and $B_\pm$-buckets. The measurement was performed at an electron energy of $E = 629\,\mathrm{MeV}$ and an applied RF voltage of $U = 500\,\mathrm{kV}$. The mo-

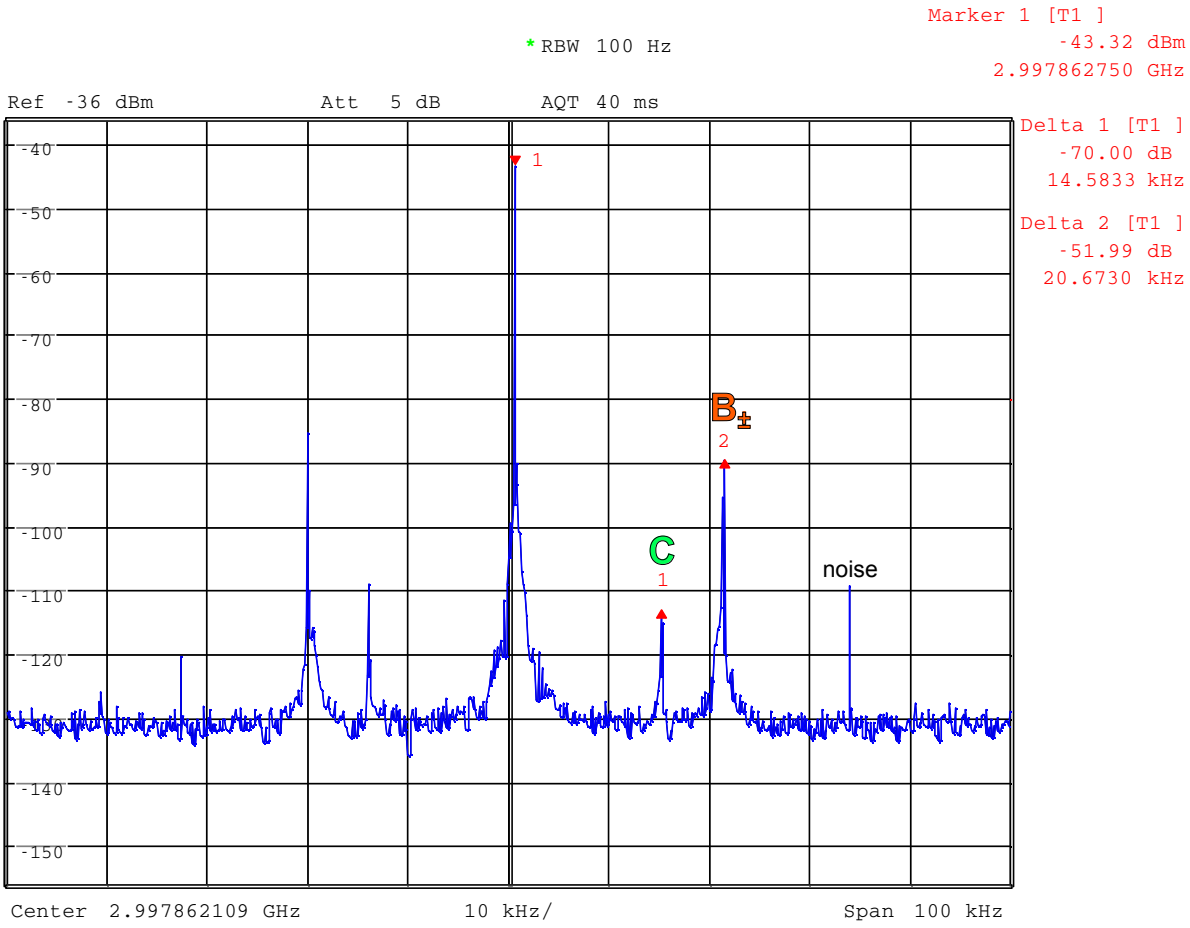

Figure 5.9: Measured synchrotron oscillation frequencies with simultaneously populated B_+, B_- and C-buckets for a momentum compaction function of $\alpha(\delta) \approx -5.4 \times 10^{-4} + 4\delta^2$.

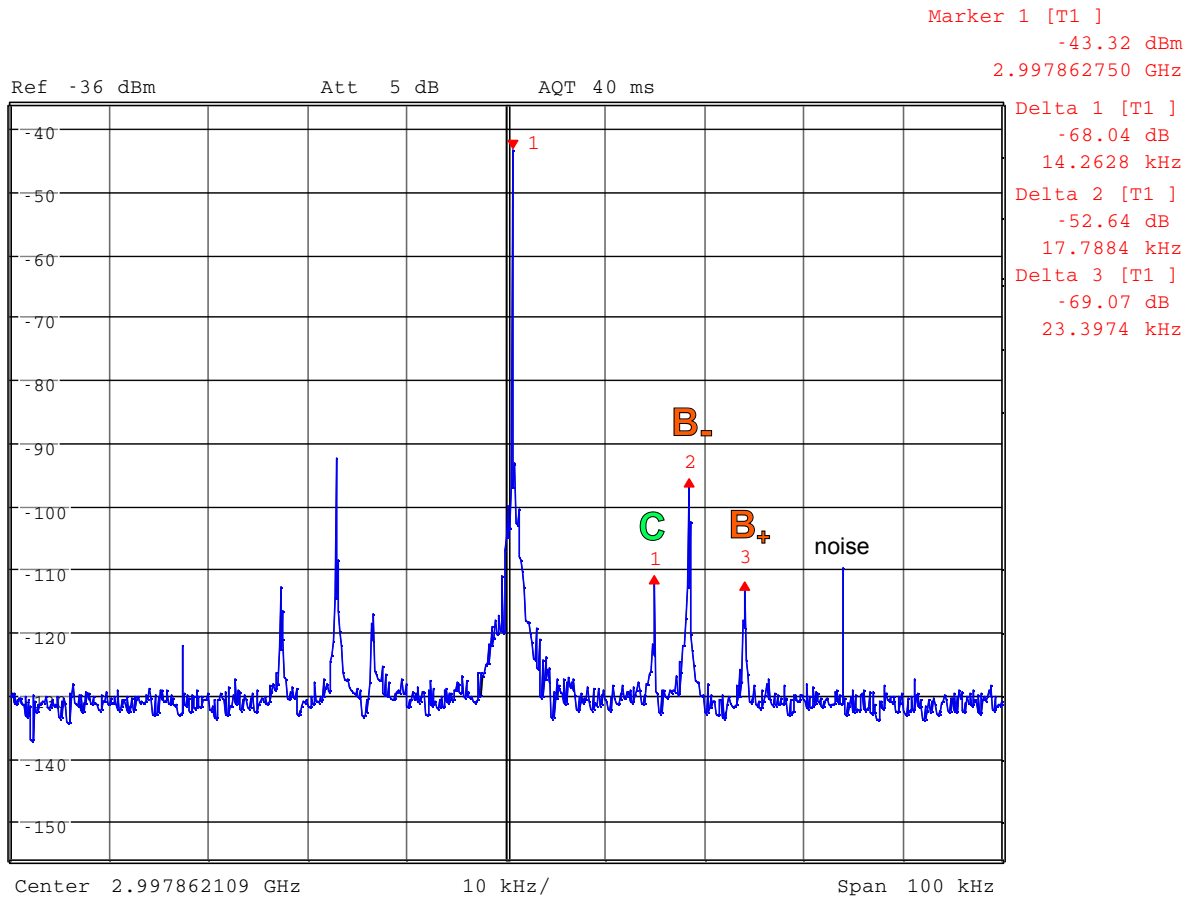

Figure 5.10: Measured synchrotron oscillation frequencies with simultaneously populated B_+, B_- and C-buckets for a momentum compaction function of $\alpha(\delta) \approx -5.4 \times 10^{-4} - 0.025\delta + 4\delta^2$.

mentum compaction function was adjusted to $\alpha(\delta) = -5.4 \times 10^{-4} + 4.0\delta^2$ for Fig. 5.9 yielding identical synchrotron oscillation frequencies in the $B_{\pm}$-buckets, which are a factor of $\sqrt{2}$ larger than in the C-bucket as predicted by Eq. 5.29. This relation can be generalized for higher order momentum compaction functions of the nature of $\alpha(\delta) = \alpha_0 + \alpha_{2n}\delta^{2n}$ yielding a tune factor of $\sqrt{2n}$. An additional characteristic frequency is measured at $f = 33\,\mathrm{kHz}$, which is due to an amplitude and phase modulation of the RF-voltage introduced by the applied power supply. By introducing a longitudinal chromaticity, as described in the last section, a non-vanishing value of $\alpha_1 = -2.5 \times 10^{-2}$ was introduced. Therefore, in Fig. 5.10, the symmetry of the momentum compaction function was broken, i.e. the synchrotron oscillation frequencies of the $B_{\pm}$-buckets split as given in Eq. 5.27. The absolute values of the measured synchrotron oscillation frequencies are in agreement with Eqs. 5.27 and 5.28 within the limits of the involved uncertainties. Alpha-buckets were also observed at the storage ring BESSY II, where the splitting of the oscillation frequency has proven to be a sensitive detection mechanism for residual α_1.

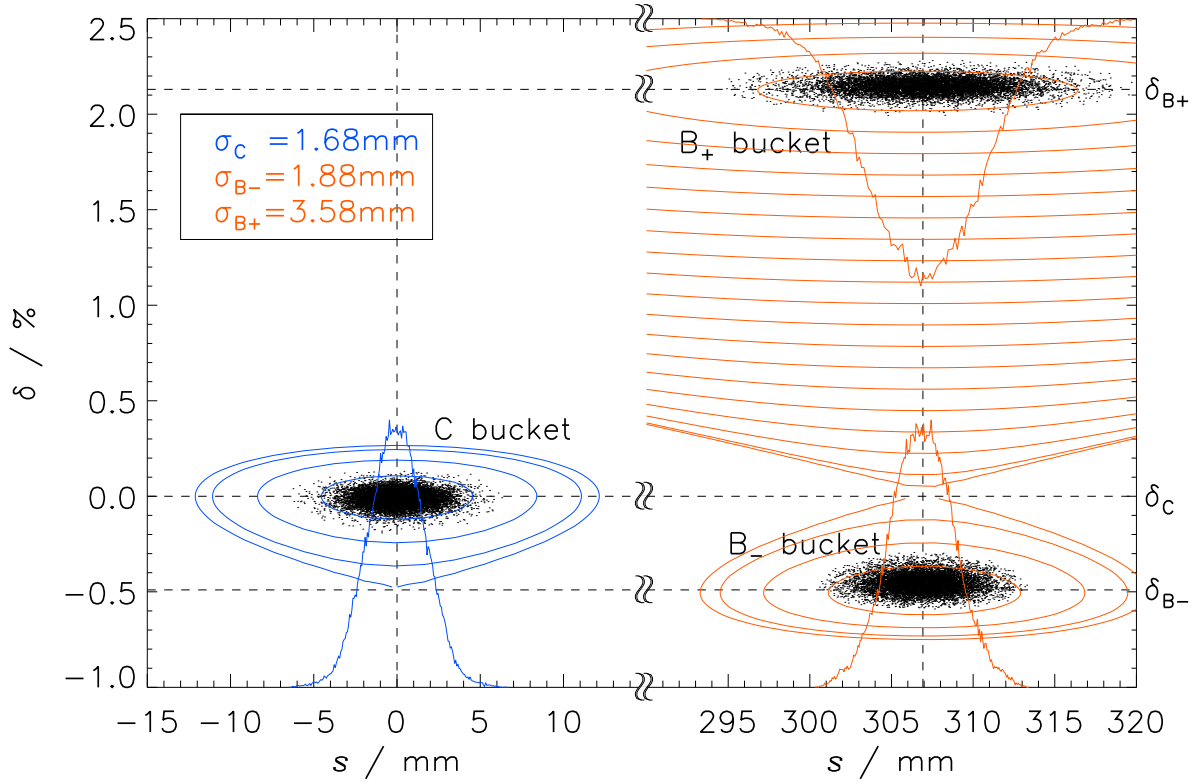

Figure 5.11: Comparison of analytical model and particle tracking for asymmetrical α-buckets. The momentum compaction function corresponds to $\alpha(\delta) = -1.45 \times 10^{-3} - 0.23\delta + 14\delta^2$. Particle tracking was performed with MAD-X including synchrotron radiation at $E_0 = 629\,\mathrm{MeV}$ and $U_0 = 250\,\mathrm{kV}$.

The bunch length in the RF-bucket can be related to the synchrotron oscillation frequency as given in Eq. 2.44. Evaluating the Hamiltonian given in Eq. 5.6 within the limits of small amplitude oscillation yields the following result for the bunch lengths:

$$\sigma_{B_\pm} = \frac{\delta_0 c}{f_{\mathrm{rf0}}} \sqrt{\frac{hE_0}{2\pi e U_0 \cos\left(\varphi_{B_\pm}\right)} \left(2\alpha_0 + \alpha_1 \delta_{B_\pm}\right)}, \tag{5.30}$$

$$\sigma_C = \frac{\delta_0 c}{f_{\mathrm{rf0}}} \sqrt{\frac{hE_0}{2\pi e U_0 \cos\left(\varphi_C\right)} \alpha_0}, \tag{5.31}$$

where δ_0 is the rms energy spread. Therefore, as long as the energy spread of the particles is small enough to stay in the locally harmonic potential the ratio of bunch lengths corresponds to the ratio of synchrotron oscillation frequencies. Combining Eqs. 5.27, 5.28, 5.30 and 5.31 yields:

$$\frac{f_{s_{B_\pm}}}{f_{s_C}} = \frac{\sigma_{B_\pm}}{\sigma_C}. \tag{5.32}$$

Figure 5.11 shows a comparison of analytical model and particle tracking simulations. Colored solid lines correspond to closed trajectories around the fixed points obtained from the Hamiltonian given in Eq. 5.4 for a momentum compaction function of $\alpha(\delta) = -1.45 \times 10^{-3} - 0.23\delta + 14\delta^2$. The storage ring model for MAD-X was set up with the same $\alpha(\delta)$. Particle tracking was conducted for 10×10^6 turns, corresponding to more than 100 times the longitudinal damping time. Synchrotron radiation damping as well as quantum excitation were included. Tracking results are in agreement with the analytical prediction. The bunch lengths for all three buckets are different, which is expected from Eqs. 5.30 and 5.31. It can be shown, that the C-bucket will always provide the shortest bunch lengths, which applies for the presented example. However, the particle distribution in buckets C and B_- already show signs of a non-harmonic potential. This is particularly distinctive when examining the projection of the particle distribution in δ. Therefore, the approximation for the bunch length given in Eqs. 5.30 and 5.31 may not be applied.

5.3 Applications

Application of α-buckets in user operation of electron storage rings may potentially add new qualities to the delivered photon beam. Operation with α-buckets based on α_1 is the first order approach but would result in a drastically reduced momentum aperture of the RF-bucket, which conflicts with the idea of upgrading existing storage ring concepts with α-buckets. Therefore, in this section possible applications of α-buckets of α_2-nature will be discussed.

To generate α-buckets based on α_2, an octupole or exploitation of higher order effects from sextupoles is required to be able to generate a sufficiently large α_2. However, introducing strong octupolar fields may indicate the need to correct amplitude dependent tune shifts in the transverse planes. In addition, there are diagnostic difficulties when operating a storage ring with simultaneous beams on different reference orbits such as current or orbit measurement. Eventually these difficulties seem to be manageable and not of principle nature, therefore several application ideas were tested at the MLS in the scope of its machine capabilities.

5.3.1 Multi-Filling Operation

One application of α-buckets could be to offer multiple filling patterns for user experiments. The user demands for the time structure of the synchrotron radiation are quite versatile depending on the conducted experiment. Commonly, in user operation a homogeneous filling pattern is applied, i.e. every bucket is populated with roughly the same amount of current. Additionally, a gap in the order of 100 ns is introduced for ion clearing. At BESSY II a single bunch in the center of the gap is populated to generate a quasi single bunch [79]. However, there is a user community interested in real single bunch operation conducting experiments such as time of flight spectroscopy. There are efforts to satisfy these users by applying fast choppers in the MHz regime to extract photons from a single bunch inside the ion clearing gap [80], however, this approach is linked to technical challenges. Therefore, quite a number of storage rings offer the dedicated mode of high current single bunch operation for few weeks per year.

In addition, there are concepts to generate pseudo single bunches. One concept uses a fast kicker magnet to deliver a kick with the same amplitude every turn to selected bunches [81]. These bunches perceive the fast kicker magnet as a static bump. Therefore they are deflected to an off-design orbit. Another concept involves exciting a single bunch, commonly done by bunch-by-bunch feedback systems such as [82]. As the selected bunch performs oscillations, its radiation coil oscillates as well. Users can use photons originating from the single bunch, by blanking out the radiation coils of the unexcited bunches using apertures. However, these concepts have the disadvantage of applying non-static fields or being restricted to a small fraction of available intensity.

Alpha-buckets provide the potential to simultaneously supply different filling patterns to the users, making use of the orbit separation presented in section 5.2.4. Neither a loss of intensity nor pulsed elements are involved. An example mode of operation could be to operate a homogeneous fill pattern in the C-bucket and a high current single bunch in an off-energy bucket. The distortion applied to the homogeneous filling by applying a C-bucket instead of an RF bucket would be minimal or in the best case even advantageous. Any experiment using a beam port with a relevant value of the dispersion function D or D' could tune their beamline optics to select

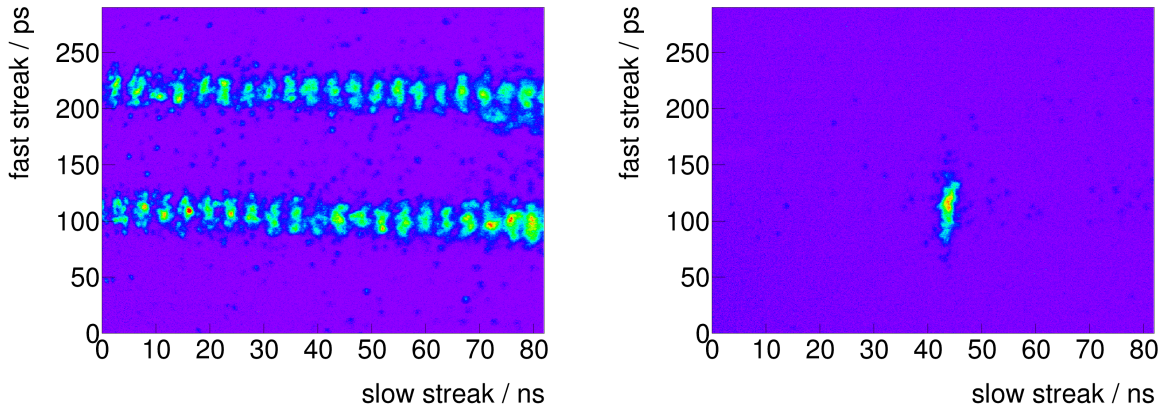

(a) homogeneous filling pattern in bucket B_-

(b) single bunch in in bucket B_+

Figure 5.12: Simultaneous operation of multiple filling patterns applying α-buckets at the MLS. Homogeneous filling pattern (a) and single bunch (b) measured using a streak camera at the IR beam port.

for the single bunch rather than the homogeneous filling. In principle one could simultaneously use as many different filling patterns as there are alpha buckets.

It was demonstrated at the MLS to simultaneously and stably operate two different filling patterns in α-buckets. The experiment was conducted starting with a homogeneous filling pattern in the RF-bucket at $E = 629\,\mathrm{MeV}$. Maximum octupole strength was applied yielding $\alpha_2 = 14$. Subsequently, α_0 was reduced slowly, while continuously tuning the sextupole families such that $\alpha_1 = 0$ was ensured. After crossing to negative α_0 the current was stored in the $B_\pm$-buckets. The RF frequency was used to redistribute currents between $B_\pm$ until both buckets were filled with the same amount of current measured by the source point imaging systems. Then α_0 was reduced further to increase the separation of the $B_\pm$ buckets with a final value of $\alpha_0 \approx -6 \times 10^{-4}$. The horizontal chromaticity was increased to about $\xi_x \approx 0.5$ to separate the horizontal tunes of both $B_\pm$. The multi-bunch feedback system of the MLS [82] was applied to selectively excite all but one bunch stored in the B_+ bucket at the horizontal tune. Due to the chromaticity the bunches stored in the B_- were not excited resonantly. The excitation amplitude was increased until no further lifetime reduction was observed. To measure the filling patterns a combination of stripline measurement, two source point imaging systems and streak camera was used [78, 83]. One source point imaging system was used to check that the overall intensity of the homogeneous filling pattern stored in B_- did not change. The second imaging system was used to confirm the reduction of intensity stored in B_+. Afterwards a streak camera was used to measure the time structure of the different photon beams at the IR beamline. Figure 5.12(a) shows the streak images recorded from the B_- beam, whereas Fig. 5.12(b) shows the streak of the B_+ beam. Larger streak timescales were used to ensure the distance of one revolution between the photon pulses.

This hybrid filling was operated for a few hours to check for long term stability as well as

possibly leaking currents to from $B_- \rightarrow B_+$. Leak currents could not be observed and therefore have to be lower than 10 μA.

As a next step the current per bucket position was measured applying a stripline technique [79]. The sum of all bunch currents matched the value measured with current transformers indicating that effects originating from spatial distribution of the currents can be neglected. Finally the remaining single bunch in the B_+ bucket was kicked out and a second fill pattern measurement was conducted. Only one bucket showed a significant difference to the first measurement

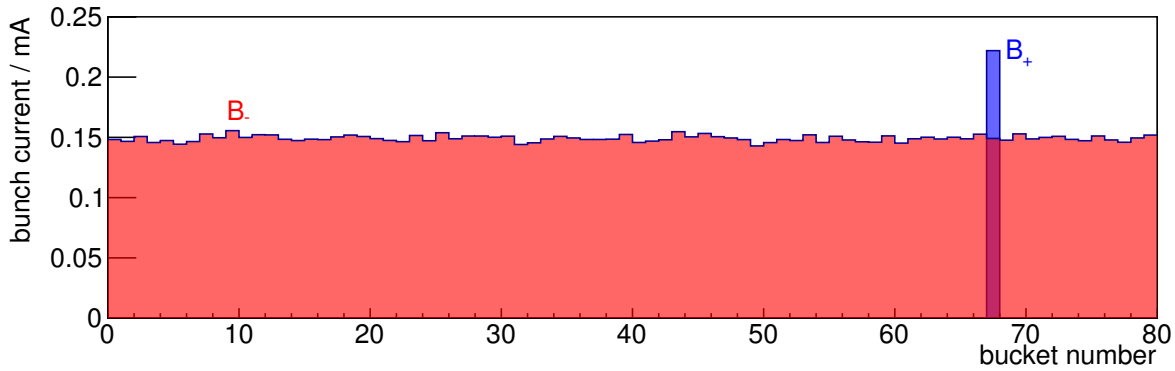

Figure 5.13: Simultaneous operation of multiple filling patterns: A homogeneous filling pattern (red) and a single bunch (blue).

indicating the missing contribution of the single bunch. Figure 5.13 shows the measurement of the filling in the B_- bucket (red) as well as the difference between both measurements (blue).

5.3.2 α-Bucket Topup

An interesting α-bucket type is the A-bucket, which by itself has no "own" stable fixed point. Instead, this bucket type has two separatrices at inner and outer side of the bucket as shown in Figs. 5.1, 5.3, and 5.4. The absence of a stable fixed point makes the bucket unattractive for stable storage of electrons under the impact of radiation damping. However, this bucket characteristic enables another interesting option - "α-bucket current redistribution". Particles stored in one of the $B_\pm$-buckets, may be kicked out of the bucket by radiation excitation, scattering or external forces. In the presence of an A-bucket, these particles do not necessarily get lost. They can be temporally stored. Radiation damping then forces particles to move towards stable fixed points, which are beyond the inner separatrix, i.e. inside the $B_\pm$-buckets. These dynamics can be exploited to redistribute electrons from the B_+-bucket to the B_--bucket or vice versa. This option was experimentally investigated at the MLS, whereas the following means of current redistribution were tested:

1. manipulation of $\alpha(\delta)$
2. external longitudinal excitation
3. RF-detuning

Alpha-bucket characteristics are dominated by the momentum compaction function as presented in section 5.2. In particular the position of the fixed points and therefore the momentum acceptance as given in Eqs. 5.10 and 5.17-5.22. Therefore, by adjusting $\alpha(\delta)$ it is possible to reduce the momentum acceptance of either B_+ or B_--bucket towards zero. Consequently, the momentum acceptance of the selected bucket will not be large enough to store the natural energy spread, i.e. the longitudinal quantum lifetime of this bucket becomes short. However, electrons lost from the affected B-bucket are not necessarily lost for storage. Instead, electrons may populate the A-bucket and get the chance to be damped back inside one of the $B_\pm$-buckets. Therefore, when the momentum acceptance of one of the B-buckets become too small compared to the natural energy spread, its electrons may pass to the other B-bucket, which still could provide sufficient momentum acceptance. In this way a continuous particle drift can be achieved.

The opposite possibility to depopulate the $B_\pm$-buckets is exciting the particle oscillation amplitude in longitudinal phase space exceeding the bucket momentum acceptance, which is kept fixed in this case. At the MLS this can be done by a phase modulation of the main RF cavity voltage. The frequency of the phase modulation is chosen close to the synchrotron oscillation frequency to excite particles resonantly. However, this technique may only be used for particle redistribution if a non-vanishing longitudinal chromaticity is applied that leads to a relevant splitting of the synchrotron oscillation frequencies $f_{s_{B_\pm}}$. Depending on the direction of particle redistribution the excitation may has to be applied in a pulse way (see section 5.2.5).

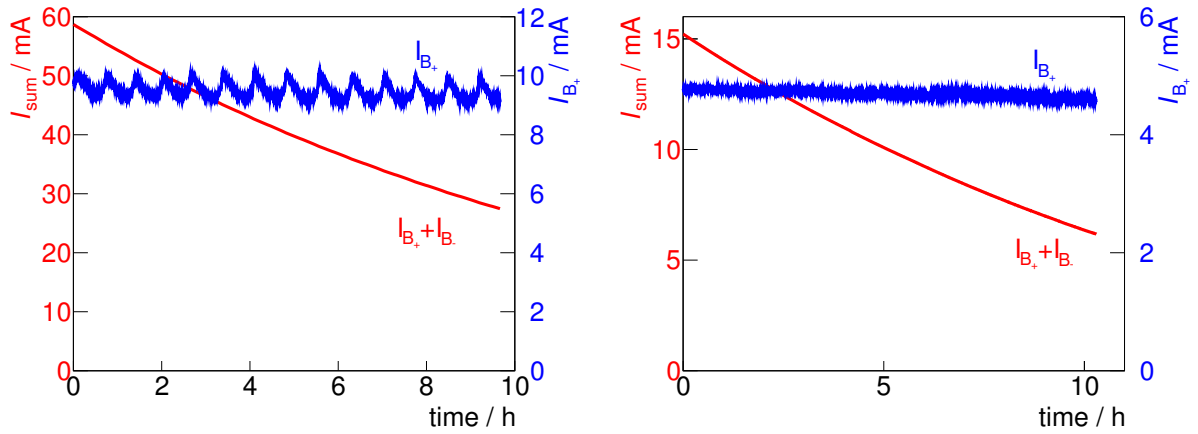

(a) current feedback

(b) lifetime feedback

Figure 5.14: Demonstration of α-bucket top-up over several hours of operation. The current stored in the B_+-bucket is shown in blue, whereas the integral current $I = I_{B_+} + I_{B_-}$ is shown in red. Left: A current feedback was applied, "injecting" from B_- to B_+ whenever a current threshold was reached. Right: A lifetime feedback was applied, adjusting the drift rate from B_- to B_+ such to exactly compensate the lifetime losses.

A demonstration experiment was conducted at the MLS to show the robustness of particle redistribution in α-buckets. Therefore, synchrotron imaging systems [78] in dispersive sections

were used as means to distinguish between current stored in the B_+ and B_--buckets. However, the dynamic range (8 bit) of these systems limited current and lifetime resolution. As a measure of current redistribution a change of f_{rf} was applied for reasons of simplicity. The bucket B_+ was arbitrarily chosen as "user bucket", whereas bucket B_- served as reservoir bunch.

Figure 5.14(a) show an α-bucket top-up run. This means, whenever the current stored in the B_+ fell below a threshold of $I(B_+) < 9\,\mathrm{mA}$ a current transfer from the reservoir bucket was initiated. When the current in the user bucket exceeded a value of $I(B_+) > 10\,\mathrm{mA}$, the current transfer was stopped. The MLS was operated for more than 10 h in this operation mode, to demonstrate the stability.

Figure 5.14(b) corresponds to a slightly different approach. By manipulating $\alpha(\delta)$ in terms of manipulating α_0, α_1 and α_2 (see Eqs. 5.17-5.22) the momentum acceptance of the $B_\pm$-buckets can be adjusted very accurately. Therefore, a mode of operation is feasible, where the lifetime losses of the user bucket are exactly compensated by a continuous current transfer from the reservoir bucket. Therefore, the lifetime of the user bucket was calculated by measuring the current over long time intervals of $t \approx 10\,\mathrm{min}$ with an active feedback loop to adjust the momentum acceptances of the $B_\pm$-buckets. The resulting current stability in the conducted experiment is maintained for over 10 h and is limited by the bucket-resolved current measurement. This mode of operation could be applied for measurement tasks that demand high temporal short and long term stability preventing injection as well as decay mode.

5.3.3 Multi-Bunch-Length Operation

At the time of writing this work, there is no storage ring based synchrotron light source operating that offers short bunches in the picosecond regime in standard user operation. There are multiple storage rings, that offer dedicated short bunch operation, whereas the user time is limited to an order of a few weeks per year.

The main reason is that short bunch operation is subject to additional effects leading to beam quality degradation at high bunch currents. The most dominant one is the bursting instability threshold - an instability arising at a large bunch charge in short bunches - see chapter 6. Increasing this current threshold to values compatible with standard user operation is one of the challenges for next generation storage rings. In addition, users of short bunches have mutually exclusive demands. Users of short pulse of incoherent synchrotron radiation are mainly interested in high brilliance and high bunch to bunch stability. In contrast, users of coherent synchrotron radiation are interested in high lifetimes to support high resolution FTIR spectrometry as well as to make use of broader spectra in the bursting regime.

There is a concept currently under development to offer long and short bunches simultaneously in a storage ring [13, 84]. It is based on a voltage beat generated by multiple RF cavities. A main cavity resupplies the synchrotron radiation losses to the beam, whereas two high gradient superconducting cavities at fractional higher harmonics are used to adjust the voltage gradient at the synchronous phase. The basic idea is to superimpose the voltage gradients of the two superconducting cavities at one bucket position, whereas it cancels at another another bucket position. Figure 5.15(a) visualizes the RF voltage beat concept, that could be used to upgrade the BESSY II storage ring. Figure 5.15(b) shows a calculation for the shift of the bursting threshold for BESSY II when increasing the voltage gradient by a factor of 100. BESSY II user

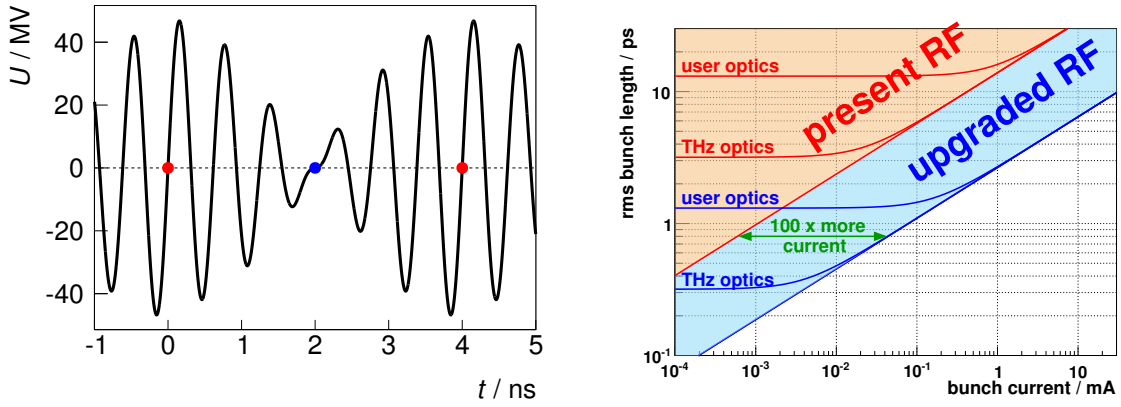

(a) BESSY$^{\text{VSR}}$ RF beat scheme

(b) shift of the bursting threshold

Figure 5.15: BESSY$^{\text{VSR}}$ - an upgrade for BESSY II. Left: RF voltage beat scheme to generate multiple RF-buckets featuring long bunches (blue dot) and short bunches (red dot). Right: Shift of the bursting threshold by applying a factor of 100 times larger gradient at the position of the short bunches.

optics are characterized a momentum compaction factor of $\alpha_0 \approx 7 \times 10^{-4}$, whereas present THz optics correspond to low-α operation at $\alpha_0 \approx 3.5 \times 10^{-5}$. Colored areas indicate the possibility of stable operation with equilibrium bunches. For a fixed bunch length, an increase of the voltage gradient by a factor of 100 yields a 100 times higher threshold current [85].

Alpha-buckets offer another approach of simultaneous operation of multiple bunch lengths [77]. Whereas the RF voltage beat based approach separates the bunches in longitudinal phase space in the phase plane, α-buckets may do the same in the energy plane. The lengths of bunches stored in α-buckets is given in Eq. 5.30. Storing bunches in α-buckets at different bunch lengths can be achieved by different means.

A direct and versatile approach is to use a high even order multipole to generate a momentum compaction function of:

$$\alpha(\delta) = \alpha_0 + \alpha_{2n}\delta^{2n}, \tag{5.33}$$

with fixed points at,

$$\delta_{\text{FP}} = \pm \sqrt[2n]{-\frac{\alpha_0}{\alpha_{2n}}}. \tag{5.34}$$

In small amplitude approximation, the ratio of synchrotron oscillation frequencies between particles stored in the $B_\pm$ bucket and the C bucket is given by:

$$\frac{f_{B_\pm}}{f_C} = \sqrt{2n} = \frac{\sigma_{B_\pm}}{\sigma_C}, \tag{5.35}$$

which corresponds the the ratio of bunch lengths. The charm of using a momentum compaction function with the nature of Eq. 5.33 is the independence of the bunch length from the fixed point value, i.e. the value of α_{2n}, as long as the resulting buckets are within momentum acceptance. Therefore, the momentum acceptance of the RF bucket replacing C bucket can be conserved. However, to achieve a bunch length difference of relevance, this approach seems unpractical, as the momentum compaction function has to be controlled to a high order in δ. To achieve a factor of 10 in bunch length between $B_\pm$ and C bucket, $\alpha(\delta)$ has to be controlled up to the order α_{100}, which seems not feasible for storage ring operation. The resulting factor of $\sqrt{2}$ for a momentum compaction function of $\alpha(\delta) = \alpha_0 + \alpha_2\delta^2$ was verified experimentally at the MLS for the tune ratio as well as by streak camera measurements for the bunch length ratio.

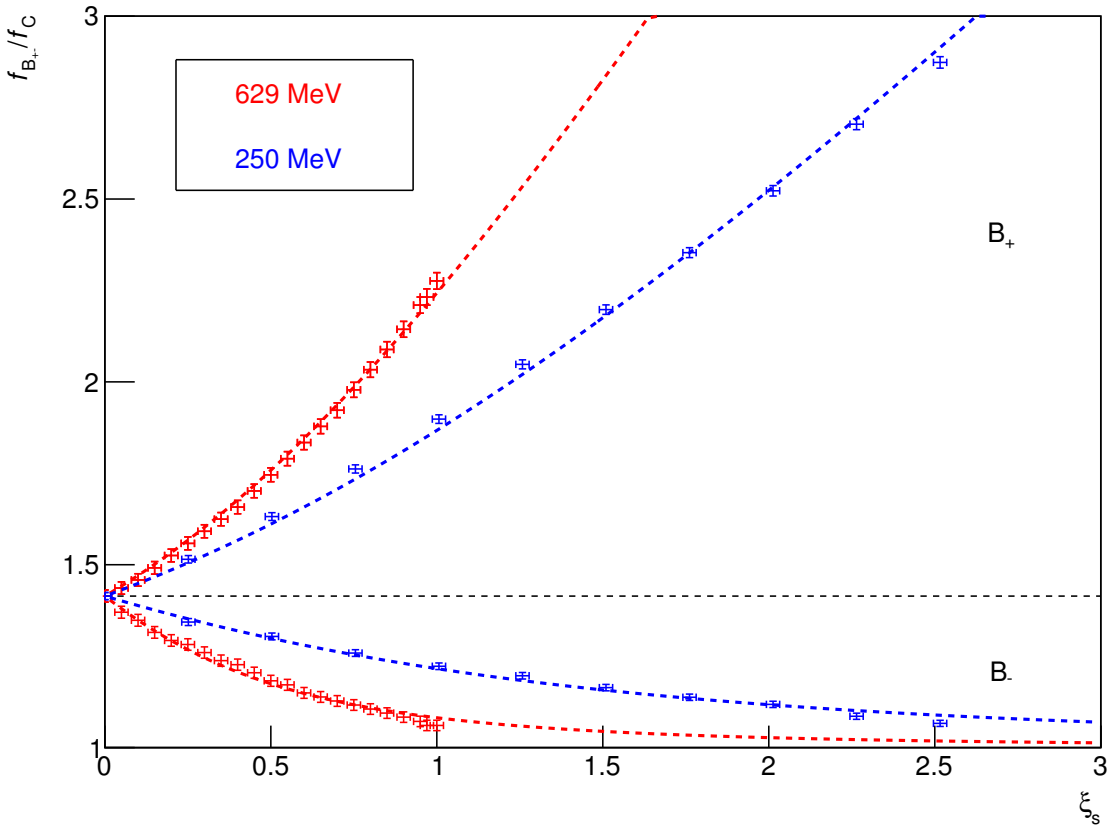

Figure 5.16: Simultaneous operation of multiple bunch lengths based on α-buckets. Synchrotron oscillation frequencies of buckets $B_\pm$ normalized to the synchrotron oscillation frequency of bucket C are shown while varying the longitudinal chromaticity ($\xi_s \propto \alpha_1$). The measurements were performed at 629 MeV (red) and 250 MeV (blue) with a maximized value of α_2.

Another approach, to simultaneously achieve multiple bunch lengths based on α-buckets, is to make use of asymmetric α-buckets by introducing a non-vanishing α_1 . However, in the simplest

case for a momentum compaction function of $\alpha(\delta) = \alpha_0 + \alpha_1\delta$, there is no effect on the bunch length as analytically follows:

$$\alpha(\delta) = \alpha_0 + \alpha_1\delta \qquad \rightarrow \qquad \frac{f_{s_B}}{f_{s_C}} = \frac{\sigma_{s_B}}{\sigma_{s_C}} = 1. \tag{5.36}$$

Therefore, at least a momentum compaction function of $\alpha(\delta) = \alpha_0 + \alpha_1\delta + \alpha_2\delta^2$ has to be considered, yielding a bunch length ratio given in Eq. 5.29 of:

$$\alpha(\delta) = \alpha_0 + \alpha_1\delta + \alpha_2\delta^2 \qquad \rightarrow \qquad \frac{f_{s_{B_\pm}}}{f_{s_C}} = \frac{\sigma_{s_{B_\pm}}}{\sigma_{s_C}} = \sqrt{2 + \frac{\alpha_1}{\alpha_0}\delta_{B_\pm}}. \tag{5.37}$$

Figure 5.16 shows simultaneous measurements of the synchrotron oscillation frequencies in RF-bucket and α-buckets. The experiment was conducted to demonstrate the feasibility of simultaneous operation multiple bunch lengths in a storage ring based on α-buckets. However, the direct measurement of the bunch length using a streak camera relies on the photon beam emitted by the electrons. To achieve a maximized bunch length ratio corresponding to Eqs. 5.30 and 5.31 it is an artificial limitation to require $D = 0$ and $D' = 0$ at the point of observation of the streak camera. However, this would be necessary to measure the bunch length without realigning the streak camera optics for every data point. Therefore, a measurement of the ratio of the synchrotron oscillation frequencies was chosen. The measurements were performed at 629 MeV (red) and 250 MeV (blue) with negative α_0 and the corresponding maximized value of $\alpha_2 > 0$ (see Eq. 4.11). The stored beam current per bucket was $I \approx 2\,\mathrm{mA}$. The longitudinal chromaticity and therefore α_1 were adjusted by sextupole magnets. The sign of α_1 was chosen such to store a long bunch in bucket B_+, whereas short bunches are stored in buckets B_- and C. The limiting effects are shrinking momentum acceptances of buckets B_- and C as well as the dispersive displacement of bucket B_+ leading to a limitation of the bucket momentum acceptance by the vacuum chamber walls. At 629 MeV the bunch length ratio was increased up to a factor of 2.2, whereas at 250 MeV even a factor of 2.7 was achieved. As all involved quantities of measurement are frequencies, the resulting uncertainties are quite small. The dashed lines show a fit of the relation given by Eq. 5.29. The resulting values for $\alpha_{0,1,2}$ are in agreement with the Compton backscattering method within the attached uncertainties. Therefore, a careful measurement of α-bucket tunes could be used to determine the values of $\alpha_{0,1,2}$ when higher orders are negligible.

5.3.4 Multi-Colored Insertion Device Radiation

The energetic separation of α-buckets in longitudinal phase space yields different spectral emission characteristics for the synchrotron radiation. For dipole magnet radiation the total emitted power changes by about 13% within operational limits for α-bucket operation at the MLS at the maximum electron energy of 629 MeV. In consequence, the synchronous phase shifts by a negligible value of lesser than 2×10^{-3} at maximum RF voltage. The spectral characteristics of dipole magnet radiation for α-buckets are similar to RF buckets as it is broad-band radiation, with the exception of a slightly shifted critical photon energy.

However, the main purpose of 3rd generation light sources is to deliver high-brilliance, narrow-

band radiation emitted by insertion devices. The spectral characteristics of α-buckets in insertion devices can become dominated by the corresponding fixed points in energy δ_{FP}. This was first observed at the NSLS and used to determine the energy separation of the α-buckets [74]. The coherence condition for undulator radiation in on-axis approximation is given by [28]:

$$\lambda_n = \frac{\lambda_u}{2\gamma^2 n}\left(1 + \frac{K^2}{2}\right), \tag{5.38}$$

where the wavelength of the n-th harmonic depends on undulator period length λ_u, electron energy and the undulator parameter K. Using the assumption of $D \approx 0$ and $D' \approx 0$ the coherence condition for electrons in α-buckets passing an insertion device at an energy fixed point δ_{FP} can be expressed by:

$$\frac{\lambda_{n\alpha}}{\lambda_n} = \frac{1}{\left(1 + \delta_{\mathrm{FP}}\right)^2}. \tag{5.39}$$

When the periodicity of the insertion device is large enough to generate harmonics with a spectral width smaller than the shift given in Eq. 5.39, it is possible to make use of two colored insertion device radiation. At the MLS it is possible to store beam in α-buckets with an energy deviation of about $\delta_{B_+} - \delta_{B_-} < 3\%$. Therefore the spectral separation for beam stored in the buckets $B_\pm$ at the fixed points $\delta_{\mathrm{FP}} = \pm 1.5\%$ accounts to:

$$\frac{\Delta\lambda}{\lambda} = \frac{\lambda\left(\delta_{\mathrm{FP}} = -1.5\%\right) - \lambda\left(\delta_{\mathrm{FP}} = +1.5\%\right)}{\lambda\left(\delta_{\mathrm{FP}} = 0\right)} \approx 6\%, \tag{5.40}$$

which can be resolved by the undulator U125 presently in operation at the MLS.

A measurement of the spectral radiant power of beam stored in α-buckets was performed to investigate the spectral characteristics as well as to cross check the values for the fixed point in energy. Therefore, beam was stored in α-buckets at a momentum compaction function of approximately $\alpha(\delta) \approx -0.0022 + 13.8\delta^2$. The experiment used a current of about $I = 40\,\mathrm{mA}$ in an homogeneous filling pattern, whereas the beam was evenly distributed in the buckets $B_\pm$. The standard low-α optics as depicted in Fig. 3.1 was modified to avoid effect originating from observation geometry. Therefore the dispersion function as well as its derivation in the insertion device section were adjusted to zero. The measured spectra are shown in Figure 5.17. Spectra of the 6th harmonic (left) and the 3rd harmonic (right) were measured using a grazing incidence monochromator and a photodiode (SPD-100UV) as detector. The RF bucket spectra are shown in red, whereas the α-bucket spectra are given in blue. The first observation is a symmetric splitting of the harmonics with respect to the RF-bucket situation, which is expected as $\alpha_1 \approx 0$. The observed asymmetry in the line shape of the harmonics is due to the nature of undulator radiation through finite apertures. The fixed point energy can be obtained by fitting the measured undulator spectra. Alternative techniques utilize the dispersive displacement at source point imaging systems, Compton backscattering or calculation based on $\alpha(\delta)$. A comparison of different methods to determine the value of the fixed point is shown in Table 5.1 shows.

Tunable spectral separation of multiple beams stored in α-buckets could be applied in ex-

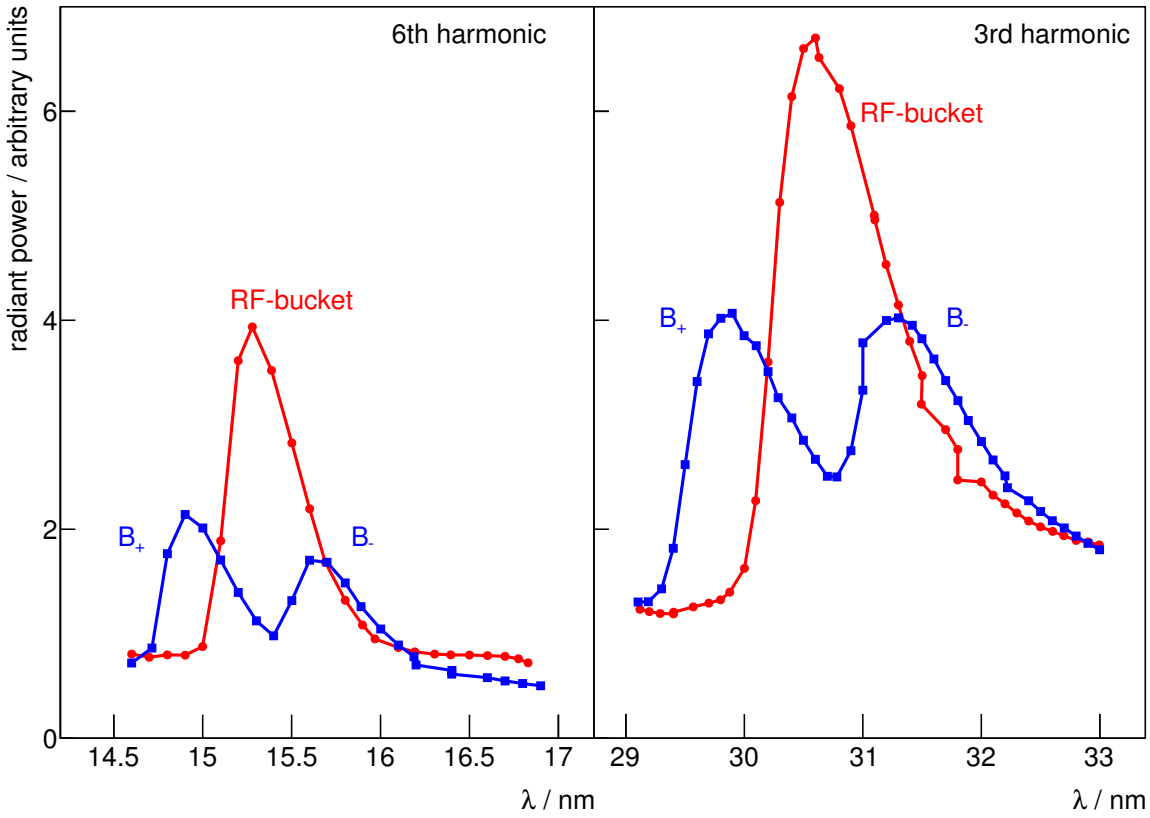

Figure 5.17: Measured splitting of undulator harmonics for α-bucket operation at the MLS. Spectra of 3rd (right) and 6th (left) harmonic measured at $E_0 = 629\,\mathrm{MeV}$, $\lambda_u = 125$ mm, $K = 1.54$, $\alpha_1 \approx 0$, $\alpha_2 \approx 13.8$ for $\alpha_0 > 0$ (red) and $\alpha_0 \approx -2.2 \times 10^{-3}$ (blue).

technique	$\delta_{\mathrm{FP}\,-}/\%$	$\delta_{\mathrm{FP}\,+}/\%$
3rd undulator harmonic	-1.22 ± 0.06	1.23 ± 0.05
6th undulator harmonic	-1.15 ± 0.04	1.20 ± 0.04
source point imaging	-1.20 ± 0.10	1.20 ± 0.10
calculation $\alpha(\delta) = 0$	-1.26 ± 0.05	1.26 ± 0.05

Table 5.1: Measurement results for δ_{FP} by different methods.

periments and be combined with geometric photon beam separation (section 5.2.4) or arrival time separation (section 5.3.5). On the other hand, the spectral separation of α-bucket photon beams could be negated by the use of tapered undulators in combination with a non-vanishing dispersion function inside the insertion device.

5.3.5 Tunable Longitudinal Delay between α-Buckets

Another application of α-buckets could be to translate the energy separation of α-buckets to an arrival time delay at a specific observation point. In this section, the presented scheme is intended to supply electron bunches with easily tunable time delay in the order of a few tens of picoseconds at the insertion device location opposite of the RF-cavity position at the MLS (see Fig. 1.2).

The position in phase, i.e. when particles arrive at the RF-cavity, is fixed by the equilibrium condition given in Eq. 2.22. However, it is possible to generate a separation in phase during one turn, as long as the synchronous phase is restored at the RF cavity. This can be achieved by introducing "asymmetric momentum compaction" to a storage ring. The idea is to generate a large partial momentum compaction factor (c.f. R_{56}) in the first half of the ring, which is then compensated by a large partial momentum compaction factor with opposite sign in the second half. In this way a stable shearing of the longitudinal phase space can be introduced at a specific observation point. In a double bend lattice this would mean giving up on dispersion free straights, which is not necessarily the case for a triple bend lattice.

Using the individual quadrupole power supplies of the MLS, there are enough degrees of freedom to deliver the following properties:

- dispersion free ID straight ($D = 0, D' = 0$),
- tunable partial momentum compaction factor in the first half of the ring α^{I},
- tunable partial momentum compaction factor in the second half of the ring α^{II},
- tunable momentum compaction factor $\alpha_0 = (\alpha^{\mathrm{I}} + \alpha^{\mathrm{II}})/2$.

However, in larger rings consisting of many segments, the scheme could be achieved by relaxing the dispersion condition in segments without (sensitive) beamlines. In the special case of the observation point being at the opposite of the RF cavity, the generated delay between the $B_{\pm}$ buckets can be written as:

$$\Delta T \approx \frac{L_0}{2\beta c}\alpha^{\mathrm{I}}\left(\delta_{B_+} - \delta_{B_-}\right), \tag{5.41}$$

and is for the MLS in the order of 20 ps. Figure 5.18(b) shows first experimental evidence, that the proposed operation scheme is applicable. A longitudinal bunch profile is shown, measured by a streak camera in the insertion device section of the MLS. To avoid impact of the photon beam path from the point of observation to the streak camera, the optical functions D and D' were carefully adjusted to zero in the insertion device section, i.e. the synchrotron radiation emitted by the $B_{\pm}$-buckets originates from the same source point and is directed in the same direction.

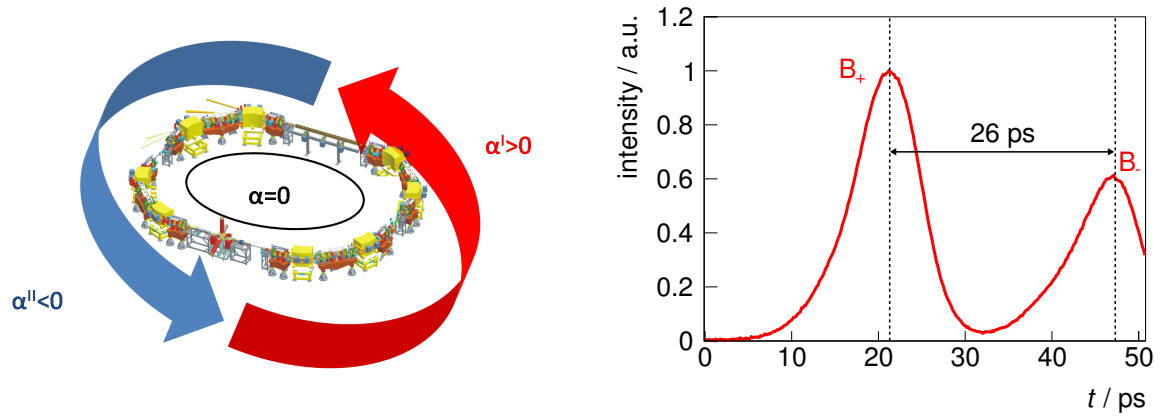

(a) delayed α-bucket generation

(b) Measured delay of α-buckets at the MLS

Figure 5.18: Generation principle of an arrival time delay of the α-buckets $B_{\pm}$ in the insertion device section of the MLS (left). Measured delay of 26 ps at the insertion device beamline using a streak camera.

The temporal separation of the photon pulses emitted by the α-buckets $B_{\pm}$ was increased up to 26 ps clearly resolved by streak camera measurements. An attractive property of this mode of operation is the ability to adjust the partial momentum compaction factor in the first half of the storage ring α_I, while keeping "global" momentum compaction α_0 fixed. Therefore, longitudinal separation can be adjusted smoothly back and forth, whereas the bunch length is kept constant. At the time of writing this thesis further studies of this operation mode are ongoing.

6 Coherent Synchrotron Radiation at the MLS

Coherent synchrotron radiation is known since the early years of synchrotron radiation [86]. However, in storage rings – as a source of instability – it was condemned to suppression for half a century [87]. In the last decade, several electron storage ring based light sources adopted the concept of low-α operation to generate coherent synchrotron radiation in the THz regime such as [7–10, 23, 41–46]. The design of the MLS was optimized for the generation of coherent synchrotron radiation [18]. At the time of writing this thesis, the MLS is regularly operated in low-α user operation [23], whereas stable and bursting CSR available. Although nonlinear momentum compaction is the main subject of this thesis, the generation of coherent synchrotron radiation is the main motivation to operate the MLS with short electron bunches. This chapter will give an overview of selected CSR measurements at the MLS performed during completion of this thesis [88]. Focus will be put on a current-dependent instability driven by the emission of CSR – "bursting" – potentially limiting the performance of short bunches in electron storage rings. Measurements conducted at the MLS and BESSY II will be shown.

6.1 Generation of Coherent Synchrotron Radiation

Comprehensive introductions to the field of coherent synchrotron radiation are given in [46, 89]. The emission of coherent synchrotron radiation by relativistic charged particles is a collective effect arising at wavelengths large compared to the longitudinal extension of the bunch or its substructures. Its relevance can be understood by investigating the superimposed radiation fields of multiple particles. As the radiation power is proportional to the square of the electric field $\mathcal{E}$, the scaling of the radiation power with particle number N_e can be expressed by [27]:

$$P(\lambda) \propto \sum_{j,l}^{N_e} \mathcal{E}_j \mathcal{E}_l^* \propto \sum_{j,l}^{N_e} e^{\frac{2\pi}{\lambda} i(ct+z_j)} e^{-\frac{2\pi}{\lambda} i(ct+z_l)} = N_e + \sum_{j \neq l}^{N_e} e^{\frac{2\pi}{\lambda} i(z_j - z_l)}, \tag{6.1}$$

where λ corresponds to the wavelength of interest and $z_{j,l}$ is the longitudinal displacement from the bunch center of the j-th correspondingly l-th electron. For simplicity, the effect of transverse particle distribution was neglected. For wavelengths small compared to the bunch length ($\lambda < z_{j,l}$), the right term in Eq. 6.1 vanishes to zero assuming equilibrium distribution, which is characteristic for incoherent synchrotron radiation: $P_{\text{incoherent}} \propto N_e$. In the limit of wavelengths that are large compared to the bunch length ($\lambda \gg z_{j,l}$), particles of a bunch emit radiation in phase like a quasi-particle with an accordingly higher charge. Therefore, the right term in Eq. 6.1 contributes $N_e\,(N_e - 1)$ adding up $P_{\text{coherent}} \propto {N_e}^2$ for coherent synchrotron radiation.

Commonly, electron storage rings are operated with bunch lengths in the order of a few tens

of picoseconds. In fact, most light sources deliberately increase the bunch length applying techniques such as Landau cavities or longitudinal excitation to achieve longer Touschek lifetimes. For long bunches, the coherent part of the emitted spectrum is suppressed due to the vacuum chamber. The cut-off wavelength for radiation suppression in the parallel plate approximation is given by [90]:

$$\lambda_{\text{cutoff}} = 2d\sqrt{d/\rho}, \tag{6.2}$$

where d is the the full chamber height and ρ the local bending radius. The chamber cutoff at the MLS ($d = 42\,\text{mm}$, $\rho = 1.528\,\text{m}$) corresponds to $\lambda_{\text{cutoff MLS}} \approx 14\,\text{mm}$, which is quite large due to the uncommonly small bending radius.

The spectral radiation power regarding coherent synchrotron radiation can be calculated by [27]:

$$P_{\text{coherent}}(\lambda) = \underbrace{P_{1e}(\lambda)N_e}_{P_{\text{incoherent}}} \left[1 + \underbrace{(N_e - 1)\exp\left(-2\pi^2\left(\frac{\sigma}{\lambda}\right)^2\right)}_{\text{CSR gain}} \right], \tag{6.3}$$

where a Gaussian particle distribution of length σ is assumed. $P_{1e}(\lambda)$ corresponds to the spectral radiation power emitted by a single electron.

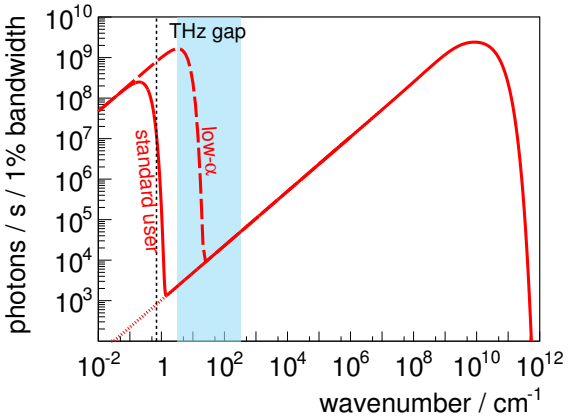

Figure 6.1: Spectrally resolved photon flux at the EUV beamline (cf. Fig. 1.1(a)) including coherent synchrotron radiation for 1 µA single bunch current. Standard user operation (solid red), low-α operation (dashed red) as well as pure incoherent (dotted red) are shown. The shielding cutoff due to vacuum chamber dimensions is marked by the dashed black line. The "THz gap" is marked by the blue area.

A calculation of the spectrally resolved photon flux at the EUV beamline of the MLS is shown in Figure 6.1 (cf. Fig. 1.1(a)) including coherent synchrotron radiation. The calculation was performed for the standard user mode (solid) as well as for low-α operation (dashed) following

Eq. 6.3. A single bunch with a bunch current of $I_{SB} = 1\,\mu A$ was assumed corresponding to a bunch charge of $10^6 e^-$. The dotted line indicates purely incoherent synchrotron radiation. The vacuum chamber cutoff given in Eq. 6.2 is indicated by a vertical dashed line. In standard user operation, only a small fraction of the emitted radiation is coherent synchrotron radiation, due to the long bunch length. However, even this small part is still detectable by sensitive detectors at the THz beamline. In low-α operation, the spectrum of coherent synchrotron radiation is beyond the chamber cutoff extending deep into the "THz gap" indicated by the blue area [91]. The largest average power of the coherent synchrotron radiation measured at the THz beamline of the MLS was $P_{max} \approx 60\,mW$ corresponding to a peak power in the order of a few ten W [92].

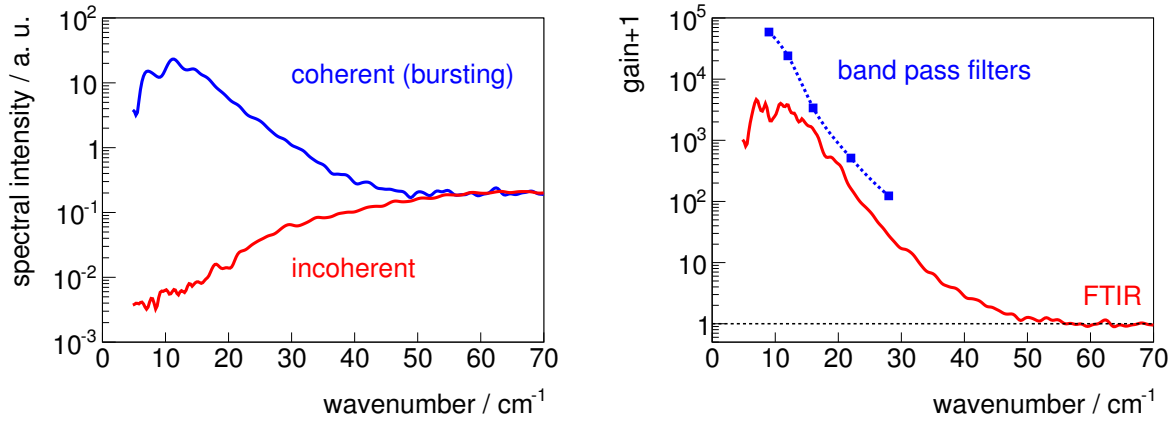

(a) FTIR spectra in standard user and low-α

(b) CSR gain (bursting)

Figure 6.2: FIR spectra at the THz beamline of the MLS (a) in standard user operation (red) and low-α operation (blue) measured at a ring current of 100 mA (bursting) using an FTIR spectrometer and a DTGS detector. CSR gain measured using the FTIR/DTGS setup (red) as well as band pass filters in combination with a Ge bolometer (blue).

Figure 6.2(a) shows a measurements of FIR spectra at the THz beamline in standard user operation (red) and low-α user operation (blue). The measurements were conducted at the THz beamline of the MLS using a Vertex 80v Fourier transform spectrometer equipped with a DTGS detector [93]. A ring current of about 100 mA with a homogeneous filling pattern was used. The spectral gain extends up to about $50\,cm^{-1}$. The lower edge of the coherent spectrum given in Fig. 6.2(a) is dominated by a 50 µm Mylar beam splitter applied in the FTIR spectrometer. Using different detectors respectively beam splitter setups, the THz group at the MLS was able to observe radiation down to about $1\,cm^{-1}$, which is in the regime of the vacuum chamber cutoff given in Eq. 6.2. In a joint experiment with ANKA, it was possible to observe radiation power at even longer wavelengths in the microwave range similar to [94]. The ratio of both spectra is visualized in Fig. 6.2(b), however, the measured gain at long wavelengths was smaller than expected. Further investigation yielded two main reasons. On the one hand, the spectrum measured in standard user mode contained coherent contributions, i.e. the incoherent

radiation power was overestimated. Therefore, the bunch length was continuously increased by reducing RF cavity voltage to the point, where measured THz power became independent of the applied RF cavity voltage. On the other hand, the detector used for the measurements in Fig. 6.2(a) turned out to suffer from severe saturation effects, i.e. the coherent radiation power was underestimated. To cover for the saturation effect, wire grid polarizers in combination with a highly sensitive Ge bolometer were set up. Polarizers were used as a measure of manipulating the THz power in a predictable manner, whereas a set of band pass filters was used for spectral resolution. The resulting corrected gain is shown in Fig. 6.2(b) as blue data yielding a factor of 100 higher gain at long wavelengths. In the limit of long wavelengths, an overall CSR gain in the order of $10^5 \ldots 10^6$ was observed similar to other light sources [95].

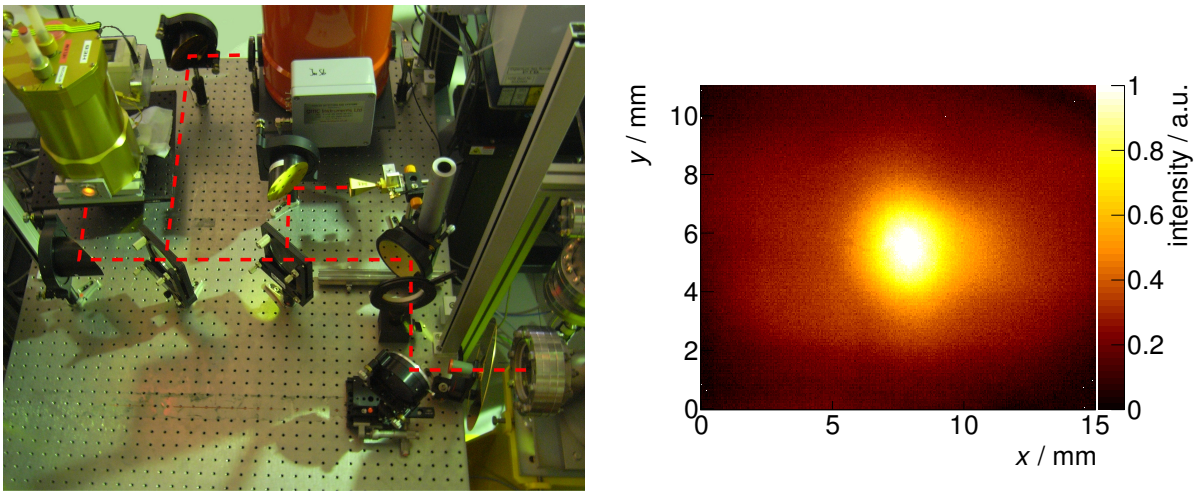

(a) detector development site

(b) spatial extension of the THz focus

Figure 6.3: Site for detector development at the THz beamline of the MLS (a), set up for simultaneous measurement using different detector types. THz focus measured at the THz beamline with an rms extension of $\sigma_x \approx 1.9\,\mathrm{mm}$ and $\sigma_y \approx 2.0\,\mathrm{mm}$.

A selected detector setup at the THz beamline is shown in Fig. 6.3(a). The exit of the beamline can be seen in the bottom right corner. In the given example, THz power is distributed to three different detectors using wire grids: a hot electron bolometer (golden dewar, ANKA), an InSb hot electron bolometer (red dewar, MLS) and a Schottky diode (DIAMOND).

The size of the THz focus spot at the detector development site is depicted in Fig. 6.3(b) and shows a measured rms beam width of $\sigma_x \approx 1.9\,\mathrm{mm}$ and $\sigma_y \approx 2.0\,\mathrm{mm}$. The spatial distribution of THz power was measured in focus using an IR camera with sensitivity in the THz regime. Polyethylene filters were used to block intensity in the NIR and VIS regime.

6.2 Bunch Length Measurement

The electron bunch length is a crucial parameter when performing fast dynamics experiments or using coherent synchrotron radiation. The zero-current bunch length can be calculated in

harmonic approximation as given in Eq. 2.44. However, various effects such as potential well distortion, excitation due to RF noise, interaction with ring impedances or the emission of coherent synchrotron radiation (see next section) may lead to a distorted equilibrium or non-equilibrium particle distribution. Most of these effects, arise at high bunch currents, therefore, Eq.2.44 may only be applied for small currents. However, an experimental characterization of the current dependence of the bunch length is essential for the users of short bunches. Therefore, measurements of the current dependent bunch length were performed in different operation modes of the MLS. A streak camera was used to measure the bunch length [83]. Unfortunately, the spectral transmission characteristics of the THz beamline in the VIS/UV range are unfavourable. Therefore, the IR beamline was chosen as point of observation, although a significant bunch lengthening at this beamline is expected (see section 3.6). Figure 6.4 shows the measurement results in a scaled

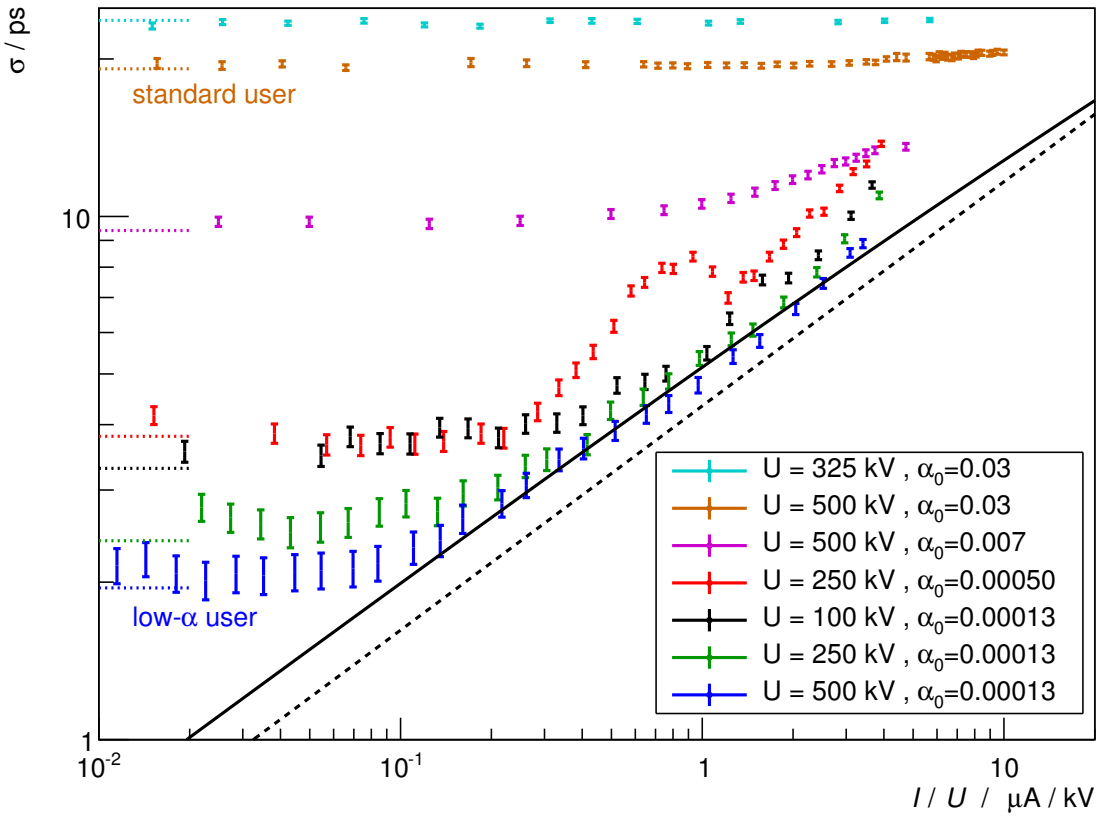

Figure 6.4: Measurement of the bunch length as a function of current in single bunch operation. Data was obtained using a streak camera at the IR beamline of the MLS for different combinations of momentum compaction factor and RF cavity voltage. Calculated bursting thresholds (solid and dashed line) are given following Eqs. 6.4 – see text. The dotted lines on the left side indicate the calculated zero-current bunch length corresponding to the color code.

plot. Measurements were performed for different combinations of momentum compaction factor and RF cavity voltage in single bunch operation. Data was obtained starting from high single bunch currents successively decreasing the current using scrapers. Of particular interest are the bunch lengths in standard user mode (orange) and in low-α user mode (blue). It should be noted, that the bunch lengthening at large currents occur due to an instability. The measured bunch length corresponds to the average bunch length. Solid and dashed lines correspond to different theoretical thresholds for bunch lengthening (see Eq. 6.4), which will be discussed in the next section. Dotted lines on the left side correspond to expected zero-current bunch length, where bunch lengthening due to RF noise as well as emittance induced lengthening due to the point of observation was regarded. The measurement uncertainty is dominated by the resolution limitation of the streak camera which is about 2 ps. However, in the zero-current limit, bunch length measurements agree well with predictions within uncertainties of the involved quantities. For high bunch currents, a bunch lengthening is observed, which agrees well with theory. A particular distinctive feature can be observed for the data taken at $\alpha_0 = 5 \times 10^{-4}$ and $U = 250\,\mathrm{kV}$ (red). At a value of $I/U \approx 1.4\,\mu\mathrm{A/kV}$ the bunch length shows anomalous behaviour with bunch current, i.e. it decreases compared to smaller bunch currents. The corresponding bunch length at the minimum of the anomaly is $\sigma_* = (6.8 \pm 0.8)\,\mathrm{ps}$. This feature is due to interaction of the bunch with the vacuum chamber walls and was already observed at BESSY I [96]. However, it could only be observed for specific combinations of bunch length, bunch current and applied RF cavity voltage. The effect will be dealt in more detail in the next section.

The measurement given in Fig. 6.4 is now used as a reference measurement by low-α users at the MLS.

6.3 Microwave Instability Thresholds

The bunch current that is stably storable in short bunches is limited by various storage ring parameters. In the limit of small currents, coherent synchrotron radiation is emitted in a stable manner, i.e. the THz pulse detected from a single bunch has the same shape and intensity every turn. However, when increasing the bunch current, fluctuations in the THz pulse – "bursting" – will arise at some point. Therefore, when comparing THz pulses from different turns or over longer time scales typically given by radiation damping time or synchrotron oscillation frequency, users will see an unstable source. The transition from stable CSR emission to bursting CSR was first observed at BESSY II [10]. Introductions in theory of instability thresholds for short bunches with focus on CSR impedance can be found in [97–99].

The relation between the current threshold I_{th} of the microwave instability and bunch length is given by [100]:

$$\sigma^{7/3} = \frac{c^2 Z_0 \rho^{1/3} h}{8\pi^2 \xi^{\mathrm{th}} f_{\mathrm{rf}}^2} \frac{I_{\mathrm{th}}}{U \cos(\varphi_s)}, \tag{6.4}$$

where $Z_0 \approx 377\,\Omega$ is the free space impedance and ξ^{th} a scaled threshold current, which was

extracted from [98, 100]:

$$\text{bunched beam theory:} \qquad \xi^{\text{th}} = \xi^{\text{th}}(\chi) \approx 0.5 + 0.34\chi - 0.38 \exp\left(-\frac{(\chi - 0.25)^2}{2 \cdot 0.02^2}\right), \tag{6.5}$$

with the shielding parameter $\chi = \sigma\rho^{1/2}/d^{3/2}$. The right term in Eq. 6.5 was modelled according to the results given in [98, 100] and rescaled for MLS machine parameters in low-α user operation. The Gaussian modification generates a local minimum of the threshold current at $\chi = 0.25$ corresponding to a bunch length of:

$$\sigma^*_{\text{MLS}} = 1.74\,\text{mm} \approx 5.8\,\text{ps}, \tag{6.6}$$

$$\sigma^*_{\text{BESSY II}} = 0.79\,\text{mm} \approx 2.6\,\text{ps}. \tag{6.7}$$

It should be noted that the distinctive feature visible in the red result from Fig. 6.4 is within feasible range of σ^*_{MLS}. The analytical result in the scope of coasting beam theory yields:

$$\text{coasting beam theory:} \qquad \xi^{\text{th}} = 7.456 \cdot 3^{1/3}/4\pi \approx 0.856. \tag{6.8}$$

The MLS is ideally suited to measure the bursting threshold and in particular its scaling as it covers a large tuning range in terms of momentum compaction factor, overvoltage factor and bunch length. Especially interesting is the threshold for short bunches in the regime of $\sigma = 1\,\text{ps}$. In addition, the impact of the vacuum chamber dimensions at short bunch lengths through Eq. 6.4 lies in a well investigable range of machine parameters.

To measure the instability threshold a fast detector in the THz range is desirable as the emission characteristics of coherent synchrotron radiation are very sensitive to changes in the bunch profile. At the MLS there is an InSb hot electron bolometer available (red dewar in Fig. 6.3(a)). Its spectral sensitivity extends up to $50\,\text{cm}^{-1}$. The detector has a time constant of about $\tau \approx 1\,\mu\text{s}$ and is therefore able to resolve frequencies up to the MHz regime. Therefore, the detector can neither resolve the bunch spacing (2 ns) nor the revolution time (160 ns), i.e. the detector will average over many bunches respectively several turns. However, typical bursting frequencies are in the order of the synchrotron oscillation frequency f_s or its higher harmonics, which are in the range of smaller than 200 kHz for low-α operation at the MLS. As processes in storage rings are typically periodic processes, using a spectrum analyzer supplies an additional boost in sensitivity. However, the limited speed of the detector leads to the problem of averaging over all 80 bunches with potentially different bunch currents. Therefore, all threshold measurements shown in this work were performed in single bunch operation.

Figure 6.5(a) shows three selected measurements to investigate the time structure of the THz radiation using the InSb detector. The first measurement (black) was performed below the instability threshold, i.e. in the regime of stable CSR emission. Therefore, no fluctuations are detected as the detector averages over the stable THz pulses, the measured signal corresponds to the noise floor. However, a strong signal was observed when introducing a mechanical chopper in the beam path, i.e. there is a large but stable THz radiation power. The second measurement (red) was performed at a bunch current slightly above the threshold, indicated by several sharp lines. Therefore, the THz radiation is modulated by bursts of coherent synchrotron radiation

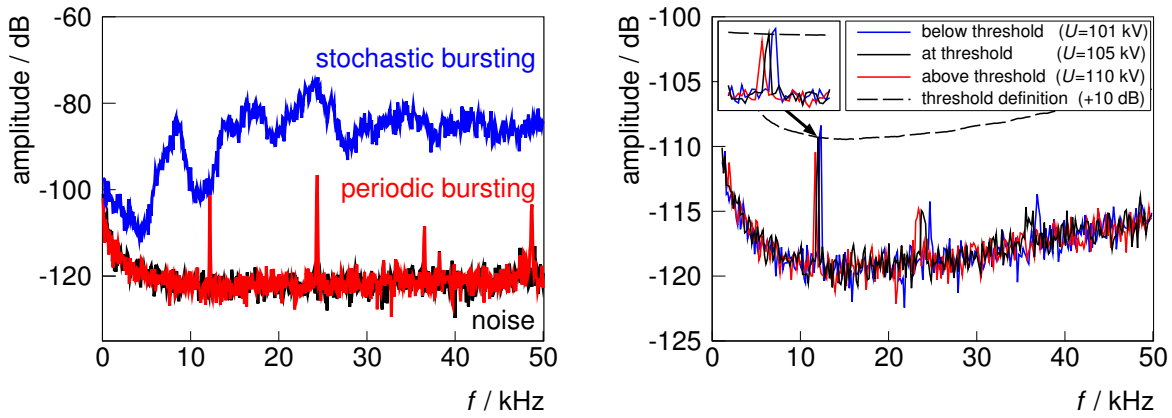

(a) THz bursting regimes

(b) definition of the applied threshold condition

Figure 6.5: Temporal fluctuations of the THz power emitted by a single bunch are shown in frequency domain measured by an InSb bolometer at the THz beamline of the MLS. Three different regimes can be identified (a): noise level (black), periodic bursting (red) and stochastic bursting (blue). The bursting threshold condition applied throughout this work "noise + 10 dB" is shown as a dashed black line in (b), whereas spectra below (red), at (black) and above (blue) the threshold condition are given.

at distinctive frequencies – "periodic bursting". The third measurement (blue) corresponds to operation far above the threshold. Although the spectrum still shows emphasized frequencies corresponding to the synchrotron oscillation frequency and its harmonics, it is characterized by a considerable rise of the signal in a broad spectral range, i.e. the nature of the THz radiation pulses in the state has a much more random nature – "stochastic bursting".

The question of a reliable criterion arises when measuring a bursting instability threshold as crossing the threshold usually does not lead to an ever self-amplifying process or beam loss. In fact, at the threshold small micro structures may emerge visible as fluctuations in the THz power [101]. However, from the phase space point of view at, there are just minor density modulations hardy visible as a measurable increase of energy spread or bunch lengthening . When applying the THz detection technique as described above, the threshold measurement criterion will necessarily depend on the signal-to-noise ratio as well as the dynamic range of the detector. A detection criterion of 10 dB above the (arbitrary) noise floor was chosen for the measurements of the bursting threshold in this work. This criterion is depicted in Fig. 6.5(b) together with three selected measurements below (red), roughly at (black) and above the threshold.

The bursting threshold may be measured by different approaches such as:

- variation of bunch current,
- variation of bunch length though RF-voltage,
- variation of bunch length though momentum compaction.

Although a bunch length variation can be provided by RF-voltage as well as momentum compaction, the RF-voltage is the favourable quantity of variation as its change can be easily measured and there is no hysteresis involved. Figure 6.6 shows the stability of the THz power measured over a large variation range of either bunch current (a) or RF voltage (b). The bunch current was measured using a PCTs in the mA-regime scaled down to smaller currents using photo diodes, which is a well established technique used by the PTB. Figure 6.6(a) shows the

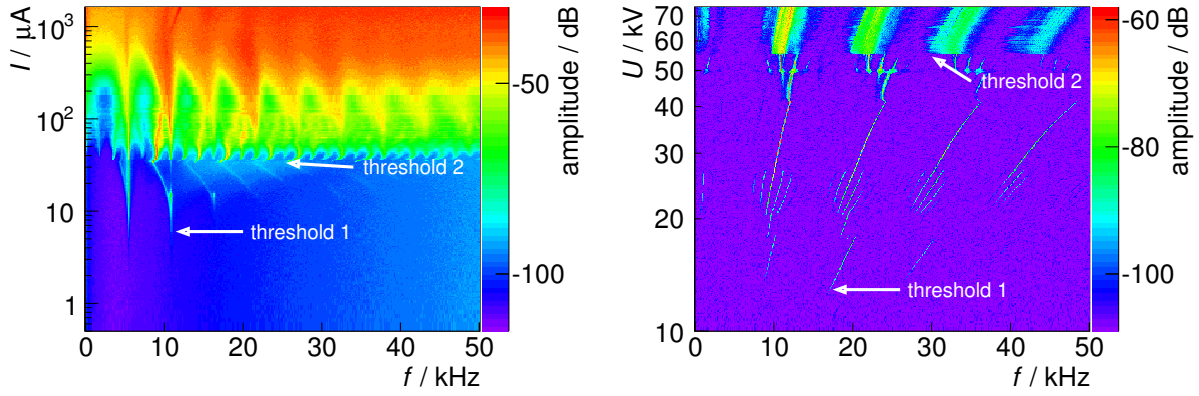

(a) threshold current scan

(b) threshold voltage scan

Figure 6.6: Temporal fluctuations of the THz power emitted by a single bunch are shown in the frequency domain measured by an InSb bolometer at the THz beamline of the MLS. A selected current scan at $\alpha_0 = 1.3 \times 10^{-4}$ and $U = 330\,\mathrm{kV}$ (a) as well as a selected RF-cavity voltage scan at $\alpha_0 = 5.0 \times 10^{-4}$ and $I = 300\,\mu\mathrm{A}$ (b) are given.

THz power in frequency domain for a bunch current variation of $I = 1600\,\mu\mathrm{A} \ldots 0.5\,\mu\mathrm{A}$. The storage ring was set up with $\alpha_0 = 1.3 \times 10^{-4}$ and $U = 330\,\mathrm{kV}$ corresponding to a zero-current bunch length of $\sigma_0 = 1.5\,\mathrm{ps}$. The bunch current was reduced by applying a scraper, however, this was done between measurements, i.e. the scraper was fully pulled out before taking data. Bursting starts at a bunch current $5\,\mu\mathrm{A}$ marked by "threshold 1", whereas a second distinctive threshold can be observed at $35\,\mu\mathrm{A}$ marked by "threshold 2". Figure 6.6(b) shows the THz power in frequency domain for an RF voltage variation from $U = 10\,\mathrm{kV}$ to $U = 80\,\mathrm{kV}$. The applied momentum compaction factor was $\alpha_0 = 5.0 \times 10^{-4}$ with a bunch current of $I \approx 300\,\mu\mathrm{A}$. Bursting starts at an RF cavity voltage of $13\,\mathrm{kV}$ (threshold 1) respectively $55\,\mathrm{kV}$ (threshold 2). As a cross check, the same measurement was conducted for a decreasing RF-voltage yielding similar results, i.e. there was no measurable difference for the transition from stable to bursting or vice versa. As the MLS is a ramped synchrotron, the corresponding experiment was not possible for current variation.

The data sets shown in Figs. 6.6(a) and 6.6(b) each yield one value for the bursting threshold, which is characterized by the triple (I, U, α_0). Measuring the bursting threshold like this is a time consuming process. The flexibility of the MLS control system allowed full automatization of the measurement process yielding a high reproducibility as well as higher resolution. The

applied algorithm can be sketched as:

1. set $U_{\min}$,
2. a) record Fourier transform data of the THz signal,
   b) record other relevant beam parameters ($I, f_s \ldots$),
   c) increase U by one increment towards $U_{\max}$,
3. use automatic scraping procedure to reduce bunch current e.g. by 5%,
4. repeat.

Offline data analysis yields one measurement of the bursting threshold per inner loop.

Figures 6.7 and 6.8 show a collection of selected bursting threshold measurements performed in various operation modes of the MLS. Table 6.1 shows a legend to identify different momentum

marker	●	●	●	●	●
$\alpha_0/10^{-6}$	157 ± 9	138 ± 8	155 ± 9	152 ± 8	111 ± 6
marker	■	■	■	■	■
$\alpha_0/10^{-6}$	507 ± 33	457 ± 26	481 ± 26	481 ± 26	473 ± 28
marker	★	★	▲	▼	▼
$\alpha_0/10^{-6}$	-490 ± 27	-473 ± 25	1330 ± 150	1910 ± 240	1880 ± 210

Table 6.1: Legend plot for the interpretation of bursting threshold measurements performed at the MLS.

compaction factors. A direct illustration of the measured threshold current as a function of RF-voltage for different momentum compaction factors is depicted in Fig. 6.7.

The scattering of different measurement sets is with respect to the corresponding value of α_0 gives an impression of the measurement reproducibility. Measurement uncertainties are not included in the plot as they are completely dominated by the applied definition of bursting threshold. Typical uncertainties of the measurement quantities are $\Delta I/I \approx 10^{-3}$, $\Delta U/U \approx 10^{-2}$ and $\Delta\alpha_0/\alpha_0 \approx 8\%$. The data is characterized by a distinctive feature at certain ratio of bunch current and RF voltage of $I/U \approx 1.4\,\mu\text{A/kV}$. This ratio is indicated by a dashed line and is at the same value as the anomaly observed for the bunch length measurement in Fig. 6.4.

Figure 6.8 shows a scaled visualization of the same data to account for theoretical threshold given in Eq. 6.4. Theoretical thresholds are indicated by a dashed line (coasting beam) and a solid line (bunched beam). The knowledge of RF-voltage and momentum compaction factor α_0 was used to calculate the zero-current bunch length as given in Eq. 2.33. The figure shows $\sigma_0(U, \alpha_0, E)$ as a of function I/U. The yellow area marks a parameter range obtained through particle tracking for the MLS, which was extracted from [102, 103].

In the limit of long bunches, measurement results agree well with theory. However, at a bunch length of $\sigma_0 = \sigma^*_{\text{MLS}} = 5.8\,\text{ps}$, a characteristic anomaly is observed peaking at a bunch

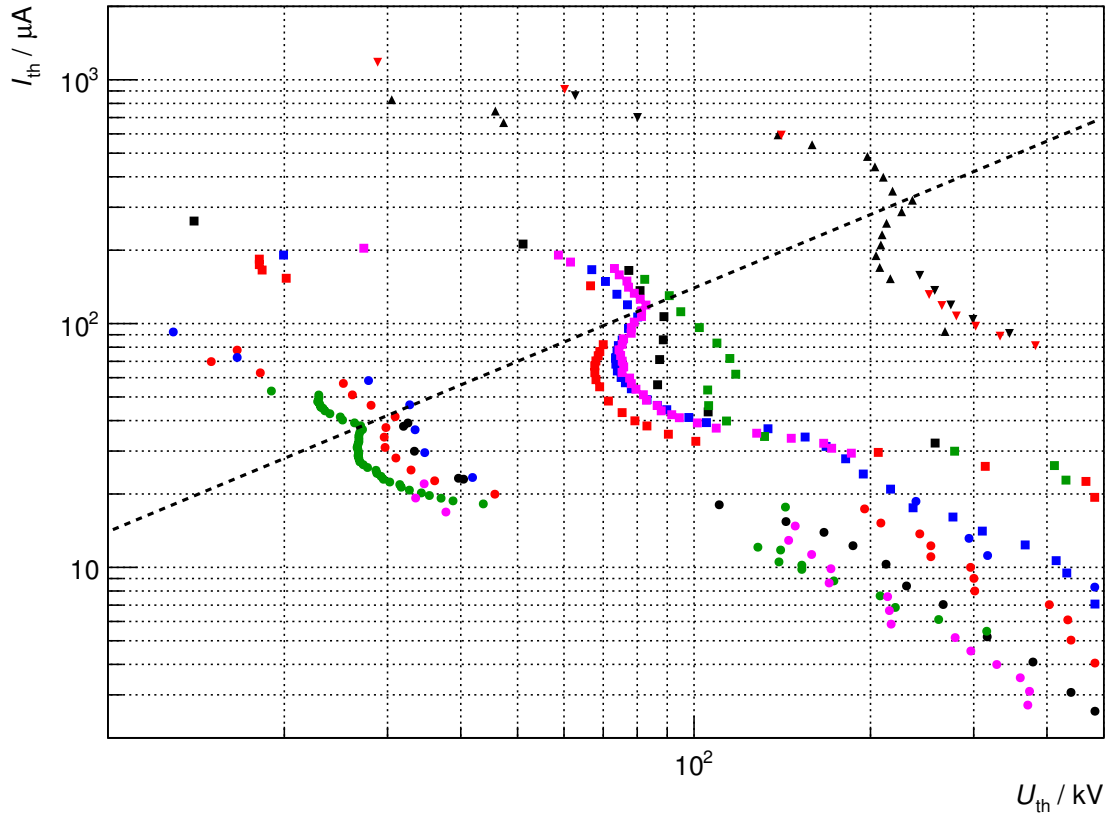

Figure 6.7: Measurement of THz-bursting thresholds for a single bunch stored at the MLS operated at positive momentum compaction. Different markers indicate different momentum compaction factors, whereas different colors indicate measurement sets corresponding to Tab. 6.1. The relation $I_{\mathrm{th}}/U_{\mathrm{th}} = 1.4\,\mu\mathrm{A/kV}$ is marked by a dashed line.

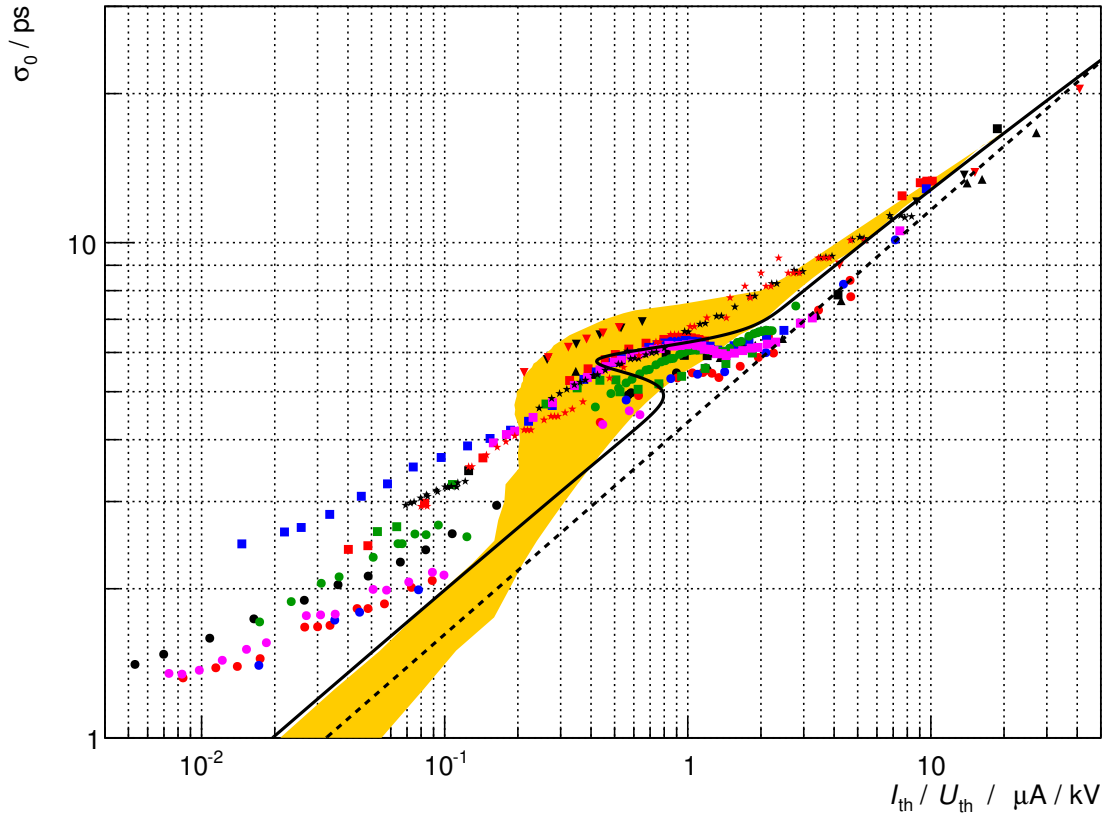

Figure 6.8: Measurement of the THz-bursting threshold at the MLS for different α_0-values, whereas different colors indicate measurements sets corresponding to Tab. 6.1. The bunch length σ_0 was calculated from the RF cavity voltage. Calculated bursting thresholds (dashed and solid line) are given following Eq. 6.4. The yellow area corresponds to thresholds obtained by particle tracking – see text.

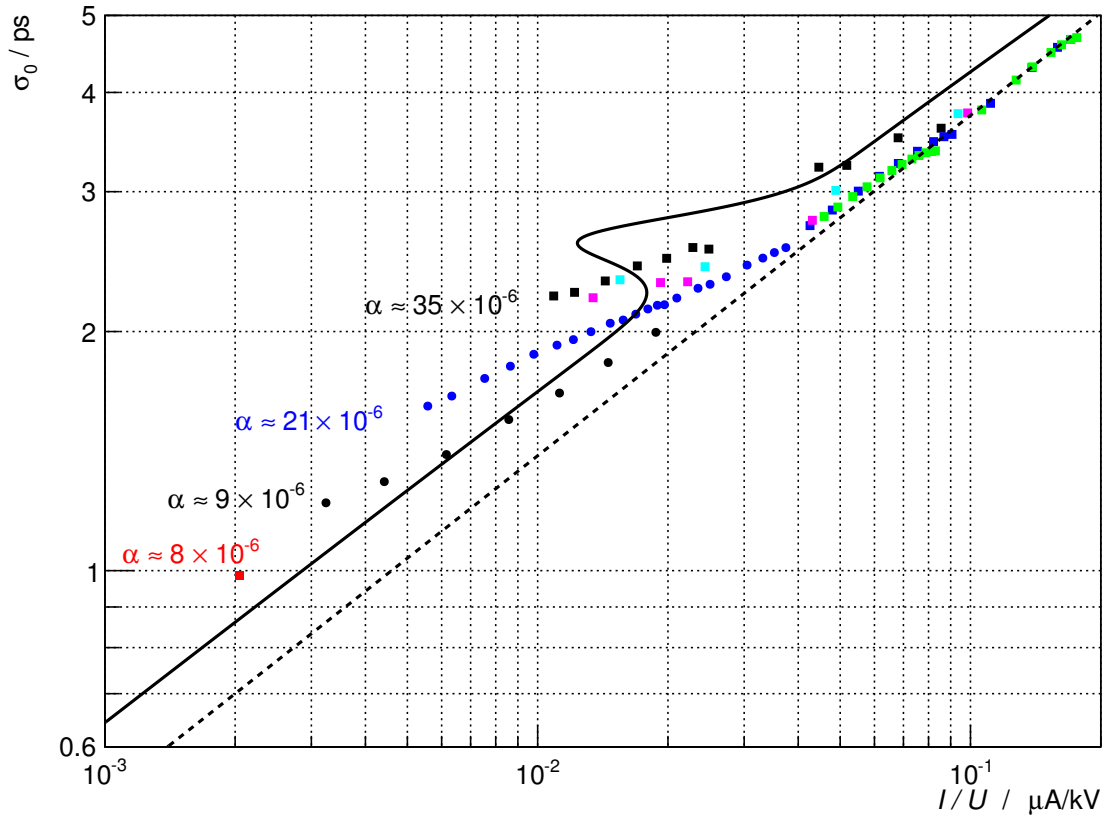

Figure 6.9: Measurement of the THz-bursting threshold at the BESSY II storage ring for different α_0-values. The bunch length σ_0 was calculated from the applied RF cavity voltage. Calculated bursting thresholds (dashed and solid line) are given following Eq. 6.4 – see text.

current to RF voltage ratio of $I/U \approx 1.4\,\mu A/kV$. This feature may be assigned to a weak instability occurring at a certain bunch length as proposed in [98, 100]. The anomaly is not observed at negative momentum compaction factors. For bunch lengths smaller than σ^*_{MLS} the measurement results are deviating significantly from the scaling law. The deviation is larger for higher momentum compaction factors.

Similar measurements of the bursting threshold through RF-voltage variation were performed at the BESSY II storage ring. The results are shown in Fig. 6.9 in a scaled view including theoretical predictions. For large bunch lengths, measurement agrees well with coasting beam theory. The distinct anomaly from the MLS results, is not visible within the BESSY II thresholds. However, similar to the MLS, at $\sigma^*_{\mathrm{BESSY\ II}}$ the measurement sets seem to deviate from the scaling law, showing again higher deviation for higher momentum compaction factors.

This observation may be of relevance for future storage ring projects targeting the 1 ps regime by applying large voltage gradients at comparatively large momentum compaction factors such as BESSY$^{\mathrm{VSR}}$. However, the definition of bursting threshold plays a key role in this matter, e.g. “threshold 1” or “threshold 2”. Eventually, this will be a question for the users of short synchrotron radiation pulses. For unstable emission, users of short incoherent X-ray pulses are affected by an average bunch lengthening as well as an increase in energy spread In particular, this affects users of coherent synchrotron radiation and to what degree fluctuations may be bearable.

7 Conclusion

The MLS is regularly operated in short bunch operation through reduction of the momentum compaction factor. Therefore, the use of additional sextupole and octupole magnets is mandatory enabling control of higher order beam optics. Throughout this thesis the low-α operation mode at the MLS was investigated and successively improved yielding user operability. Therefore, the needed tools were developed and implemented. The maximum current available in low-α operation was pushed up to the limits imposed by radiation protection regulations. The momentum dependence of the momentum compaction factor was directly measured up to the third order applying different measurement techniques. A calibration of the dependence of α_2 on the octupole excitation current in low-α user optics was performed. For beam dynamics studies an operation mode with negative momentum compaction was implemented including a separate injection state as well as a separate energy ramp. Operation with negative momentum compaction is now available for further investigation with beam currents of up to 100 mA. Potentially limiting effects were investigated through the means of particle tracking as well as experimental observation. In addition, the feasibility of a low-α-low-emittance mode was explored using a brute force approach globally scanning for solutions in the space of quadrupole field strengths.

Additional buckets in longitudinal phase space – α-buckets – were experimentally observed at the MLS as well as BESSY II. Properties of α-buckets were investigated and manipulated using the unique capability of the MLS to control the three leading orders of $\alpha(\delta)$. The required theory was derived and compared to particle tracking as well as measurement results. The capability to introduce α-buckets to the longitudinal phase space without deteriorating the RF-bucket may potentially add qualitatively new features to the operation of storage ring light sources. Several new application modes have been experimentally investigated at the MLS such as simultaneous operation with multiple filling patterns or bunch lengths as well as generating a defined and tunable arrival time delay between bunches in the picosecond regime.

The coherent synchrotron radiation usable at the MLS was characterized with focus on instabilities. In particular the threshold of the microbunching instability was experimentally observed and measured with high reproducibility over a wide range in terms of current respectively bunch length. Results were compared to similar measurements at the BESSY II storage ring. The threshold of the weak instability was observed emerging at bunch lengths in the order of a few picoseconds. The applicability of commonly used scaling laws for bunch lengths in the regime of the weak instability or below has been investigated. This is of relevance for future short pulse storage rings such as BESSY$^{\mathrm{VSR}}$ targeting comparatively high current operation in new bunch length regimes of 1 ps or below. In addition, the current dependent bunch length was characterized using a streak camera at the MLS, which is now used as a reference measurement by THz users.

MAD-X input files

MAD-X input file 1: MLS standard user

```
TITLE,"MLS: standard user mode, PTC ->
E=629MeV,alpha=0.03,Qx=3.178,Qy=2.232,DQX=0,DQY=0";

option,echo,warn,info;
ASSIGN,ECHO=echo.dat;

beam,particle=electron,energy=0.629,sige=4.4e-4,sigt=1e-3;//,radiate;

//RF CAVITY DEFINITON
CAV: RFCAVITY,L=0.15,VOLT=-0.5/2.0,HARMON=80,no_cavity_totalpath=true; // 1/2 RF CAV

//DRIFT DEFINITION
DL      : drift, L = 3.0;        // 1/2 long straight
DL_CAV  : drift, L = 2.85;       // 1/2 long straight in RF cavity straight
DK      : drift, L = 1.25;       // 1/2 short straight
D1      : drift, L = 0.15;
D2      : drift, L = 0.125;
D3      : drift, L = 0.425;
D4      : drift, L = 0.3;

//DIPOLE DEFINITION
BBSBEND: SBEND, L=1.2, ANGLE=PI/4;
BBDIPEDGE1: dipedge, h=PI/4./1.2,E1=PI/8.,hgap=0.025,FINT=0.5;
BBDIPEDGE2: dipedge, h=PI/4./1.2,E1=PI/8.,hgap=0.025,FINT=0.5;
BB: line=(BBDIPEDGE1,BBSBEND,BBDIPEDGE2);

//QUADRUPOLE DEFINITION // Qx=3.178,Qy=2.232,alpha_0=0.03
VQ1      =  2.9624;
VQ1_SEP  =  2.4746;
VQ2K     = -4.50667;
VQ2L     = -4.17499;
VQ3K     =  5.00574;
VQ3L     =  5.19192;
Q1      : QUADRUPOLE,  L=0.2, K1:=VQ1;
Q1_SEP  : QUADRUPOLE,  L=0.2, K1:=VQ1_SEP;
Q2K     : QUADRUPOLE,  L=0.2, K1:=VQ2K;
Q3K     : QUADRUPOLE,  L=0.2, K1:=VQ3K;
Q2L     : QUADRUPOLE,  L=0.2, K1:=VQ2L;
Q3L     : QUADRUPOLE,  L=0.2, K1:=VQ3L;

//SEXTUPOLE DEFINITION  // xi_x=xi_y=+1
VS1 =   89.5039;
VS2 = -108.271;
VS3 =    0.0;
S1:SEXTUPOLE,L=0.1,K2:=VS1;
S2:SEXTUPOLE,L=0.1,K2:=VS2;
S3:SEXTUPOLE,L=0.1,K2:=VS3;

//OCTUPOLE DEFINITION
O1:OCTUPOLE,L=0.1,K3=0.0;
```

```
//RING DEFINITION
RING:LINE=(
    DK     ,S3,D1,Q3K,D1,Q2K,D3,BB,D3,S2,D4,S1,D1,Q1_SEP,D2,O1,D2,Q1     ,D1,S1,D4,S2,
        D3,BB,D3,Q2L,D1,Q3L,D1,S3,DL,
    DL     ,S3,D1,Q3L,D1,Q2L,D3,BB,D3,S2,D4,S1,D1,Q1     ,D2,O1,D2,Q1     ,D1,S1,D4,S2,
        D3,BB,D3,Q2K,D1,Q3K,D1,S3,DK,
    DK     ,S3,D1,Q3K,D1,Q2K,D3,BB,D3,S2,D4,S1,D1,Q1     ,D2,O1,D2,Q1     ,D1,S1,D4,S2,
        D3,BB,D3,Q2L,D1,Q3L,D1,S3,DL_CAV,CAV,
CAV,DL_CAV,S3,D1,Q3L,D1,Q2L,D3,BB,D3,S2,D4,S1,D1,Q1     ,D2,O1,D2,Q1_SEP,D1,S1,D4,S2,
    D3,BB,D3,Q2K,D1,Q3K,D1,S3,DK
);

USE,period=RING;

PTC_CREATE_UNIVERSE;
PTC_CREATE_LAYOUT,model=2,method=6,nst=10,exact;
PTC_ALIGN;
PTC_TWISS,file=twiss_ptc.dat,ICASE=5,closed_orbit,no=2,deltap=0.00;
PTC_END;

PTC_CREATE_UNIVERSE;
PTC_CREATE_LAYOUT,model=2,method=6,nst=10,exact;
PTC_ALIGN;
PTC_START, x= 0.0001, px= 0.0, y= 0.0001, py= 0.00, t= 0.0,pt= 0.001;
PTC_TRACK, deltap=0.0 , dump,file=track_ptc_1.txt,turns=10001,ICASE=6;
PTC_TRACK_END;
PTC_END;

STOP;
```

MAD-X input file 2: MLS low-alpha user

```
TITLE,"MLS: Low-alpha user mode, PTC
-> E=629MeV,alpha=0.000127,Qx=3.178,Qy=2.232,DQX=0,DQY=0";

option,echo,warn,info;
ASSIGN,ECHO=echo.dat;

beam,particle=electron,energy=0.629,sige=4.2e-4,sigt=1e-3;//,radiate;

//RF CAVITY DEFINITION
CAV: RFCAVITY,L=0.15,VOLT=-0.5/2.0,HARMON=80,no_cavity_totalpath=true; // 1/2 RF CAV

//DRIFT DEFINITION
DL      : drift, L = 3.0;        // 1/2 long straight
DL_CAV  : drift, L = 2.85;       // 1/2 long straight in RF cavity straight
DK      : drift, L = 1.25;       // 1/2 short straight
D1      : drift, L = 0.15;
D2      : drift, L = 0.125;
D3      : drift, L = 0.425;
D4      : drift, L = 0.3;

//DIPOLE DEFINITION
BBSBEND: SBEND, L=1.2, ANGLE=PI/4;
BBDIPEDGE1: dipedge, h=PI/4./1.2,E1=PI/8.,hgap=0.025,FINT=0.5;
BBDIPEDGE2: dipedge, h=PI/4./1.2,E1=PI/8.,hgap=0.025,FINT=0.5;
BB: line=(BBDIPEDGE1,BBSBEND,BBDIPEDGE2);

//QUADRUPOLE DEFINITION // Qx=3.178,Qy=2.232,alpha_0=0.000127
VQ1      =  3.17930;
VQ1_CAV  =  3.46049;
VQ2K     = -4.47299;
VQ2L     = -4.10793;
VQ3K     =  5.01444;
VQ3L     =  4.89629;
Q1      : QUADRUPOLE,  L=0.2, K1:=VQ1;
Q1_CAV  : QUADRUPOLE,  L=0.2, K1:=VQ1_CAV;
Q2K     : QUADRUPOLE,  L=0.2, K1:=VQ2K;
Q3K     : QUADRUPOLE,  L=0.2, K1:=VQ3K;
Q2L     : QUADRUPOLE,  L=0.2, K1:=VQ2L;
Q3L     : QUADRUPOLE,  L=0.2, K1:=VQ3L;

//SEXTUPOLE DEFINITION  // xi_x=xi_y=alpha_1=0
VS1= 44.7432;
VS2=-70.6191;
VS3= -7.635;
S1:SEXTUPOLE,L=0.1,K2:=VS1;
S2:SEXTUPOLE,L=0.1,K2:=VS2;
S3:SEXTUPOLE,L=0.1,K2:=VS3;

//OCTUPOLE DEFINITION  // alpha_2>=0
O1:OCTUPOLE,L=0.1,K3=-100.0;

//RING DEFINITION
RING:LINE=(CAV,
DL_CAV,S3,D1,Q3L,D1,Q2L,D3,BB,D3,S2,D4,S1,D1,Q1_CAV,D2,O1,D2,Q1     ,D1,S1,D4,S2,D3,BB
    ,D3,Q2K,D1,Q3K,D1,S3,DK,
DK     ,S3,D1,Q3K,D1,Q2K,D3,BB,D3,S2,D4,S1,D1,Q1     ,D2,O1,D2,Q1     ,D1,S1,D4,S2,D3,BB
    ,D3,Q2L,D1,Q3L,D1,S3,DL,
DL     ,S3,D1,Q3L,D1,Q2L,D3,BB,D3,S2,D4,S1,D1,Q1     ,D2,O1,D2,Q1     ,D1,S1,D4,S2,D3,BB
    ,D3,Q2K,D1,Q3K,D1,S3,DK,
DK     ,S3,D1,Q3K,D1,Q2K,D3,BB,D3,S2,D4,S1,D1,Q1     ,D2,O1,D2,Q1_CAV,D1,S1,D4,S2,D3,BB
```

```
      ,D3,Q2L,D1,Q3L,D1,S3,DL_CAV
   ,CAV);

   USE,period=RING;

   PTC_CREATE_UNIVERSE;
   PTC_CREATE_LAYOUT,model=2,method=6,nst=10,exact;
   PTC_ALIGN;
   PTC_TWISS,file=twiss_ptc.dat,ICASE=5,closed_orbit,no=2,deltap=0.00;
   PTC_END;

   PTC_CREATE_UNIVERSE;
   PTC_CREATE_LAYOUT,model=2,method=6,nst=10,exact;
   PTC_ALIGN;
   PTC_START, x= 0.0001, px= 0.0, y= 0.0001, py= 0.00, t= 0.0,pt= 0.001;
   PTC_TRACK, dump,file="track_ptc_1.txt",turns=10001,ICASE=6;
   PTC_TRACK_END;
   PTC_END;

   STOP;
```

Bibliography

[1] D. W. Lynch, "Tantalus, a 240MeV Dedicated Source of Synchrotron Radiation, 1968–1986," *J. Synchrotron Rad.*, vol. 4, no. 6, pp. 334–343, 1997.

[2] A. L. Robinson, "History of Synchrotron Radiation," in *X-Ray Data Booklet (expanded version)*, Berkeley, CA 94720: Lawrence Berkeley National Laboratory, 2009.

[3] B. W. J. McNeil and N. R. Thompson, "X-ray free-electron lasers," *Nature Photon.*, vol. 4, no. 12, pp. 814–821, 2010.

[4] D. H. Bilderback *et al.*, "Energy recovery linac (ERL) coherent hard x-ray sources," *New J. Phys.*, vol. 12, 035011, 2010.

[5] J. Knobloch *et al.*, "Status of the BERLinPro Energy Recovery Linac Project," in *Proceedings of IPAC2012*, International Particle Accelerator Conference, (New Orleans, USA), pp. 601–603, 2012.

[6] M. Eriksson *et al.*, "The MAX-IV Design: Pushing the Envelope," in *Proceedings of PAC07*, Particle Accelerator Conference, (Albuquerque, USA), pp. 74–76, 2007.

[7] E. B. Blum, M. Dienes, and J. Murphy, eds., *Micro Bunches Workshop*, (Upton, USA), 1995.

[8] G. Wüstefeld, "Short Bunches in Electron Storage Rings and Coherent Synchrotron Radiation," in *Proceedings of EPAC08*, European Particle Accelerator Conference, (Genoa, Italy), pp. 26–30, 2008.

[9] A.-S. Müller, "Short-Pulse Operation of Storage Ring Light Sources," in *Proceedings of IPAC2013*, International Particle Accelerator Conference, (Shanghai, China), pp. 1129–1133, 2013.

[10] M. Abo-Bakr *et al.*, "Steady-state far-infrared coherent synchrotron radiation detected at BESSY II," *Phys. Rev. Lett.*, vol. 88, no. 25, 2002.

[11] Y. Orlov, "Bunch length compression using crab cavities," in *Beam Dynamics Issues of High-Luminosity Asymmetric Collider Rings*, vol. 214 of *American Institute of Physics Conference Series*, pp. 336–346, 1990.

[12] K.-J. Kim, S. Chattopadhyay, and C. Shank, "Generation of femtosecond X-rays by 90° Thomson scattering," *Nucl. Instrum. Methods Phys. Res., Sect. A*, vol. 341, no. 1-3, pp. 351–354, 1994.

[13] G. Wüstefeld *et al.*, "Simultaneous Long and Short Electron Bunches in the BESSY II Storage Ring," in *Proceedings of IPAC2011*, International Particle Accelerator Conference, (San Sebastián, Spain), pp. 2936–2938, 2011.

[14] A. A. Zholents, "Generation of Subpicosecond X-ray Pulses in Storage Rings," in *Proceedings of PAC07*, Particle Accelerator Conference, (Albuquerque, USA), pp. 1272–1276, 2007.

[15] B. Beckhoff *et al.*, "A quarter-century of metrology using synchrotron radiation by PTB in Berlin," *Phys. Status Solidi B*, vol. 246, no. 7, pp. 1415–1434, 2009.

[16] J. Schwinger, "On the classical radiation of accelerated electrons," *Phys. Rev.*, vol. 75, no. 12, pp. 1912–1925, 1949.

[17] R. Klein *et al.*, "Operation of the metrology light source as a primary radiation source standard," *Phys. Rev. ST Accel. Beams*, vol. 11, 110701, 2008.

[18] D. Krämer *et al.*, "MLS technical design report," tech. rep., BESSY GmbH, Berlin, Germany, 2003.

[19] A. Gottwald *et al.*, "Ultraviolet and vacuum-ultraviolet detector-based radiometry at the Metrology Light Source," *Meas. Sci. Technol.*, vol. 21, 125101, 2010.

[20] K. Buerkmann *et al.*, "Commissioning of the 100 MeV Racetrack Microtron of the Metrology Light Source," in *Proceedings of PAC07*, Particle Accelerator Conference, (Albuquerque, USA), pp. 944–946, 2007.

[21] T. Birke *et al.*, "Automated Operation of the MLS Electron Storage Ring," in *Proceedings of PAC09*, Particle Accelerator Conference, (Vancouver, Canada), pp. 1798–1800, 2009.

[22] J. Feikes *et al.*, "Recent Developments at the Metrology Light Source," in *Proceedings of IPAC2011*, International Particle Accelerator Conference, (San Sebastián, Spain), pp. 2927–2929, 2011.

[23] J. Feikes *et al.*, "Metrology Light Source: The first electron storage ring optimized for generating coherent THz radiation," *Phys. Rev. ST Accel. Beams*, vol. 14, 030705, 2011.

[24] E. Weihreter, "Status of the European HOM Damped Normal Conducting Cavity," in *Proceedings of EPAC08*, European Particle Accelerator Conference, (Genoa, Italy), pp. 2932–2936, 2008.

[25] T. Goetsch *et al.*, "Lifetime Studies at Metrology Light Source and ANKA," in *Proceedings of IPAC2013*, International Particle Accelerator Conference, (Shanghai, China), pp. 88–909, 2013.

[26] P. Schmid *et al.*, "Optics Calibration at the MLS and at BESSY II," in *Proceedings of IPAC'10*, International Particle Accelerator Conference, (Kyoto, Japan), pp. 2505–2507, 2010.

[27] H. Wiedemann, *Particle Accelerator Physics*. Springer Berlin Heidelberg New York, 3 ed., 2007.

[28] K. Wille, *The Physics of Particle Accelerators*. Oxford, 2000.

[29] E. Courant and H. Snyder, "Theory of the Alternating-Gradient Synchrotron," *Annals of Physics*, vol. 3, no. 1, pp. 1–48, 1958.

[30] J.-P. Delahaye and J. Jäger, "Variation of the Dispersion Function, Momentum Compaction Factor, and Damping Partition Numbers with Particle Energy Deviation," *Particle Accelerators*, vol. 18, pp. 183–201, 1986.

[31] A. W. Chao and M. Tigner, *Handbook of accelerator physics and engineering*. World Scientific Publishing Company, Incorporated, 3 ed., 1999.

[32] S. Koscielniak, "Slip Factor Expansions for LONG1D," Tech. Rep. TRI-DN-00-11, TRI-UMF, 2000.

[33] H. Bruck, *Circular Particle Accelerators*. Los Alamos Scientific Laboratory, English translation, 1966.

[34] K. Ng, "Physics of intensity dependent beam instabilities," Tech. Rep. FERMILAB-FN-0713, Fermilab, 2002.

[35] Y. Shoji, "Bunch lengthening by a betatron motion in quasi-isochronous storage rings," *Phys. Rev. ST Accel. Beams*, vol. 7, no. 090703, 2004.

[36] Y. Shoji, "Dependence of average path length betatron motion in a storage ring," *Phys. Rev. ST Accel. Beams*, vol. 8, no. 094001, 2005.

[37] M. Sands, "The Physics of Electron Storage Rings - An Introduction," tech. rep., U. S. Atomic Energy Commission, SLAC-121 UC-28 (ACC), 1970.

[38] Y. Shoji *et al.*, "Longitudinal radiation excitation in an electron storage ring," *Phys. Rev. E*, vol. 54, no. 5, pp. R4556–R4559, 1996.

[39] K. Johnsen, "Transition," in *Proceedings of CERN Accelerator School – General Accelerator Physics*, pp. 178–194, CERN, 1984.

[40] Y. Shoji, "Quasi-isochronous Operation at NewSUBARU," in *Proceedings of EPAC 2004*, European Particle Accelerator Conference, (Lucerne, Switzerland), pp. 2356–2358, 2004.

[41] M. Klein, *Optics Calculations and Simulations of the Longitudinal Beam Dynamics for the Low-α Mode at ANKA*. PhD thesis, Karlsruher Institut für Technologie, 2012.

[42] I. P. S. Martin *et al.*, "Low alpha operation of the diamond storage ring," in *Proceedings of IPAC'10*, International Particle Accelerator Conference, (Kyoto, Japan), pp. 4599–4601, 2010.

[43] A. Ando *et al.*, "VUV and Soft X-ray Light Source "NEW SUBARU"," in *PAC'97 Proceedings*, Particle Accelerator Conference, (Vancouver, B.C., Canada), pp. 757–759, 1997.

[44] M.-A. Tordeux *et al.*, "Low-alpha operation for the soleil storage ring," in *Proceedings of IPAC2012*, International Particle Accelerator Conference, (New Orleans, USA), pp. 1608–1610, 2012.

[45] X. Huang *et al.*, "Low Alpha Mode for SPEAR3," in *Proceedings of PAC07*, Particle Accelerator Conference, (Albuquerque, USA), pp. 1308–1310, 2007.

[46] Y. Cai, ed., *ICFA Beam Dynamics Newsletter No. 57*, 2012.

[47] C. J. A. Corsten, *Resonance and Coupling Effects in Circular Accelerators*. PhD thesis, Eindhoven University of Technology, 1982.

[48] C. Pellegrini and D. Robin, "Quasi-isochronous storage ring," *Nucl. Instrum. Methods Phys. Res., Sect. A*, vol. 301, no. 1, pp. 27–36, 1991.

[49] R. Klein, R. Thornagel, and G. Ulm, "From single photons to milliwatt radiant power–electron storage rings as radiation sources with a high dynamic range," *Metrologia*, vol. 47, no. 5, pp. R33–R40, 2010.

[50] R. Brun and F. Rademakers, "ROOT - An object oriented data analysis framework," *Nucl. Instrum. Methods Phys. Res., Sect. A*, vol. 389, no. 1-2, pp. 81–86, 1997.

[51] R. Helm *et al.*, "Evaluation of synchrotron radiation integrals," in *IEEE Transactions on Nuclear Science, Volume NS-20, Number 3*, Particle Accelerator Conference, (San Francisco, USA), pp. 900–901, 1973.

[52] K. W. Robinson, "Radiation Effects in Circular Electron Accelerators," *Phys. Rev.*, vol. 111, no. 2, pp. 373–380, 1958.

[53] H. Abualrob *et al.*, "SOLEIL Emittance Reduction using a Robinson Wiggler," in *Proceedings of IPAC2012*, International Particle Accelerator Conference, (New Orleans, USA), pp. 702–704, 2012.

[54] M. Ries *et al.*, "Survey of Beam Optics Solutions for the MLS Lattice," in *Proceedings of IPAC2013*, International Particle Accelerator Conference, (Shanghai, China), pp. 1883–1885, 2013.

[55] D. S. Robin *et al.*, "Global analysis of all linear stable settings of a storage ring lattice," *Phys. Rev. ST Accel. Beams*, vol. 11, 024002, 2008.

[56] C. Biscari, "Bunch length modulation in highly dispersive storage rings," *Phys. Rev. ST Accel. Beams*, vol. 8, 091001, 2005.

[57] L. Yang *et al.*, "Global optimization of an accelerator lattice using multiobjective genetic algorithms," *Nucl. Instrum. Methods Phys. Res., Sect. A*, vol. 609, no. 1, pp. 50–57, 2009.

[58] C. Steier *et al.*, "Measuring and optimizing the momentum aperture in a particle accelerator," *Phys. Rev. E*, vol. 65, 056506, 2002.

[59] H. Grote and F. Schmidt, "MAD-X – An Upgrade from MAD8," in *Proceedings of the 2003 Particle Accelerator Conference*, Particle Accelerator Conference, (Portland, USA), pp. 3497–3499, 2003.

[60] G. Wüstefeld, "Horizontal-longitudinal Coupling in the FEL Beam Line," tech. rep., Berliner Elektronenspeicherring-Gesellschaft für Synchrotronstrahlung (BESSY), 2005.

[61] G. Wüstefeld, "The BESSY Low Alpha Optics and the Generation of Coherent Synchrotron Radiation," in *ICFA Mini-Workshop on Frontiers of Short Bunches in Storage Rings*, (Frascati, Italy), 2005.

[62] J. Safranek, G. Portmann, and A. Terebilo, "MATLAB-based LOCO," in *Proceedings of EPAC 2002*, European Particle Accelerator Conference, (Paris, France), pp. 1184–1186, 2002.

[63] G. Portmann, J. Corbett, and A. Terebilo, "An Accelerator Control Middle Layer Using MATLAB," in *Proceedings of the 2005 Particle Accelerator Conference*, Particle Accelerator Conference, (Knoxville, USA), pp. 4009–4011, 2005.

[64] J. Feikes, "Investigation of lifetime and source size." MLS Commissioning Report, 2012.

[65] S. R. Mane, Y. M. Shatunov, and K. Yokoya, "Spin-polarized charged particle beams in high-energy accelerators," *Rep. Prog. Phys.*, vol. 68, no. 9, p. 1997, 2005.

[66] P. Kuske and R. Goergen, "High Precision Determination of the Energy at BESSY II," in *Proceedings of EPAC 2000*, (Vienna, Austria), pp. 1771–1773, 2000.

[67] A.-S. Müller, *Precision Measurements of the LEP Beam Energy for the Determination of the W Boson Mass*. PhD thesis, Johannes Gutenberg-Universität, Mainz, Germany, 2000.

[68] A. H. Compton, "A Quantum Theory of the Scattering of X-rays by Light Elements," *Phys. Rev.*, vol. 21, no. 5, pp. 483–502, 1923.

[69] R. Klein *et al.*, "Beam diagnostics at the BESSY I electron storage ring with Compton backscattered laser photons: Measurement of the electron energy and related quantities," *Nucl. Instrum. Methods Phys. Res., Sect. A*, vol. 384, no. 2-3, pp. 293–298, 1997.

[70] J. Feikes and G. Wüstefeld, "Experimental Studies of the Nonlinear Momentum Compaction Factor at BESSY II," in *Proceedings of the 1999 Particle Accelerator Conference*, Particle Accelerator Conference, (New York, USA), pp. 2376–2378, 1999.

[71] H. Hama, S. Takano, and G. Isoyama, "Control of the bunch length on an electron storage ring," *Nucl. Instrum. Methods Phys. Res., Sect. A*, vol. 329, no. 1-2, pp. 29–36, 1993.

[72] D. A. G. Deacon, "Basic Theory of the Isochronous Storage Ring Laser," *Phys. Rep.*, vol. 76, no. 5, pp. 349–391, 1981.

[73] *CERN Symposium On High Energy Accelerators and Pion Physics*, vol. I, (Geneva, Switzerland), 1956. Chapter: "Problems concerning the transition energy".

[74] J. B. Murphy and S. L. Kramer, "First Observation of Simultaneous Alpha Buckets in a Quasi-Isochronous Storage Ring," *Phys. Rev. Lett.*, vol. 84, no. 24, pp. 5516–5519, 2000.

[75] I. P. S. Martin *et al.*, "Experience with low-alpha lattices at the Diamond Light Source," *Phys. Rev. ST Accel. Beams*, vol. 14, 040705, 2011.

[76] M. Attal *et al.*, "Dynamics of three simultaneously stored beams in a storage ring," *Phys. Rev. ST Accel. Beams*, vol. 16, 054001, 2013.

[77] M. Ries *et al.*, "Simultaneous Long and Short Bunch Operation in an Electron Storage Ring - a Hybrid Mode based on Nonlinear Momentum Compaction," in *Proceedings of IPAC2011*, International Particle Accelerator Conference, (San Sebastián, Spain), pp. 945–947, 2011.

[78] C. Koschitzki *et al.*, "Highly Sensitive Beam Size Monitor for pA Currents at the MLS Electron Storage Ring," in *Proceedings of IPAC'10*, International Particle Accelerator Conference, (Kyoto, Japan), pp. 894–896, 2010.

[79] F. Falkenstern *et al.*, ""BUNCHVIEW" – A Fast and Accurate Bunch-by-Bunch Current Monitor," in *Proceedings of DIPAC09*, European Workshop on Beam Diagnostics and Instrumentation for Particle Accelerators, (Basel, Switzerland), pp. 128–130, 2009.

[80] Forschungszentrum Jülich, "Chopper für Synchrotronstrahlung." preliminary information in german, 2013.

[81] C. Sun *et al.*, "Pseudo-Single-Bunch with Adjustable Frequency: A New Operation Mode for Synchrotron Light Sources," *Phys. Rev. Lett.*, vol. 109, no. 26, 2012.

[82] D. Teytelman, *iGp12 User Manuals*. http://www.dimtel.com/support/manuals/igp12, 2010.

[83] *Universal Streak Camera C5680 Series*. Hamamatsu, 2010.

[84] M. Ruprecht *et al.*, "Single Particle Tracking for Simultaneous Long and Short Electron Bunches in the BESSY II Storage Ring," in *Proceedings of IPAC2013*, International Particle Accelerator Conference, (Shanghai, China), pp. 2038–2040, 2013.

[85] J. Feikes, P. Kuske, and G. Wüstefeld, "Towards Sub-Picosecond Electron Bunches: Upgrading Ideas For BESSY II," in *Proceedings of EPAC 2006*, European Particle Accelerator Conference, (Edinburgh, Scotland), pp. 157–159, 2006.

[86] J. Schwinger, "Electron Radiation in High Energy Accelerators," *Phys. Rev.*, vol. 70, no. 9-10, pp. 798–799, 1946.

[87] J. S. Nodvick and D. S. Saxon, "Suppression of Coherent Radiation by Electrons in a Synchrotron," *Phys. Rev.*, vol. 96, no. 1, pp. 180–184, 1954.

[88] M. Ries *et al.*, "THz Bursting Thresholds Measured at the Metrology Light Source," in *Proceedings of IPAC2012*, International Particle Accelerator Conference, (New Orleans, USA), pp. 3030–3032, 2012.

[89] C. Biscari, ed., *ICFA Beam Dynamics Newsletter No. 35*, 2004.

[90] R. L. Warnock, "Shielded Coherent Synchrotron Radiation and Its Effect on Very Short Bunches," tech. rep., SLAC, Report No. SLAC-PUB-5375, 1990.

[91] G. Williams, "Filling the THz gap – high power sources and applications," *Rep. Prog. Phys.*, vol. 69, no. 2, pp. 301–326, 2006.

[92] R. Müller *et al.*, "The Metrology Light Source of PTB - a Source for THz Radiation," *J Infrared Milli Terahz Waves*, vol. 32, pp. 742–753, 2011.

[93] R. Müller *et al.*, "THz Studies at a Dedicated Beamline at the MLS," in *Proceedings of IPAC2011*, International Particle Accelerator Conference, (San Sebastián, Spain), pp. 2933–2935, 2011.

[94] V. Judin *et al.*, "Observation of Microwave Radiation Using Low-Cost Detectors at the ANKA Storage Ring," in *Proceedings of IPAC2011*, International Particle Accelerator Conference, (San Sebastián, Spain), pp. 1203–1205, 2011.

[95] I. P. S. Martin *et al.*, "Operating the DIAMOND Light Source in Low Alpha Mode for Users," in *Proceedings of IPAC2013*, International Particle Accelerator Conference, (Shanghai, China), pp. 246–248, 2013.

[96] W. Anders, *Longitudinale Strahldynamik im Elektronen Speicherring BESSY I unter dem Einfluß der Breitbandimpedanz der Vakuumkammer.* PhD thesis, Universität Dortmund, 1992.

[97] G. Stupakov and S. Heifets, "Beam instability and microbunching due to coherent synchrotron radiation," *Phys. Rev. ST Accel. Beams*, vol. 5, 054402, 2002.

[98] K. L. F. Bane, Y. Cai, and G. Stupakov, "Threshold studies of the microwave instability in electron storage rings," *Phys. Rev. ST Accel. Beams*, vol. 13, 104402, 2010.

[99] Y. Cai, "Linear theory of microwave instability in electron storage rings," *Phys. Rev. ST Accel. Beams*, vol. 14, 061002, 2011.

[100] Y. Cai, "Theory of Microwave Instability and Coherent Synchrotron Radiation in Electron Storage Rings," in *Proceedings of IPAC2011*, International Particle Accelerator Conference, pp. 3774–3778, 2011.

[101] C. Evain *et al.*, "Spatio-temporal dynamics of relativistic electron bunches during the micro-bunching instability in storage rings," *EPL*, vol. 98, 40006, 2012.

[102] P. Kuske, "CSR-driven Longitudinal Single Bunch Instability Thresholds," in *Proceedings of IPAC2013*, International Particle Accelerator Conference, (Shanghai, China), pp. 2041–2043, 2013.

[103] P. Kuske, "Calculation of Longitudinal Instability Threshold Currents for Single Bunches," in *Proceedings of ICAP2012*, International Particle Accelerator Conference, pp. 267–269, 2012.

Acknowledgement

The completion of this doctoral thesis was made possible by the support of many colleagues from the HZB, the PTB and other institutions. Special gratitude is owed to...

Prof. Dr. Andreas Jankowiak for supervision in a friendly and open-minded way and for the granted freedom to pursue diverse research ideas. In case of need, he was always open for advice and gave me the opportunity to present the work in national and international talks,

Dr. Gerhard Ulm for ongoing support throughout the years and for close and productive cooperation of PTB users and the HZB machine group,

Dr. Godehard Wüstefeld for close mentoring on the broad field of accelerator physics and his friendship. Only by his foresight the MLS was equipped with additional sextupole and octupole magnets enabling all the fun you can have with nonlinear momentum compaction. His impressive ability to condense complicated problems to a simple core crucially guided long and exciting discussions about recent ideas, tracking or measurement results. In addition, his shared enthusiasm fueled joint weekend and night shifts,

Dr. Jörg Feikes, whose friendship, ongoing support and encouragement helped me to evolve a strong fascination for applied accelerator physics. We spent plenty of hours in the control room exploring ideas, evolving measurement concepts, chasing obstacles in the beam path and drinking East Frisian tea,

Dipl. Ing. Arne Hoehl and Dr. Ralph Müller, for patience and willingness to implement numerous experimental setups in close cooperation with the infrared/THz group of the PTB, for instructing me to handle liquid helium cooled detectors and for the granted freedom in the laboratory,

Dr. Roman Klein, who lured me to the field of accelerator physics during my diploma thesis and whose support continued during this work. Special thanks is owed for the support of the electron energy measurements based on Compton backscattering,

Dipl. Ing. Fjodor Falkenstern and Dipl. Ing. Jens Kuszynski for a lot of effort to prepare diagnostic signals and their digitalization needed for various automated measurements,

Dipl. Ing. Thomas Birke, Dipl. Ing. Dennis Engel and Dipl. Ing Benjamin Franksen for providing continuous help and development of the MLS control system as well as for taking hundreds of phone calls while dodging the other half,

Dipl. Ing. Hans-Georg Hoberg and Dipl. Ing. Andreas Heugel for their efforts to provide an optimized RF voltage including the means for manipulation,

Dr. Peter Schmid for constructive feedback on various talks,

Dr. Clement Evain, Vitali Judin and Dr. Ian Martin for a fascinating weekend spent at the MLS full of measurements and discussions on the matter of the THz bursting threshold,

Prof. Dr. Anke-Susanne Müller on behalf of the whole ANKA THz group for many interesting discussions, joint measurements and an exciting stay in Karlsruhe,

Dipl. Phys. Martin Ruprecht and Dipl. Phys. Tobias Goetsch for daily discussions as well as sharing the challenges of data analysis and visualization,

Dr. Robert Seidel as a friend and fellow physicist.

Finally, I would like to thank my family and my friends for their support and endurance during the last years.

Selbständigkeitserklärung

Ich erkläre, dass ich die vorliegende Arbeit selbständig und nur unter Verwendung der angegebenen Literatur und Hilfsmittel angefertigt habe.

Berlin, den 29. Oktober 2013 Markus Ries